Effect of Flap Position on Propeller-Wing-Flap Aerodynamic Interaction for Distributed Propulsion Systems

An experimental approach

Pedro López Pernas

TU Delft

Effect of Flap Position on Propeller-Wing-Flap Aerodynamic Interaction for Distributed Propulsion Systems

An experimental approach

by

Pedro López Pernas

to obtain the degree of Master of Science in Aerospace Engineering
at the Delft University of Technology,
to be defended publicly on Tuesday Febraury 22, 2022 at 14:00.

Student number:	5028922	
Project duration:	September, 2020 – February, 2022	
Supervisor:	Ir. R. de Vries,	TU Delft
	Dr. ir. L.L.M. Veldhuis	TU Delft
Thesis committee:	Ir. R. de Vries,	TU Delft
	Dr. ir. L.L.M. Veldhuis	TU Delft
	Dr. T. Sinnige	TU Delft
	Dr. N. Timmer	TU Delft

TU Delft

Picture of the cover taken by Tomas Sinnige (Assistant Professor at TU Delft).

SUMMARY

Aviation is responsible for a large part of the emissions due to transportation, which is why, in recent years, a trend towards implementing sustainability in aviation has emerged. In small aircraft, the concept of Leading-Edge Distributed Propulsion (LEDP) can provide aerodynamic advantages to reduce fuel consumption thanks to the ability to increase lift due to the interaction between the slipstream of the propellers and the wing.

Therefore, a wind tunnel experiment is performed to study the aerodynamic interaction in propeller-wing-flap systems when Leading-Edge Distributed Propulsion is used. The objective of this research is to gain insight into the difference in wing loading distribution between the distributed-propeller and single-propeller configurations in the flap retracted case, about the effect of flap position on the lift enhancement in LEDP and about the effect of flap deflection on the wake downstream of the system.

The model consists of a 2.5D configuration semi-span wing with three propellers and a Fowler flap. The experiment takes place in the DNW low-speed tunnel. The measurement techniques used are balance forces to obtain the wing lift and drag, the model is also instrumented with pressure taps at two sections located behind the medium propeller, where maximum blade loading is expected, on both up- and down-going blade side to obtain the pressure distribution and sectional lift and pressure drag; and five-hole probe wake measurement located a one chord from the wing in flap retracted configuration to analyze the slipstream deformation as it interacts with the wing.

Experimental results show that the wing lift enhancement of the distributed-propulsion configuration is similar to three times that generated by the single-propeller configuration. However, there is a modification of the pressure distribution, that is recorded behind the middle propeller, due to the effect of the adjacent propeller's slipstream, resulting in higher sectional lift. This influence is higher on the down-going blade side due to the adjacent up-going propeller. In addition, an increase in rear loading is observed behind the middle propeller due to the slipstream impingement of the adjacent slipstream, which increases with increasing thrust because the deformation of the slipstream due to trailing vorticity increases.

When evaluating the effect of flap position on lift enhancement, it can be seen how at low angles of attack the enhancement increases with flap deflection angle, mainly due to an increase in flap suction. However, while for the flap retracted configuration the enhancement increases with AoA, a larger flap deflection angle causes the enhancement

to decrease with angle of attack due to the higher position of the propeller. At higher angles of attack the lift enhancement increases again since the propeller-off configuration is stalled, resulting in a big difference between the lift generated in prop-on and prop-off configurations. When evaluating the effect of the flap gap, it is found that the lift is higher when the flap gap is smaller in propeller-off condition, a similar flap pressure distribution is obtained for both flap gap values when the propellers are on.

The results obtained in this experiment help to better understand the aerodynamic interaction of propeller-wing-flap systems with distributed propulsion. The comparison of the slipstream effect on wing loading between the single-propeller case and the distributed-propulsion case in flap retracted configuration, the use of different flap positions to evaluate their influence on the lift enhancement produced by the distributed-propulsion system and the analysis of the slipstream deformation under flap action provide a complete assessment of the aerodynamics of the system and contribute to the development of leading-edge distributed propulsion configurations for electric/hybrid-electric aircraft.

CONTENTS

NOMENCLATURE

List of symbols

δ,δ_f	Flap deflection angle	[deg]
$\dot{m}$	Mass flow rate	[kg/s]
ω	Propeller rotational velocity	[Hz]
ϕ_T	Helix angle at the tip	[deg]
ρ_∞	Free-stream density	[kg/m^3]
σ	Blade solidity	[-]
θ	Turning angle	[deg]
θ_{swirl}	Propeller swirl angle	[deg]
θ_p,i_p	Propeller inclination angle	[deg]
a	Axial induction factor	[-]
A, A_p	Propeller disk area	[m^2]
a'	Tangential induction factor	[-]
c	Wing chord	[m]
C_{d_p}	Sectional pressure drag coefficient	[-]
C_D	Wing drag coefficient	[-]
c_f	Flap chord	[m]
$C_{L_{eff}}$	Lift coefficient including thrust force	[-]
$C_{L_{Thrust}}$	Contribution of the thrust force to the lift coefficient	[-]
C_L	Wing lift coefficient	[-]
C_l	Sectional lift coefficient	[-]
c_p	Pressure coefficient	[-]

D	Drag force	[N]
$D,_p$	Propeller diameter	[m]
F	Tip-loss correction factor	[-]
F/T	Thrust recovery factor	[-]
J	Propeller advance ration	[-]
k	Transition strip grain size	[m]
L	Lift force	[N]
$p_{1,2,3,4}$	Static pressure far upstream, immediately upstream, immediately downstream and far downstream of the propeller, respectively	[Pa]
p_∞	Free-stream static pressure	[Pa]
P_i	Propeller required power	[N]
p_t	Local total pressure	[Pa]
q_∞	Free-stream dynamic pressure	[Pa]
$R,_p$	Propeller radius	[m]
Re	Reynolds number	[-]
S_{ref}	Wing reference area (wing area, 0.375 m^2)	[m^2]
T	Propeller thrust	[N]
t/c	Thickness-to-chord ratio	[-]
T_c	Thrust coefficient	[-]
$V_{1,2,3,4}$	Velocity far upstream, immediately upstream, immediately downstream and far downstream of the propeller, respectively	[m/s]
V_∞	Free-stream velocity	[m/s]
V_a, V_{axial}	Axial velocity	[m/s]
v_i	Propeller induced velocity	[m/s]
V_t	Tangential velocity	[m/s]
x_f	Flap overlap (horizontal distance wrt main element trailing-edge)	[%c]
x_p	Propeller horizontal distance wrt wing leading-edge	[m]
z_f	Flap gap (vertical distance wrt main element trailing-edge)	[%c]
z_p	Propeller vertical distance wrt wing leading-edge	[m]

AoA, α	Angle of attack	[deg]

Acronyms

DEP	Distributed Electric Propulsion
FP	Flap Position
LST	Low Speed Tunnel
LTT	Low Turbulence Tunnel
RAM	Regional Air Mobility
STOL	Short Take Off and Landing
TE	Trailing-edge
UAM	Urban Air Mobility

List of Figures

List of Tables

1

INTRODUCTION

The aviation industry is a great contributor to the climate change through the gasses that are emitted from the internal combustion engines (ICE) and the contrails generated at high altitude. According to the European Aviation Environmental Report [1], in 2016 the aviation was responsible of 13.4% of the CO_2 emission due to transport. A 42% growth in the number of flights is forecasted to 2040 that brings a 21% increase in CO_2 emissions and a 16% increase in NO_x emissions. Another source, such as the ICAO 2019 Environmental Report [2], predicts and increase in the emissions of 2 to 4 times from 2015 to 2050 depending on the type of the emission and the scenario used. In figure (1.1), it can be appreciated how the CO_2 emissions are predicted to grow despite the technological advancements, therefore, new disruptive aircraft concepts with reduced climate impacts are required.

Seeing these predictions, it is not surprising that the European Union has created a vision for the future, this project is called Fligthpath 2050 and aims to emit 75% less CO_2, 90% less NO_x and 65% less noise when compared to a typical new aircraft in 2000. [4]. In order to meet these ambitious goals, it is necessary to incorporate sustainable technology in aviation, which is the purpose of projects such as CleanSky 2 and the NASA Environmentally Responsible Aviation (ERA).

Incorporating sustainability into aviation can be understood as the substitution of the fuel for another green energy source, the use of more efficient power sources or the implementation of new configurations to reduce the energy consumption of the aircraft. All of the measures mentioned before have a common actor: the electricity. Electricity, when obtained from a green energy source, does not produce gas emissions; it powers electric engines, which are more efficient and compact than combustion engines [5]; and,

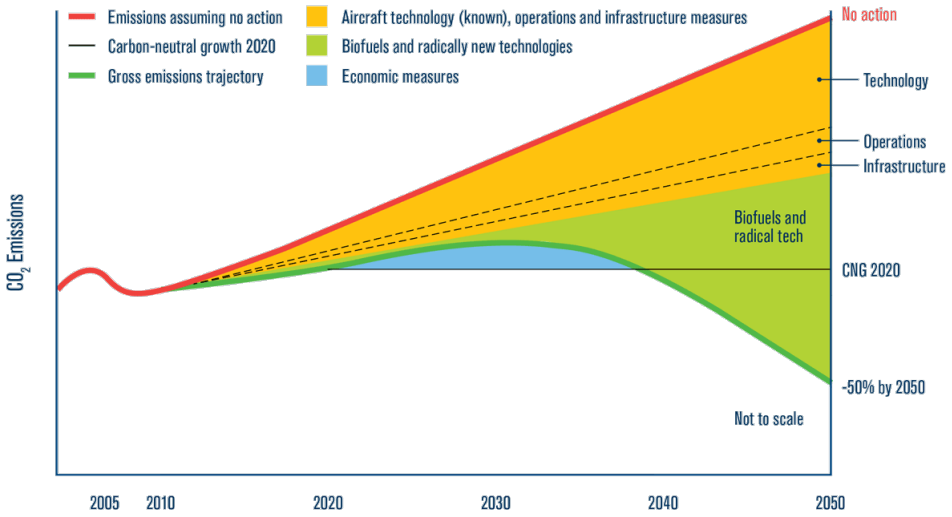

Figure 1.1: CO_2 emissions roadmap [3]

since the transmission of energy is done through wires, it allows to place these engines in a strategic location to obtain additional benefit of the interaction of the engine with the flow that surrounds the airframe.

The electricity used to power the airplanes could be obtained by several ways: extracted from a storage of energy, like batteries; obtained through chemical reaction, like the fuel cells; or directly obtained from the sun using solar panels. For small aircraft, the most promising technology in the short term seems to be the battery technology [6]. The two most important parameters regarding the batteries are the specific energy (Wh/kg), that governs the energy capacity for a certain amount of batteries and hence it limits the range of the battery powered aircraft; and the specific power (W/kg), that indicates the amount of power that can be obtained instantaneously from a determined amount of batteries. Therefore, it may represent a restriction certain flight phases such as take-off and climb. Nevertheless, there are other key parameters that must be taken into account when opting for a particular type of battery such as the life, the volumetric density and the price. Apart from the batteries, other sources for energy storage have been researched that could entail the future of powered aircraft. Some examples of these systems are the fuel cells [7], the flywheel [8] or the structural batteries [9].

The electric engines possesses several advantages with respect to the ICE. They produce less noise [10] due to the absence of combustion and they are simpler and more reliable, what reduces the maintenance cost [5]. Besides, they do not require warming up, they supply the power instantly and they do not depend on the size to provide good performance [5]. Different architectures can be implemented depending on the role that these electric engines play. If a full-electric architecture is used the aircraft is powered by electric

engines that receive the electricity directly from the storage. When part of the energy to power the aircraft is obtained through more than one energy source (e.g. fuel and electricity) it is denominated hybrid-electric architecture. Finally, when the aircraft is powered by electric engines but the electricity is obtained from a combustion engine it is called turboelectric architecture. A detailed visualization of these architectures can be found in figure

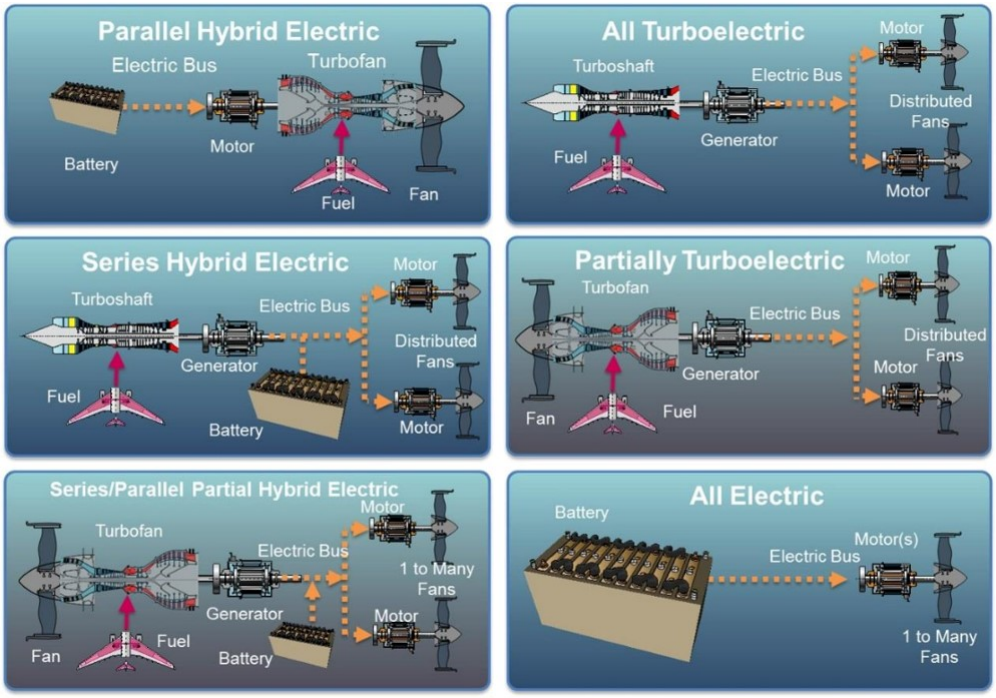

Figure 1.2: Different architectures for the power system of sustainable aircraft [11].

Apart from the benefits that the use of electric engines provide in terms of reduction of noise and lower maintenance costs, the fact that the transmission from the energy source to the electric engine is made by wires and the higher specific power these engines [12] opens the door for the concept of Distributed Electric Propulsion (DEP) in small aircraft. It consists of placing the electric engines strategically to obtain additional benefit of the interaction of the engine with the flow that surrounds the airframe. Some of these configurations are the concepts of wingtip mounted propellers, boundary-layer ingestion and leading-edge distributed propulsion.

The concept of wingtip mounted propeller consist of placing the propeller engines on the tip of the wing so it interacts with the wingtip vortex. Although initial studies suggested an increase in the performance of the propeller and a reduction of induced drag, later studies indicate that a distinction should be made depending on if the propeller is in

tractor or pusher configuration because it reduces the induced drag or increases the propeller efficiency, respectively [13]. Other advantages of this concept are the reduction in passenger perceived noise due to the increased distance from the fuselage as compared to conventional layouts [14] and the reduced probability of impact of a blade with the fuselage in the case of blade loss[15]. This concept could entail some disadvantages, for example, from an aeroelastic point of view because of flutter due to the change in the torsion moment of inertia and the bending and torsion modes coupling [15]. The main problems of the wingtip-mounted propellers are the directional control after engine failure due to the big asymmetric moment generated because of the distance with respect to the fuselage and the ground clearance [14][15].

The concept of boundary-layer ingestion resides in placing the electric engines in the rear part of the fuselage to make the engine ingest part of the boundary layer of the fuselage. Since the air that is part of the boundary layer has less energy than the freestream flow, the change in momentum is higher compared to a propeller in freestream conditions for the same power, hence, it increases the propulsive efficiency [16]. However, the increase in efficiency may be mitigated by the increase in fuselage drag and the weight penalty [17]. Another advantage could be that less wetted area is obtained because the nacelles are embedded in the fuselage, hence, less friction drag.

The concept of leading-edge distributed propulsion is based on placing the engines in the leading-edge of the wing along the span in order to use the propeller slipstream to create additional lift. This technology could be used in determined flight phases when high lift is required and would not work during cruise to achieve laminar flow on the wing and, hence, reduce the drag [18]. However, the technology could be also used in cruise conditions, because, if part of the lift is generated due to propeller slipstream, a wing with less chord can be used that enhances the aerodynamic efficiency when maintaining the same span. The concept could be implemented together with a flap in order to achieve very high lift coefficients or, instead of it, to obtain a simple wing. The working principle behind this concept is blowing the wings to create lift, what induces a new degree of freedom for producing lift that must be taken into account when designing the aircraft. This system, apart from increasing the maximum lift coefficient and allowing for smaller wings, when used for all flight phases, entails an advantage when balancing the aircraft after engine failure because the asymmetry generated due to the thrust force could be used to counteract instead of the vertical tail, meaning that the tail could be reduced or maybe eliminated [19].

1.1. MOTIVATION AND THESIS OBJECTIVE

Having analyzed all the advantages that result from distributed electric propulsion, a question arises: Which one is the most promising one? The answer to this question depends on the type of aircraft and the timeframe targeted. Taking into account the current state-of-the-art of the battery technology and other sources of energy [6], the

incorporation of the distributed electric propulsion on aviation could only be implemented depending on the degree of hybridization of energy [20], meaning how much of the energy used to power the aircraft is electric. Therefore, it is able to develop an all-electric aircraft only when it is small, including urban air mobility concepts, but it is also possible in bigger concepts with hybrid-electric architectures. Due to its high-lift capabilities that are important for STOL aircraft (again, urban air mobility development) combined with increased safety and aerodynamic efficiency, the concept of leading-edge distributed propulsion seems to be a promising technology in the development of distributed electric propulsion aircraft and serves as a demonstrator for bigger aircraft in the coming years.

Various studies have been conducted to obtain a better understanding of the leading-edge distributed propulsion systems. The interaction between the propeller slipstream and the wing has been studying by analyzing the sensitivity of the relative position of the propeller with respect to the leading-edge [21]–[24]. The spanwise position of the propellers and its direction of rotation has been also assessed in a experimental [21] and numerical [25] way.

Nevertheless, there is a gap in literature concerning the effect of the flap position on the propeller-wing-flap interaction. Only few numerical [26][27] and experimental [28] studies have been conducted where flap deflection is assessed. In conclusion, since the flap position plays an important role in high-lift systems with distributed propulsion, analyzing the effect that this geometrical parameter has on the aerodynamics of propeller-wing-flap systems is envisioned as a promising research direction that could find its application in electric (or hybrid-electric) regional aircraft or urban air mobility during the next decade.

Once the topic is defined, the next question that arises is: what is the most appropriate approach to assess the effect of flap position in leading-edge distributed propulsion systems? A low-order method would be ideal to test the different positions since the analysis is computationally fast. However, since these methods are based on inviscid aerodynamic models coupled with propeller aerodynamic theories, there are not able to predict stall accurately and they rely on airfoil data to estimate viscous drag [29][30][26][27]. A high-order method would be more appropriate to obtain more accurate results, although it is computationally expensive to test different configurations. In conclusion, a wind tunnel experiment is proposed to assess the effect of flap position in leading-edge distributed propulsion systems. Examples of wind tunnel experiments to assess the effect of the different design parameters can be found in literature [21]–[23].

In conclusion, the fundamental research objective that emerges from the gap in literature is to **gain insight into the aerodynamic interaction effects in propeller-wing-flap systems with leading-edge distributed propulsion, and to assess how this interaction changes with flap position.**

Within the main research objective, the following sub-goals are assessed in this thesis:

- What is the effect of using multiple propellers on the wing loading distribution, when compared to a single-propeller case?
- What is the effect of the flap position on the change in aerodynamic coefficients due to slipstream effects?
- How does the flap deflection affect the wake downstream of the system?

1.2. THESIS OUTLINE

The present thesis is structured in six chapters. Chapter 2 collects all the theoretical knowledge necessary to understand the concepts studied in the experiment. The topics covered are: propeller aerodynamics, high-lift aerodynamics, the interaction between components and the effect of the design parameters on the aerodynamic coefficients. Chapter 3 covers the design of the model and its installation, the wind tunnel facilities where it takes place and under what conditions, and the manner in which the data are obtained and processed. Chapter 4 is the first of the two chapter of results and presents all the results regarding the aerodynamic interaction in leading-edge distributed-propulsion systems when the flap is retracted. Chapter 5 assesses the effect of flap position in propeller-wing-flap systems with leading-edge distributed propulsion. Finally, in Chapter 6 the conclusions extracted from the results are summarized.

2

THEORETICAL BACKGROUND

This chapter is divided into four different sections that establish the foundation for understanding the interaction between propeller and flap in DEP configurations. The first section treats the analysis methods for propellers and it covers the Momentum Theory, the Blade Element Method and the Vortex Theory. The second section focuses on the aerodynamics of trailing-edge high-lift devices. Finally, the third section focus on the interference between components, that is, on propeller-wing interaction, propeller-flap interaction and propeller-propeller interaction.

2.1. PROPELLER AERODYNAMICS

A simple way to understand the working principle of a propeller is using the momentum theory [31]. This theory, also known as actuator disk theory, defines the propeller as a porous disk of a determined area (A) that produces thrust (T). It assumes that the thrust is uniformly distributed over the disk. The disk accelerates the flow only in the axial direction, so no swirl is considered. Figure (2.1) visualizes the scheme of the streamtube that passes through the disk. Four sections can be distinguished. The first section is the incoming flow with a determined static pressure. The second section corresponds to the flow before the propeller, where the velocity of the flow is increased by a velocity induced by the propeller. Section three is located immediately after the propeller and it is different from section two because the static pressure is increased by a Δp. Finally, the last section accounts for the flow with a velocity higher than the incoming one but with the pressure equals to the freestream static pressure.

This theory assumes incompressible flow, hence, the Bernouilli equation is applied in the

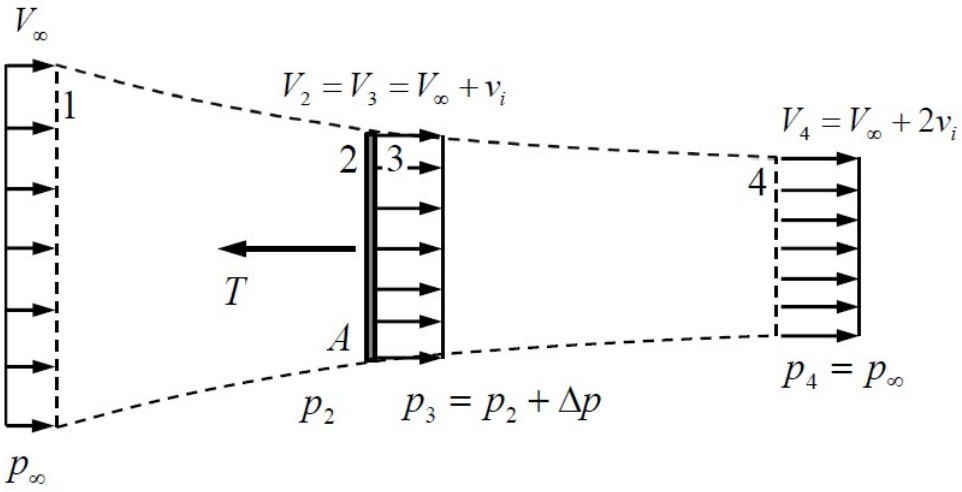

Figure 2.1: Flow passing through a propeller[18].

section upstream of the propeller (Eq. (2.1)) and downstream of the propeller ((2.2)).

$$p_\infty + \frac{1}{2}\rho V_\infty^2 = p_2 + \frac{1}{2}\rho V_2^2 \tag{2.1}$$

$$p_\infty + \frac{1}{2}\rho V_4^2 = p_2 + \Delta p + \frac{1}{2}\rho V_2^2 \tag{2.2}$$

If the streamtube is selected as a control surface and the continuity equation is applied, a expression of the thrust can be obtained ((2.3)). The thrust can also be expressed as a change in velocity or as a pressure jump.

$$T = \rho\pi R_4^2 V_4(V_4 - V_\infty) = \rho A V_2(V_4 - V_\infty) = \dot{m}\Delta V = A\Delta p \tag{2.3}$$

An expression for the required power can be derived. Nevertheless, this power is less than the power required to spin the propeller, because the momentum theory does not consider losses due to profile drag or trailing vortices [18].

$$P_i = \frac{1}{2}\dot{m}(V_4^2 - V_\infty^2) = T(V_\infty + v_i) \tag{2.4}$$

From equations (2.4) and (2.3) it can be extracted that the velocity in section 4 equals the incoming velocity plus two times the induced velocity by the propeller in the location of the propeller disk. Summarizing, the velocity in each of the sections is expressed in terms of the incoming velocity in figure (2.1).

The greatest limitation of this theory is that it does not consider the design of individual blades and the absence of swirl. Nevertheless, it could be a powerful tool when estimating the thrust or trying to evaluate axial velocity, specially in early design phases.

The flow downstream of the propeller is known as slipstream. The velocities present in the slipstream have three components: the axial component, the tangential component and the radial component.

The axial component of the velocity is the main velocity induced by the propeller. This is the only induced velocity desired as it is the one that contributes to the thrust. A representative representation of the axial velocity distribution along a blade can be seen in figure (2.2).

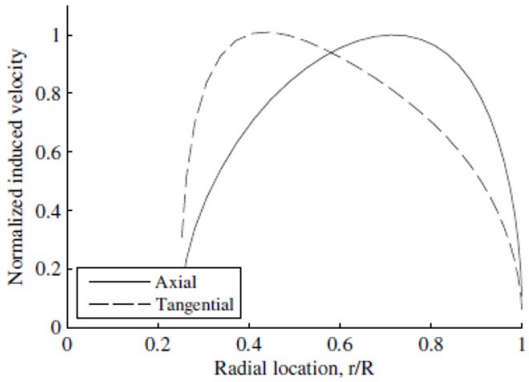

Figure 2.2: Representative representation of the axial and tangential normalized induced velocities vs. radial location.[18]

The tangential component of the velocity is called swirl and is produced by the bound vorticity on the blades in vortex system and the viscous drag of the blades. Contrary to the axial velocity, the swirl is not useful for producing thrust, therefore, it is desired to reduce the swirl. A typical distribution of the tangential velocity can be appreciated in figure (2.2). The higher tangential velocity is located near the root and diminishes when moving to the propeller tip. The swirl angle can be seen as the deviation of the flow from the axial direction:

$$\theta_{\text{swirl}} = \arctan \frac{V_{\text{t}}}{V_{\infty} + V_{\text{a}}} \tag{2.5}$$

The radial component of the velocity is mainly due to the contraction that the slipstream experiments. In lightly loaded propellers the contraction of the slipstream is on the order of 1% [32], therefore this velocity is sometimes neglected without compromising the calculations.

The pressure distribution changes throughout the slipstream. The effect of the propeller is to increase both static and total pressure of the flow. Since not all the flow is accelerated in axial direction, the total pressure rise is higher than the rise of static pressure. The difference between the cases with and without contraction of the slipstream is equivalent to $\frac{1}{2}\rho V_t^2$ [21]. In the same way as the axial and tangential velocity, the total and static

pressures vary in the radial direction, as shown in figure (2.3).

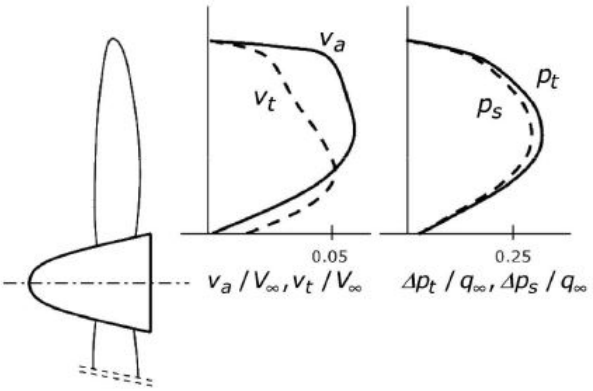

Figure 2.3: Typical radial distribution of axial velocity, tangential velocity, total pressure and static pressure directly behind a 6 bladed lightly loaded propeller. [21]

Since the momentum theory only takes into account the axial component of the velocity, there is another method called the blade element method [31]. This method is useful when the detailed shape of the blade is of interest. The blade is divided into differential sections or elements as if they were airfoils with length dr. Each element has its own flow properties and geometry that generates a differential lift and a differential drag. It is assumed that no interaction takes place between elements and the differential lift and drag are purely two-dimensional. The velocity that sees the element (v_r) is compound by two velocities, the axial velocity (v_a) and the tangential velocity (v_t):

$$v_a = V_\infty(1+a) \tag{2.6}$$

$$v_t = \Omega r(1-a') \tag{2.7}$$

Where a is the axial induction factor and it is defined as the ratio between induced velocity and freesetream velocity; a' is the tangential induction factor and it is defined as the ratio between the local angular velocity and the angular velocity of the propeller. In order to obtain the total thrust and torque, an integration must be performed along the blade. Nevertheless, the induced velocity by the propeller is unknown when integrating, therefore, the blade element method is usually combined with momentum theory to create the blade element momentum theory. The propeller disk is divided into annular rings of thickness dr and the torque and the thrust are calculated using momentum theory.

However, this combined theory does not consider the influence of the vortices shed from the blade tips into the slipstream. That is the reason why a tip-loss correction factor (F) is sometimes used that provides the circulation for minimum vortex energy loss at a given radial station [33] to account for the finite number of blades and zero loading towards the tip:

$$F = \frac{2}{\pi} \arccos e^{\frac{-N}{2} \frac{R-r}{R \sin \phi_T}} \tag{2.8}$$

Where r is the local radial location and ϕ_T the helix angle at the tip. This correction factor provides higher accuracy with a high number of blades and large ratios of propeller tip speed to freestream speed [18]. The induced factors presented in equations (2.6) and (2.7) can be expressed in the following way as a function of the helix angle:

$$a = \left[\frac{4F \sin^2 \phi}{\sigma (C_L \cos \phi - C_D \sin \phi)} - 1 \right]^{-1} \tag{2.9}$$

$$a' = \left[\frac{4F \sin \phi \cos \phi}{\sigma (C_L \sin \phi - C_D \cos \phi)} + 1 \right]^{-1} \tag{2.10}$$

Where σ is the solidity of the blade, defined as the ratio area of the propeller blades to the area of the propeller disk.

2.2. HIGH-LIFT AERODYNAMICS

The high-lift propellers can be combined with trailing edge high-lift devices [34] to maximize the lift generation. This subsection covers the theory behind high-lift aerodynamics and provides an analysis of different high-lift configurations that can be employed.

Lift is the most important force in aeronautics as it is required to maintain an aircraft in the air. This force may be required to be very high in flight phases where there is low velocity. The lift force is non-dimensionalized with the dynamic pressure and the reference area to obtain the lift coefficient. Nevertheless, the value that the lift coefficient could have is limited by the potential flow theory. If inviscid flow around a circle is considered, where there is no separation, the circulation could be so strong that front and rear stagnation point coincide. In this case the lift coefficient that is obtained is 4π, and it indicates the maximum theoretical lift coefficient that can be achieved using potential flow theory. In practice, since the flow is viscous, rotational and compressible; the lift coefficients are usually much lower.

The reality is that the maximum lift coefficient is governed by the boundary layer separation that takes place when viscous flow is considered. Therefore, trying to predict separation is crucial when evaluating high lift. Stratford [35] provides a limit that indicates the maximum pressure coefficient that can be attained without separation. This is known as the Stratford limit. It provides the pressure coefficient distribution that can be obtained on an airfoil with a determined margin before separation. This limit is a function of the Reynolds number based on the airfoil chord and the trailing-edge pressure coefficient. In figure (2.4), an example of the Stratford limit can be seen. Since the lower surface is not

prone to separation, it is desired to have a velocity as low as possible to obtain maximum lift. More information regarding the Stratford limit can be found in references [36],[35] and [37].

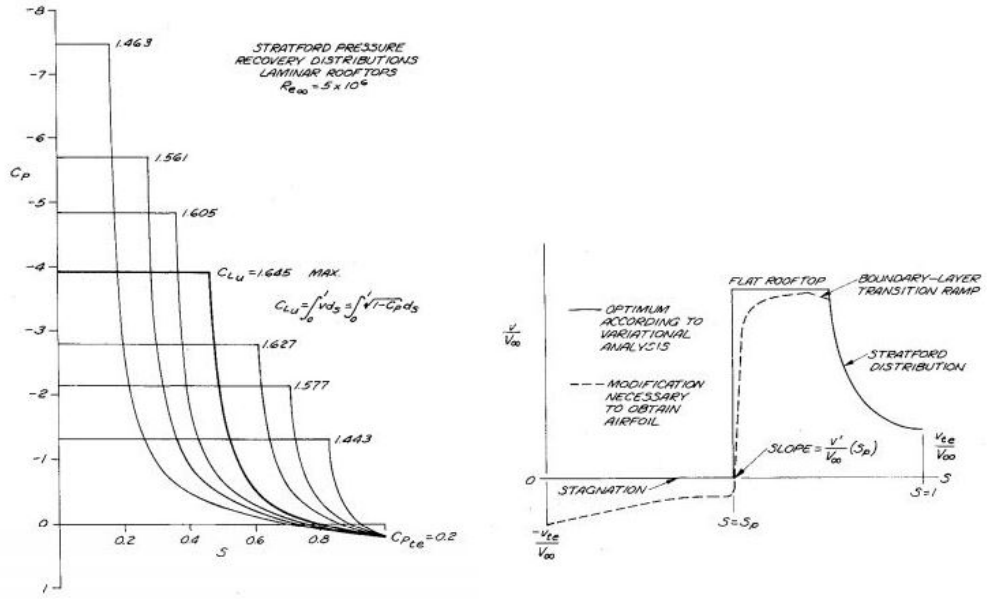

Figure 2.4: On the left side, Stratford pressure distribution on the suction side for $C_{p_{\text{te}}} = 0.2$ and $Re = 5x10^6$. On the right side, optimum airfoil velocity distribution and the modification required to obtain an airfoil shape. Both figures are extracted from [36].

If the pressure recovery starts too late there is not enough space for the flow to slow down without separation. Therefore, the concept of multi-element airfoils plays an important role when attempting to achieve high lift without separation. When two airfoils are placed close to each other, the flow of the first element discharges in a region where the flow has higher velocity compared to the freestream flow due to the presence of the second element. Consequently, the pressure rise is lower, decreasing the possibility of separation, this is known as the dumping effect. There is also an effect of the circulation of the downstream element on the upstream element because it induces velocities on the latter. Thus, in order to achieve the Kutta condition the circulation is increased, this results in higher pressure peak (specially near the trailing edge) and a decrease of the velocities of the lower surface. There is also an effect known as off-the-surface pressure recovery. This effect takes place when the boundary layer that leaves the trailing edge becomes a wake that, when recovering back to freestream away from being in contact with the wall it is done in a more efficient way. Finally, there is a fresh boundary layer that is created due to the slot that can withstand higher adverse pressure gradient since new boundary layers are thinner.

2.3. AERODYNAMIC INTERACTION BETWEEN COMPONENTS OF THE LEDP SYSTEM

2.3.1. EFFECT OF THE PROPELLER ON THE WING

Subsection (2.1) explains how the propeller changes the momentum of the flow in the axial and the tangential direction. This means that for propellers in a tractor position, the flow downstream of the propeller will have added velocities compared to the freestream flow due to the induced velocities by the propeller. Apart from the added velocities, the velocity field is different with respect to the freestream condition due to the existence of the tangential and radial velocities. In a similar way, the total and static pressure varies in axial and radial direction.

In summary, the two main effects of the slipstream are the change in velocity and effective angle of attack. The change in velocity increases the dynamic pressure, and, therefore, the lift is enhanced. This is the main purpose of the high-lift propellers. Increasing the velocity also means an increase in Reynolds number, which may delay stall, contributing to the main objective of this technology. However, since not all the flow is accelerated in axial direction, the swirl is responsible of modifying the angle of attack of the wing. The half of the propeller that rotates in upward direction tends to increase the angle of attack of the part of the wing downstream and the other half that rotates in downward direction decreases the angle of attack of the part of the wing downstream. To summarize, the lift is enhanced aft of the propeller due to the increase in dynamic pressure, and is further increased or decreased depending on the sense of rotation.

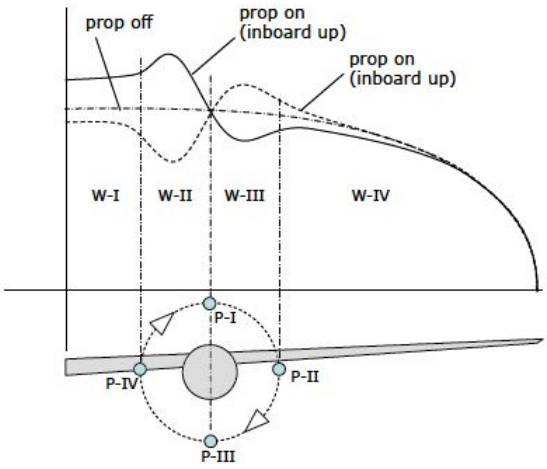

Figure 2.5: Effect of the axial and tangential velocities on the lift distribution over the wing [38].

Not only the lift distribution is affected in the region downwash of the propeller but

also in the region outside the propeller domain. The reason behind that is the spanwise change in lift, which leads to trailing vorticity. The trailing vortex sheet behind the wing subsequently alters the lift distribution. As can be seen in figure (2.5), the lift distribution is modified in areas W-I and W-IV depending on the sense of rotation, being the inboard up case the one that generates the most lift. The effects that the slipstream produces on the wing flow are magnified with the increase in propeller loading.

The presence of the wing alters the rotational symmetry of the slipstream. The boundary of the slipstream is sheared in lateral direction as it interacts with the wing, leading to a different spanwise position of the slipstream boundaries located in upper and lower surface. The result is that both halves displace in opposite direction (Fig. (2.6)).

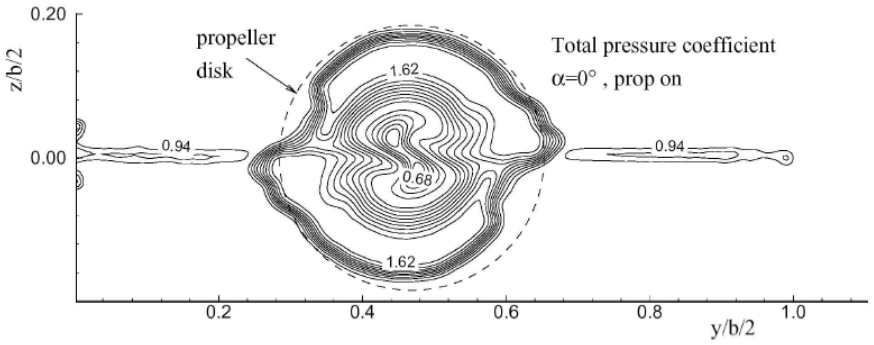

Figure 2.6: Slipstream deformation due to trailing vortices (propeller rotates in clockwise direction) [38].

There is also an influence of the propeller slipstream on the boundary layer over the wing. The boundary layer cycles between laminar and turbulent state at a rate equivalent to the blade passage frequency. This unsteady behaviour takes place because the wake resulting from a blade impacts the wing causing a turbulent transitional phase. After the wake, the boundary layer reverse to a laminar state. The effect that is derived from this transitional behaviour is an increase in friction drag compared to a condition where there is fully laminar flow, but not as much as the condition with fully turbulent flow [39].

2.3.2. EFFECT OF THE WING ON THE PROPELLER

The presence of the wing modifies the surrounding flow. Hence, it modifies the performance of the propeller. The circulation of the wing induces velocities in the upward direction upwash of the wing. Therefore, the propeller encounters a non-uniform flow field that tends to decrease the performance of the propeller. If we analyze figure (2.5), the angle of attack increases in the downgoing blade side (P-II) and decreases in the upgoing blade side (P-IV). The effect on regions P-I and P-III depends on the propeller height with respect to the wing [38]. This interaction is higher when the propeller is placed very close in axial direction with respect to the wing.

The presence of the wing on the slipstream created by the propeller acts as a stator vane that reduces the rotational velocity of the slipstream due to a change in the slipstream helix angle. The downwash produced by the wing reduces the angle of rotation behind the upgoing blade while the upwash of the wing reduces the rotation angle behind the downgoing blade. This effect is known as swirl recovery.

Another way of explaining swirl recovery is by analyzing the airfoil sections that are immersed in the slipstream of the upgoing and the downgoing blade. The upgoing blade induces upwash on the wing that increases the local angle of attack generating positive lift and negative drag. In the downgoing blade, the propeller induced downwash on the wing that decreases the ange of attack, generating negative lift and negative drag again. A negative component of the drag can be seen as an enhance in propeller performance or a reduction in swirl losses [21].

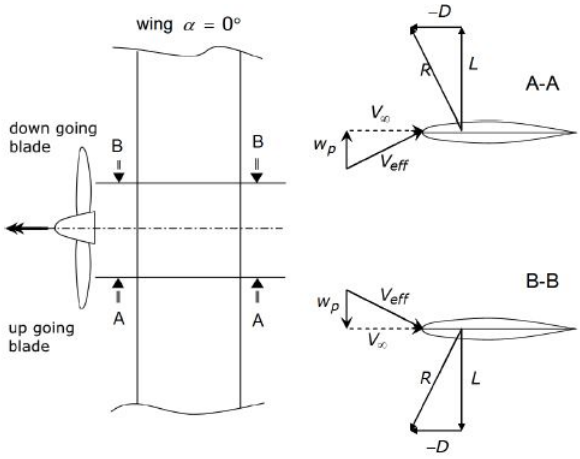

Figure 2.7: Swirl recovery on an infinite wing with symmetrical airfoils at zero angle of attack.[21]

The presence of the nacelle has an effect on the contraction of the slipstream. If the nacelle has a streamlined contour, the slipstream will follow this contour and the contraction could be magnified [18]. Apart from that, the nacelle induces a non-uniform axial velocity distribution on the propeller inflow that alters the load distribution on the blade, hence, modifying the thrust [21].

2.3.3. PROPELLER-FLAP INTERACTION

Since the deflection of the flap increases the circulation of the wing, the effects that have been explained regarding the interaction between the wing and the propeller are magnified. The effect of the flap on deflecting the slipstream of a propeller downwards has been studied for vertical and short take-off airplanes. Two parameters need to be defined: the turning angle (θ) and the thrust recovery factor (F/T).

The turning angle is the angle between the thrust axis and the deflected slipstream. The value of the turning angle is a function of the flap deflection angle, the type of flap and the ratio between the extended flap chord and the propeller diameter. In Ref. [40], two parameters that are derived from the turning angle are used. The first one is the turning angle per degree deflection (θ/δ). This slope is only dependent on the flap chord and the type of flap. The other parameter is the maximum turning angle. To obtain high angles, it is necessary to use multiple flaps and either slots or a large radii at the knee of the flap, as it is employed when using flaps that increase the chord.

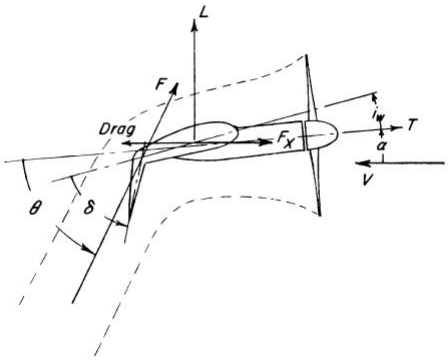

Figure 2.8: Flap deflection of the slisptream.[40]

The thrust recovery factor is the part of the thrust that remains after the loss of momentum in the flow due to viscous effect. It is a function of the turning angle, the flap configuration and the propeller arrangement. The best thrust recovery factor is obtained with slotted flap, probably due to the fresh boundary layer, according to [40]. The Fowler flaps provide higher thrust recovery factor because the turning process is farther forward on the wing [40]. Now that both magnitudes have been presented, the total lift and horizontal force can be expressed in the following way:

$$L = \frac{F}{T} NT \sin(\theta + \alpha) \tag{2.11}$$

$$F_x = \frac{F}{T} NT \cos(\theta + \alpha) \tag{2.12}$$

In conclusion, when assessing the lift of a propeller-wing-flap system, three contributions must be distinguished: the power-off lift, the additional lift generated on the wing due to the propeller slipstream (due to increased mass flow) and the direct thrust. The three contributions can be appreciated in figure (2.9), where the lift coefficient is expressed as a function of the thrust coefficient.

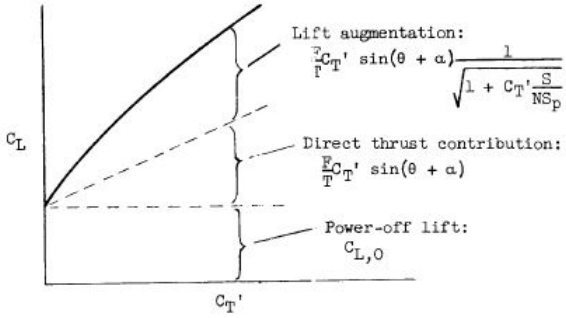

Figure 2.9: Three contributions to the lift coefficient in propeller-wing-flap systems.[40]

2.3.4. PROPELLER-PROPELLER INTERACTION

The interaction that takes place between to propellers close to each other or even overlapping propellers is a field with limited information available. When the propellers are overlapped, the rear one ingests the wake of the other. This slipstream has increased axial velocity; therefore, the rear propeller produces less change of momentum and, hence, less thrust. The main factor that governs this loss of thrust is the lateral distance between the centerlines of the propellers, so the more the overlapped area the more the loss of thrust. According to Ref. [41], the interaction between propellers takes place only for propellers that are very close, although the effect in thrust coefficient is practically negligible. Nevertheless, the complex flow interaction that takes place between propeller slipstreams generate thrust fluctuations.

2.4. EFFECT OF THE DESIGN PARAMETERS ON THE AERODYNAMIC COEFFICIENTS

A representation of the parameters that comprise the design of propeller-wing-flap system can be found in figure (2.10). There are parameters related to the size of the propeller and its position with respect to the airfoil and there are parameters related to the size of the flap and its position with respect to the airfoil. The criteria used for the flap geometry definition is extracted from [42].

When the impact of the diameter-to-chord (D_p/c) ratio in obtaining high-lift is assessed [34], it is found that the blown to unblown C_L ratio increased as the chord was decreased, but the increase in relative size of the nacelle to the wing impacted wing lift performance. That is the reason why the study indicated that a propeller diameter to wing chord ratio of 1.0 gives the overall best maximum lift on the wing with the DEP system. In figure (2.11) it can be seen that the higher the propeller diameter, the higher the effective lift coefficient, because for the same value of the rest of the parameters a higher lift coefficient is obtained

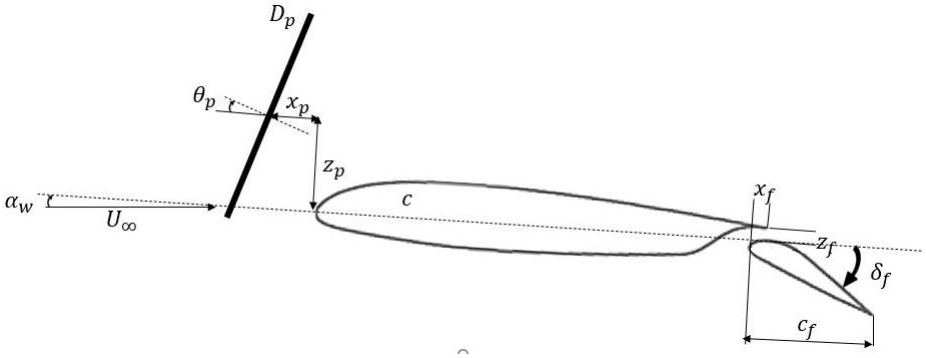

Figure 2.10: 2D model of the concept of high-lift propeller.

when moving from a propeller diameter-to-chord ratio of 1 to 1.8.

The position of the propeller with respect to the airfoil leading edge in the chordwise direction (x_p) does not have an important effect on the performance of both the propeller and the wing for positions well ahead in front of the wing leading edge. If the distance with respect to the wing is increased there is a small benefit in the propulsive efficiency of the propeller [21]. Increasing this distance enhances the lift coefficient without modifying the slope and increases the drag coefficient [22]. Nevertheless, it has low effect on the peak lift coefficient, therefore it may be optimized with cruise conditions [23]. For chordwise positions of the propeller very close to the wing, strong interference effects take place [21].

The effect of the vertical position of the propeller with respect to the airfoil leading edge (z_p) is more significant than the horizontal position. High values of z_p, which means that the propeller is above the airfoil, lead to higher values of lift coefficient [22]. If the propeller is aligned with the airfoil, a smaller part of the wing is washed by the slipstream annulus, producing minimum drag coefficient [21]. For increasing the propulsive efficiency of the propeller it is better to place the propeller in a position under the wing because the propeller inflow distortion is reduced [21].

Sometimes the vertical position of the propeller is non-dimensionalized with the propeller radius. The value of this parameter for which the lift coefficient is maximum decreases when increasing the angle of attack or the flap deflection because more slipstream cross-sectional area impinge upon the wing [23]. A linear relation seems to exist between the unblown lift coefficient and the optimum propeller height, as shown in figure (2.12).

The propeller inclination angle (i_p) is defined as the angle between the propeller centerline and the chord. It must be taken into account which criteria is used when defining positive inclination angles, in this report, the criteria used is the one reflected in figure (2.10). Decreasing the value of the inclination angle (to negative values) produces a big increase

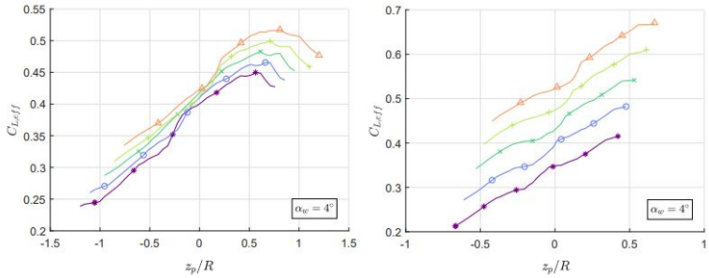

Figure 2.11: Lift coefficient vs. propeller height for an angle of attack of 4°, $\delta_f = 0°$, $x_p = 9''$ and $J = 0.4$. $D/c = 1$ (left), $D_p = 1.8$ (right). [23]. Note that both axis are in different scale.

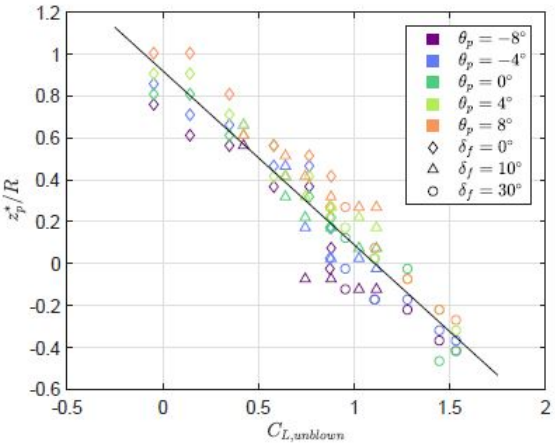

Figure 2.12: Unblown lift coefficient vs. optimum propeller height for $J = 0.4$ and. $D_p = 10''$. [23]

on the lift coefficient [22]. Other studies suggest that the benefit in the lift coefficient takes place beyond 15° in the negative sense [21]. Nevertheless, it must be taken into account that the increase in lift coefficient depends on if the propulsive forces on the lift direction are taken into account [23], because, despite negative inclination angles may be better for enhancing lift, since the propeller would be tilted, the thrust vector would have a component opposite to lift. The influence of the propeller inclination angle on the wing lift coefficient seems to disappear for values of the non-dimensional propeller vertical position beyond the optimum value [23].

While the 2D parameters seem to hve an impact on the aerodynamic coefficients, the spanwise position of the propeller seems to have a negligible effect in rectangular wings except from very particular positions such as near the tip, where the presence of the tip vortex has a strong influence on the performance of the propeller [21].

Apart from the relative location of the propeller with respect to the wing, the direction

of rotation of the propellers has been studied in Ref. [25], two approaches can be distinguished: the case where the propellers are corrotating or the case where the propellers are counterrrotating. The corrotating approach provides higher values of L/D when all the propellers spin in the inboard up direction.

3

EXPERIMENTAL SET-UP

In this chapter, all the aspects regarding the experimental set-up are covered. First, the propeller-wing-flap system is shown together with the design decisions concerning dimensions and relative position between the different components. Second, the wind -tunnel facility where the experiment takes place is presented. Third, a explanation of how the model is installed in the wind tunnel is provided. Then, the operating conditions of the experiment and the different configurations tested are presented. Finally, the measurement techniques used during the campaign are explained together with the way that the data provided is processed.

3.1. DESIGN OF THE PROPELLER-WING-FLAP SYSTEM

In this section, the design process of the propeller-wing-flap system is addressed. The conceptual design of the whole system is presented. This stage of the design comprises the layout of the system, the general dimensions of the wing, flap and propeller, including the relative position between them.

Similar to other experimental research conducted to test propeller-wing interaction ([21]–[23], [28]) the model consists of a semi-span rectangular wing for simplicity. The main difference with respect to other experiments is the presence of more than one propeller. The system is provided with three propellers placed in the leading-edge in order to evaluate the impact of these distributed-propulsion systems when compared with the case of a single propeller. That is the reason why the propellers (together with the nacelle) must be removable, allowing to test the wing in a clean configuration with neither propeller nor nacelle. This capability of having a clean wing configuration allows

to identify the effect of the nacelle on the aerodynamic coefficients. A representation of the model can be found in figure (3.1) The propeller chosen for this experiment is the TUD-XPROP-S, which have been used in previous experiments conducted by the propeller research group at TU Delft for testing isolated propeller performance and propeller integration [43]. The propeller consists of a six-bladed propeller with a diameter of 0.203 m.

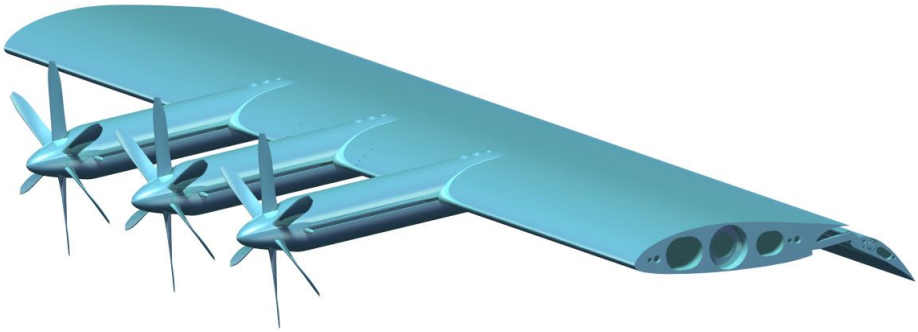

Figure 3.1: Rendered representation of the model.

To facilitate future research with the same model, the span of the model is restricted to the dimensions of the LTT Wind Tunnel at TU Delft, therefore the span measures 1.248 m to fit into the 1.25 m height of the LTT Wind tunnel.

As explained in section (2.4), one of the most important coefficients regarding distributed propulsion systems is the diameter of the propeller to the wing chord ratio. In that section, it is also mentioned how a diameter-to-chord ratio between 0.5 and 1 is appropriate for distributed propulsion systems. It is also concluded that, on one hand, it is desired to have a diameter-to-chord as large as possible. Nevertheless, a compromise must be established because the propeller diameter is fixed, consequently, the wing chord should be very small, which lead to a very low Reynolds number that could entail separation issues, specially on the flap due to its reduced chord and the presence of the slot, where the Reynolds number may play an important role . Besides, a very small wing means that the support may not be able to withstand the loads generated in high lift conditions.

In order to select the chord of the model, a similarity is established between a conventional regional propeller-driven aircraft and its distributed propulsion version. The aircraft ATR-42 [44] has a propeller diameter of 3.93 m, which leads to a propeller disk area of 12.1 m^2. If it is assumed that the ATR-42 has distributed propulsion with the same disk area of the original one, six propellers per semispan could fit taking into account that only 75% of the span can be used (Fig. (3.2)) . Each of the propellers would have a diameter of 1.49 m for a wing of 2.25 m of mean chord, what leads to a diameter-to-chord ratio of 0.66. This diameter-to-chord ratio means that the chord has a value of 0.3 m.

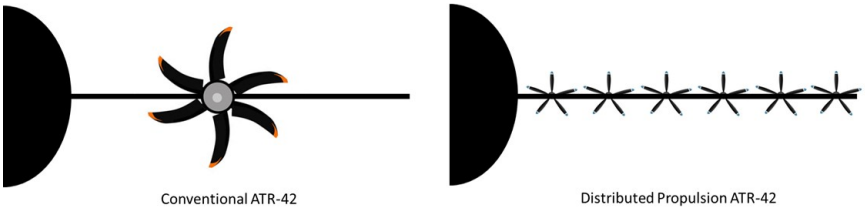

Figure 3.2: Conventional ATR-42 vs. ATR-42 with distributed propulsion

As commented in section (2.4), since the horizontal position of the propeller with respect to the leading-edge does not have an important effect on the performance, the decision of this position is made just taking into account that enough space is needed for the electric engine, a value of 1.8R is therefore selected. In order to decide the inclination of the propeller together with its vertical position with respect to the leading edge, the velocity field of the airfoil is analyzed using XFOIL assuming cruise condition with a lift coefficient of 0.5. It is desired to match the propeller inclination angle with the local flow direction to have the propeller aligned with the freestream flow in cruise conditions. The analyses provides an inclination value of roughly -5 deg at a location of 0.155R below the leading-edge; which, not only provides a higher effective angle of attack, but also avoids an extremely high position of the propeller with respect to the leading edge at high angles of attack that would mean that a large portion of the slipstream flows over the wing.

The airfoil selected is the NLF-MOD22, designed at Delft University of Technology for low-speed applications [45]. This airfoil has been selected among other low-speed airfoils because it has a thickness-to-chord ratio of 17%. Having a thick profile can be beneficial in terms of stall regarding the low chord value. Apart from that, in Boermans and Rutten report [45], the NLF-MOD22 airfoil is tested with a Fowler flap for various flap positions. The report therefore serves as a baseline for the experiment to compare the effect of flap position with and without the effect of slipstream. In the report, two configurations are tested: configuration A has a smooth slot entry shape with large gap in the lower surface when the flap is retracted, configuration B has a sharp slot entry shape with small gap in the lower surface when the flap is retracted. Configuration B is chosen to reduce the influence of the slot on the aerodynamic coefficients in flap retracted configuration. The shape of the airfoil is represented in figure (3.3). The design parameters are summarized in table (3.1).

As commented in section (2.4), the flap position is defined by three parameters: flap deflection, overlap (x_f) and gap (z_f). Three flap deflections (apart from the flap retracted) are selected to represent three configurations similarly to the flap deflection tested in Boermanns and Rutten report [45]: take-off (15 deg), medium flap deflection (30 deg) and full-flap deflection (40 deg). In the case of the full-flap configuration, three gap values are tested (2%c, 3%c and 5%c) since previous research has shown that there is an optimum value of the gap for achieving maximum lift coefficient ([46], [47]). The values are also selected based on previous research because the position of optimum gap position seems

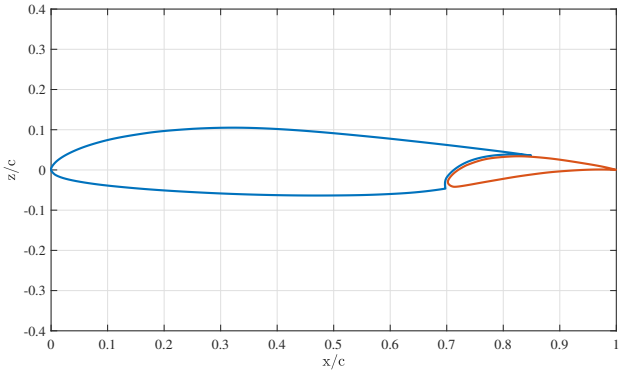

Figure 3.3: NLF-MOD22B airfoil with flap retracted[45].

to decrease with increased Reynolds number [48]. Since the slipstream accelerates the flow in axial direction, an increase of Reynolds number is expected, making the optimum gap values for this model lower than the values of Boermans and Rutten report [45]. The choice of the overlap seems to be less critical than the choice of gap [48], so two overlaps (0% and 1%c) are tested for two of the gap values (2%c and 3%c). Two additional gap positions are tested (17.85%c and 10%c); in the first position, the flap is placed under the wing where the maximum slipstream velocity is expected to test if that position produces the maximum lift coefficient. The second additional position is defined as an intermediate position between the position where maximum slipstream velocity is expected and the typical ones.

In order to test the effect of flap deflection, in the medium flap deflection (30 deg) configuration the values for overlap and gap are selected ensuring that the same values are tested for the full-flap deflection (40 deg) configuration. When increasing flap deflection the values of overlap and gap for maximum flap position are reduced [46], the positions selected are therefore the ones in table (3.2). The last flap position selected is the one corresponding to take-off position with the values of overlap and gap similar to the ones tested by Boermans and Rutten [45].

A structural analysis using finite element method (FEM) is made as part of the requirements necessary to ensure safe operation during the wind tunnel test campaign. As it is not part of the research question but necessary in the design of the model, the methodology used for the structural calculation is presented in Appendix (B).

Wing	
Span (mm)	1248
Aspect ratio	4.16
Chord (mm)	300
Taper ratio	0
Sweep (deg)	0
Airfoil	NLF-MOD22B
t/c	0.17
Propeller	
Number of propeller	3
Diameter (mm)	203
Horizontal position	1.8R
Vertical position	0.155R
Inclination angle (deg)	-5
Tip clearance (mm)	5

Table 3.1: Main design parameters of the model.

Flap Position	Overlap	Gap	Deflection
FP1	8%c	2%c	15 deg
FP2	0%c	2%c	30 deg
FP3	0%c	3%c	30 deg
FP4	1%c	3%c	30 deg
FP5	0%c	2%c	40 deg
FP6	0%c	3%c	40 deg
FP7	0%c	5%c	40 deg
FP8	0%c	10%c	40 deg
FP9	0%c	17.85%c	40 deg
FP10	1%c	2%c	40 deg
FP11	1%c	3%c	40 deg

Table 3.2: Flap positions tested in the experiment.

3.2. WIND-TUNNEL FACILITY

The test is conducted in the Low-Speed Tunnel (LST) [49] at the DNW facilities in Marknesse, the Netherlands. It consists of a closed-type wind tunnel with a rectangular test section of 3 m x 2.25 m. The wind-tunnel operates at atmospheric conditions. The operating range of the wind tunnel goes from 0 to 80 m/s. There is a 1:9 contraction ratio after the setting chamber. The turbulence level of the wind is 0.03% of the velocity in the y and z direction (both directions define the section of the wind tunnel) and 0.02% in the longitudinal direction (freestream direction) for wind speed up to 60 m/s. The wind-tunnel is adapted to test different types of models: turntables in top and bottom wall for 2D testing, sting support for internal balance or six-component overhead balance for 3D balance [49]. An aerial view of the tunnel can be found in figure (3.4).

Figure 3.4: Aerial view of the DNW-LST Wind tunnel.

3.3. MODEL INSTALLATION

The wind-tunnel model consists of two main parts, the wing and the table. A schematic view of the wind-tunnel assembly can be found in figure (3.5) and a front picture in figure (3.7). The first part is the wing model mounted on the beam assembly that is attached to the balance. The balance is placed in a rotating plate in the ceiling to modify the angle of attack. There are three types of configurations that can be tested: the distributed propulsion wing, the propeller-off wing and the clean wing. The distributed propulsion wing (Fig. (3.6a)) has the propellers mounted and operating. In the propeller-off wing configuration (3.6c) the propellers are removed but the nacelles are still mounted. Finally, the clean wing (Fig. (3.6b)) does not have propellers nor nacelles, leading-edge caps are placed instead to leave the wing with its original shape.

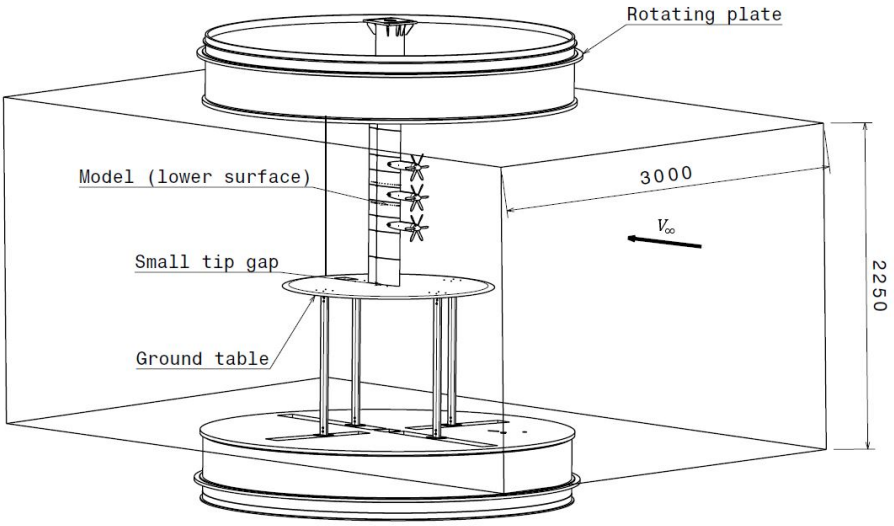

Figure 3.5: Wind-tunnel assembly.

The second part is the ground table. This table is attached to the floor and acts as an end plate. The purpose of this arrangement is to try to reproduce 2D conditions as much as possible by hindering the flow to go from lower to upper surface at the tip of the wing. This type of model is therefore known as a 2.5D configuration. In reality, since the model cannot be attached to the table in order to measure forces and moments with the balance, a small gap is left at the tip. That is the reason why the model has a span of 1.248 m, that added to the gap size (2 mm) and the height of the table (1 m), provides the total height of the wind-tunnel section (2.25 m).

In order to avoid 3D flow effects at the corner between the model and the ceiling, 3D printed fairings are placed at the root to smooth the pass of the air. The fairing have the same shape as the airfoil with a 2 mm offset to avoid the contact between fairing and

(a) with Distributed Propulsion.

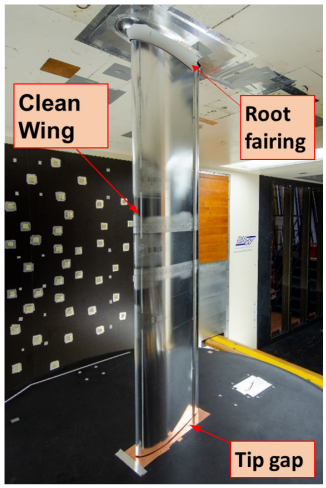

(b) in clean wing configuration.

(c) in prop-off configuration.

Figure 3.6: Picture of the wing model.

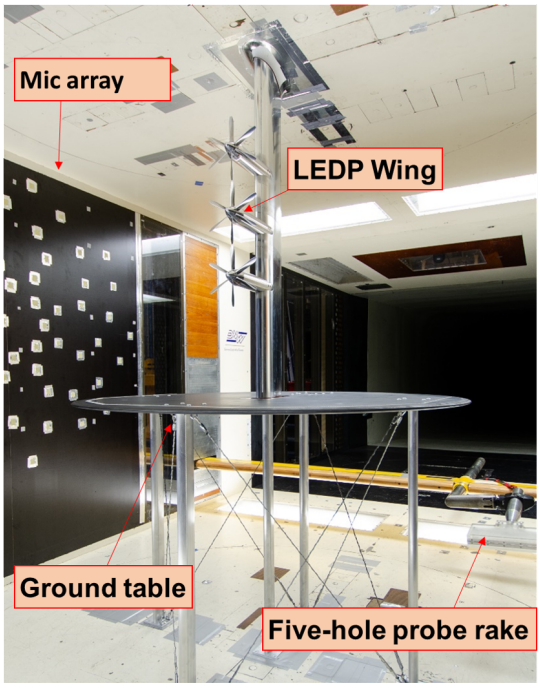

Figure 3.7: Wind-tunnel assembly.

model. The span of the fairing is 35 mm. Figure (3.8) shows a wind tunnel run of the Flap 30 deg x=0%c y=2%c configuration using tufts to evaluate possible 3D effects near the wing-ceiling junction at two different AoA. For AoA = 5 deg (Fig. (3.8a)), cross-flow is observed at the model-ceiling junction despite of the fairing that leads to a small area of detached flow, while there is no cross-flow coming from the gap at the tip section. Nevertheless, the 3D effects are highly evident at AoA = 14 deg (Fig. (3.8b)) at the model-ceiling junction while cross-flow can be appreciated coming from the tip gap, but with less severity than in the model-ceiling junction. Analyzing the latter, it can be seen how the cross-flow covers a large portion of the span generating detached flow and merging with the cross-flow generated by the nacelle-wing interference. This interference is analyzed in Chapter (5). In conclusion, at high AoA the wing could not be considered as 2D and the values of wing aerodynamic coefficients obtained are no longer representative for the whole wing. Nevertheless, a comparison could still be made between different configurations.

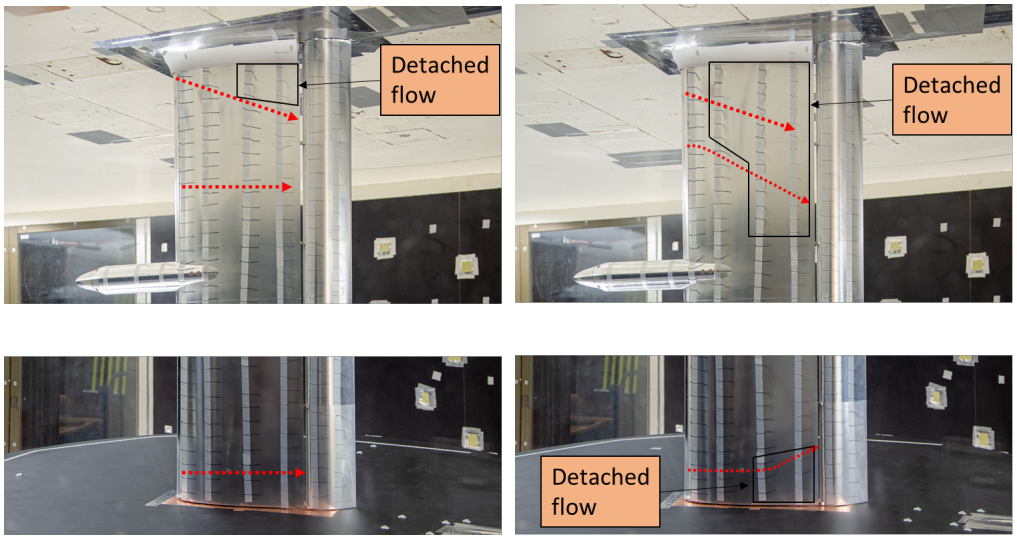

(a) AoA = 5 deg.

(b) AoA = 14 deg.

Figure 3.8: Wind-on run using tufts of the Flap 30 deg x=0%c y=2%c configuration.

Transition strips are placed in both main element and flap in upper and lower surface. The strips are made of carborandum with a grain size of 0.5 mm that has been estimated using equation (3.1) [50]. The parameters used are based on sea-level conditions and the chord of the model. Since the grain size calculated using the chord of the flap is also close to 0.5 mm (0.43 mm), the same grain size is used for simplicity.

$$k = \frac{x}{Re_x^{3/4}} \sqrt{\frac{Re_k}{0.332}} \tag{3.1}$$

The position of the transition strips is selected based on two criteria. First, it is desired to place the transition strips as close as possible to the leading-edge to ensure that transition takes place before separation even at high AoA. Second, avoiding cover or being too close to any of the pressure taps. Following these criteria, the position of the transition strips is shown in the following table:

	Upper surface	**Lower surface**
Main element	5 %c	10 %c
Flap	5 %c_f	5 %c_f

Table 3.3: Position of the transition strips.

3.4. MEASUREMENT TECHNIQUES

The different measurement techniques that are used in the experiment are explained in this section. The techniques are explained together with the data processing approach and its uncertainty.

BALANCE

The model is attached to a six-component balance to measure the forces and moments present during the operation. The lift and drag coefficients are therefore obtained by non-dimensionalizing lift and drag forces. For doing so, the wind-tunnel dynamic pressure (V_∞) and the wing area of the model (S_{ref})

$$C_L = \frac{L}{q_\infty S_{\text{ref}}} \tag{3.2}$$

$$C_D = \frac{D}{q_\infty S_{\text{ref}}} \tag{3.3}$$

To subtract the forces and moments generated by non-aerodynamics sources, a wind-off measurement is performed. This measurement is not only conducted for all the AoA range, but also taking into account hysteresis. To do so, the wind-off measurement is made by differentiating when the AoA is increasing and when the AoA is decreasing. A linear fit for each of the two cases is made and subtracted for all the balance data. A different wind-off measurement is performed with the flap deployed to evaluate if significant difference between the two measurement takes place for two reasons: the change in mass distribution due to the deployment of the flap and the possibility of uncertainty between measurements performed in different days. Small differences were appreciated between wind-off measurements.

The uncertainty of the balance is 0.1% of the full measurement range. The measurement range is presented in table (3.4). These calibration error values are treated as a systematic error present on all the balance measurements. To account for the random error, two approaches are evaluated based on a repeated measurement:

- For the two measurements, the 2 deg angle of attack is tested three times per configuration. This leads to six measurements of the same condition in total from which standard deviation is obtained and applied to all AoA.
- For each AoA, the standard deviation is calculated using the repeated measurements. At the end, there are AoA with only two measurements to obtain the standard deviation and AoA with more measurement.

The standard deviation obtained from both methods is similar, the first approach is therefore used for simplicity.

Balance magnitude	**Range**
F_x	2100 N
F_y	2100 N
F_z	8400 N
M_x	1700 Nm
M_y	1700 Nm
M_z	2100 Nm

Table 3.4: Balance measurement range.

PRESSURE TAPS

Wing surface pressure is recorded using pressure taps. Two rows of pressure taps are placed in chordwise direction. The rows are placed at $0.7R_p$ from the medium propeller centerline, one in inboard direction and the other in outboard direction (Figure (3.9)). This position where the maximum slipstream axial velocity is expected [51]. Each row has pressure taps in upper and lower surface of both main element and flap, the spacing between pressure taps is made using a cosine distribution. The specific location of the pressure taps can be found in Appendix (C). The pressure data is used to calculate the pressure coefficient:

$$C_p = \frac{p - p_\infty}{q_\infty} \tag{3.4}$$

To obtain the sectional lift (C_l) and pressure drag coefficient (C_{d_p}), the wing is divided into panels, the pressure coefficient is interpolated to the panel midpoint. Since no pressure

tap can be placed on the trailing-edge, the pressure coefficient at that position is obtained from linear extrapolation. The pressure coefficient are projected into the vertical and the horizontal component. An integration is performed to obtain the sectional aerodynamic coefficients. Two coefficients are used: sectional lift coefficient, C_l and sectional pressure drag, C_{d_p}.

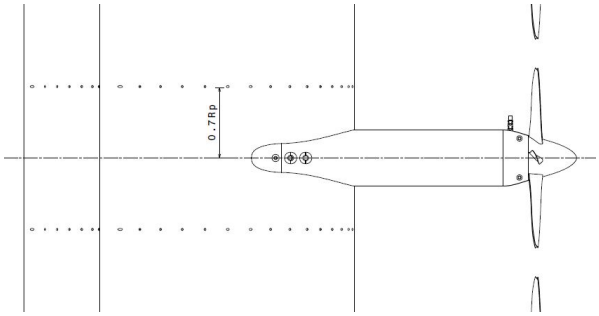

Figure 3.9: Top view of the pressure taps position.

The uncertainty of the pressure sensor was 0.25% of the measurement range, which is 5 psi for the pressure taps where high suction/pressure is expected (close to the leading-edge of both elements); and 1 psi for the rest of the pressure taps. The same approach as described for the balance data is used to account for the random error. The standard deviation for each pressure port is obtained using the repeated measurements. For the sectional aerodynamic coefficients, the errors present in the pressure taps measurement are considered random when propagating the spread in pressure coefficient through integration to obtain the sectional aerodynamic coefficients. The error was obtained by analyzing the standard deviation of the sectional aerodynamic coefficients from the repeated measurement. It was found that when propagating the error, the latter becomes negligible, it is therefore not included when showing sectional aerodynamic coefficients data.

FIVE-HOLE PROBE MEASUREMENTS

A five-hole probe is located aft of the model to analyze the wake plane. The rake is placed at 345 mm from the main element trailing edge (1 chord from the flap retracted configuration trailing-edge) aligned with the middle propeller. The origin of the wake survey plane is located at half-span (625 mm) from the wall (Fig. (3.10)). It consists of 18 five-hole probes with spherical heads (2.5 mm diameter). A sketch of the wake analysis with the position of the measurement plane is provided in figure (3.10). Data of the three components of the velocity and pressure data is obtained to identify the areas of increased axial velocity and the rotational flow generated by the slipstream. Total pressure is also calculated using the total pressure coefficient:

$$C_{p_t} = \frac{p_t - p_\infty}{q_\infty} \tag{3.5}$$

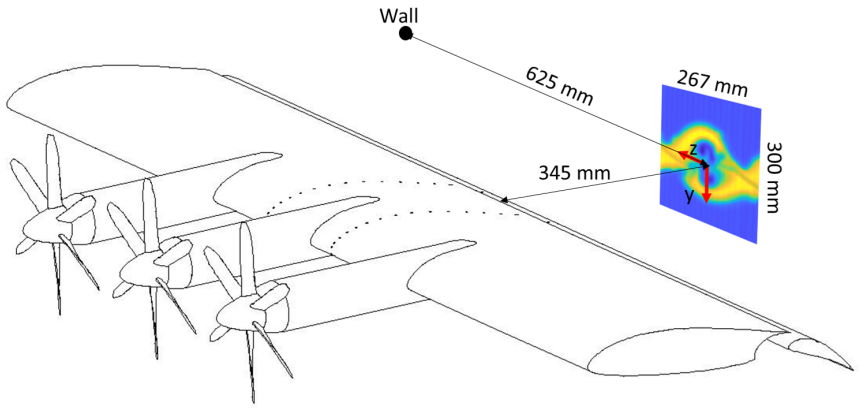

Figure 3.10: Sketch of the location of the wake survey plane

3.5. OPERATING CONDITIONS

In this section, the operating conditions in which the experiment takes place are collected. Not only the data concerning velocity, AoA or propeller advance ratio; but also the different configurations that are tested and the differences between them.

Table (3.5) collects the operating conditions of the experiment. A freestream velocity of 30 m/s is selected as the wind tunnel velocity for the experiment. A velocity of 40 m/s was also evaluated but discarded due to the strong vibrations generated at high angles of attack. This value of the velocity leads to a Reynolds number based on the chord of approximately 610000. This Reynolds number is significantly lower than the Reynolds number of a full-scale model [52] that may have an effect, not only on the lift and drag coefficients, but also on the stall behavior, being the effect of the enhanced Reynolds number on the slipstream more significant for the stall behavior and the wing-flap interaction than in full-scale applications. In conclusion, this experiment presents a limit case of a wing with small propellers and high aspect ratio which is relevant for small aircraft such as UAM

Parameter	**Test values**
Angle of attack α	-4°, -1°, 2°, 5°, 8°, 10°, 11°, 12°, 13°, 14°, 15°, 16°
Freestream velocity V_∞	30 m/s
Reynolds number Re	610k

Table 3.5: Table collecting the operating conditions.

or RAM STOL concepts. This experiment, therefore, serves as a demonstrator for future experiments with larger models.

The range of angles of attack varies from -4° to 16° when the flap is retracted and to 14° when the flap is deployed. Three thrust settings are tested simulating three thrust conditions (Table (3.6)). Except where otherwise noted, all propeller-on configurations use medium-thrust setting ($J = 1$) as this is the closest setting to the maximum propeller efficiency condition.

Thrust	**Rotational velocity** ω	**Advance ratio** $J = \frac{V_\infty}{\omega D_p}$	**Thrust coefficient** $T_c = \frac{T}{q_\infty \pi R_p^2}$
Low thrust	128.4 Hz	$J = 1.15$	$T_c \approx 0.25$
Medium thrust	147.6 Hz	$J = 1$	$T_c \approx 0.5$
High thrust	184.5 Hz	$J = 0.8$	$T_c \approx 1$

Table 3.6: Table collecting the thrust settings.

In Section (3.1), the flap positions chosen for the experiment were presented. Nevertheless, due to the lack of time and several issues during the test campaign, only 5 flap positions were tested apart from the retracted conditions. One of the flap positions selected is the one corresponding to take-off configuration (15 deg, x=8%c, y=2%c). As stated in Section (2.4), the effect of the overlap is lower than the effect of the gap, that is the reason why two different gap positions are selected for the two flap deflections, 30 deg and 40 deg. The flap positions are shown in table (3.7). These five flap positions together with the flap retracted condition were the configurations selected for the experiment. To evaluate if the small gap present in flap retracted configuration is significant in the aerodynamic coefficients, the flap retracted with the gap closed using tape was also tested.

For the configurations explained in the previous paragraph, different settings are tested. Due to the lack of time, not all the combinations could be tested. Apart from the three models explained in Section (3.3), when the propellers are turned on, there are three

	Retracted	**Retracted (gap closed)**	**FP1 15 deg x=8%c y=2%c**	**FP2 30 deg x=0%c y=3%c**	**FP3 40 deg x=0%c y=3%c**	**FP4 40 deg x=0%c y=5%c**	**FP9 30 deg x=0%c y=2%c**
Clean	X	X	X				X
Prop-off	X	X	X	X	X	X	X
1 Prop		X					
Prop-on (1 *J*)				X	X	X	
Prop-on (3 *J*)	X	X	X				X
Wake array		X	X				X

Table 3.7: Configurations tested during the wind-tunnel campaign.

different situations: first, testing only with the middle propeller 81 Prop), second, testing with all the propellers but only for the medium-thrust setting (Prop-on 1J) and, finally, testing with all the propellers for the three thrust settings (Prop-on 3J). Apart from that, the five-hole probe measurement is only performed in few configurations. The different combinations of configuration and setting are collected in table (3.7).

The data presented in the following chapters is raw data. No wind tunnel corrections have been applied to the data because, when estimating wind tunnel corrections due to blockage and streamline curvature, it was found that they may have a slight impact on the lift coefficient only at high AoA while they may have a slight impact on the zero-lift drag coefficient of the entire AoA range, but since the focus of the research is on lift enhancement, they are neglected as well. The calculations regarding wind tunnel corrections can be found on Appendix (D).

4

AERODYNAMIC INTERACTION BETWEEN THE DISTRIBUTED-PROPULSION SLIPSTREAM AND THE FLAP RETRACTED WING

In this chapter, the results of the wind-tunnel experiment concerning flap retracted configuration are analyzed to gain further insight into slipstream-wing interaction in distributed propulsion systems. The chapter is divided in three sections. First, the results of the aerodynamic coefficients when the propeller is turned off are presented as a baseline. Two baseline configurations are shown: the wing with nacelle and the wing without nacelle (clean wing). Second, a comparison is made between the aerodynamic coefficients of the propeller-off case and the configuration with only the middle propeller on to assess the effect of a single propeller. Third, the effect of having multiple propellers in close proximity (distributed propulsion) in the aerodynamic coefficients is compared with the effect of having a single propeller. Likewise, the third section is divided into three subsections: the effect of distributed-propulsion on the aerodynamic coefficients, the influence of thrust setting and the wake analysis.

The configurations presented in this chapter correspond to the case where the flap gap in retracted configuration is open. Configurations with the gap closed have been also tested. Only small differences are appreciated at high-angles of attack because some flow

passes through the gap that creates a two-airfoil interference. The presence of the rear element slightly increases the suction peak on the upstream element, enhancing the lift coefficient.

The same approach is made throughout the chapter. First, the balance data is presented in terms of wing lift coefficient and wing drag coefficient. To obtain a better understanding of the local flow phenomena, sectional data of the aerodynamic coefficients is also provided. When further explanation is required, pressure distributions are shown.

4.1. AERODYNAMIC COEFFICIENTS OF THE BASELINE CONFIGURATION

In this section, the aerodynamic coefficients that comprises the baseline are presented. The wing lift and drag coefficients are shown in figure (4.1) and the sectional lift and the sectional pressure drag are shown in figure (4.2). Two configurations are provided: the wing with nacelles and the clean wing.

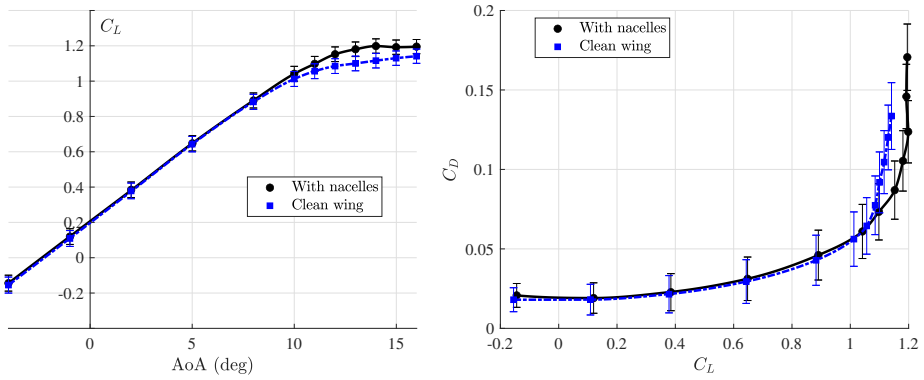

(a) C_L vs. AoA

(b) C_L vs. C_D

Figure 4.1: Wing aerodynamic coefficients. Flap retracted with nacelles vs. clean wing

Figure (4.1a) shows how the lift coefficient is similar with and without nacelles until high-angles of attack are reached, where the configuration with nacelle provides additional lift. Due to the proximity of the pressure taps section to the nacelle, the sectional lift coefficient presents higher difference than the wing lift coefficient, as shown in figure (4.2a). At high-angles of attack, the pressure distribution (4.3b) reveals how the clean wing configuration is stalled while the configuration with nacelles has attached flow. Additionally, the nacelle generates lift that contributes to the difference in wing lift coefficient at high AoA.

The reason for the difference in lift between the nacelle configuration and the clean wing configuration could lie in the interaction between the nacelle and the wing. In a

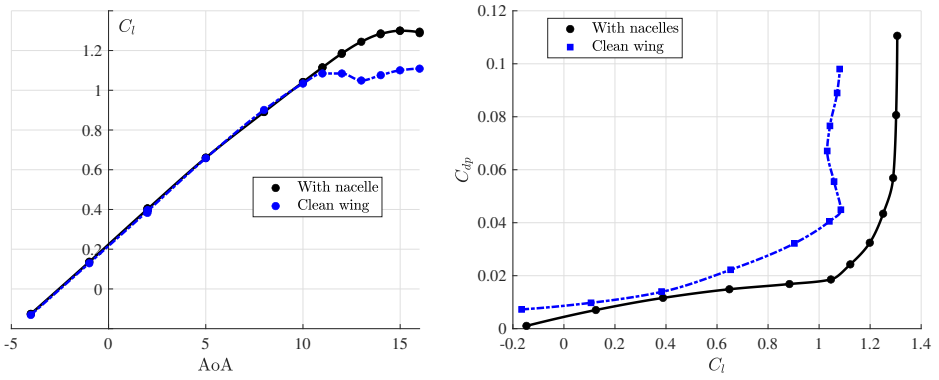

(a) Sectional lift coefficient

(b) Pressure drag coefficient.

Figure 4.2: Sectional aerodynamic coefficients. Flap retracted with nacelles vs. clean wing

nacelle-wing interference, an area of high pressure is produced downstream of the nacelle. This creates a pressure difference between the adjacent spanwise position where there is no nacelle and the downstream of the nacelle [53], generating cross-flow towards the area of less pressure. The adjacent nacelle follows the same behavior, increasing the area of influence of the cross-flow that enhances the suction postponing separation at the pressure taps location.

The presence of the nacelle does not produce a significant change in wing drag coefficient at low-angles of attack, as shown in figure (4.1b). Nevertheless, a decrease in sectional pressure drag can be observed with respect to the clean wing configuration in figure (4.2b). The pressure distribution at low-angle of attack (5 deg) (4.3a) shows how in the configuration with nacelle there is a shift of the suction peak to a more upstream position. It is difficult to ascertain the reason for the change in pressure distribution, the culprit may be a local increase in AoA. When following the circular shape around the nacelle, the flow increases its vertical component leading to an increased AoA [53] that shifts the suction peak to a more upstream position, hence reducing the pressure drag. Although this phenomenon would explain the change in pressure distribution, the increase in angle of attack takes place in a region close to the nacelle, so it is unlikely to have a significant influence at the pressure taps location.

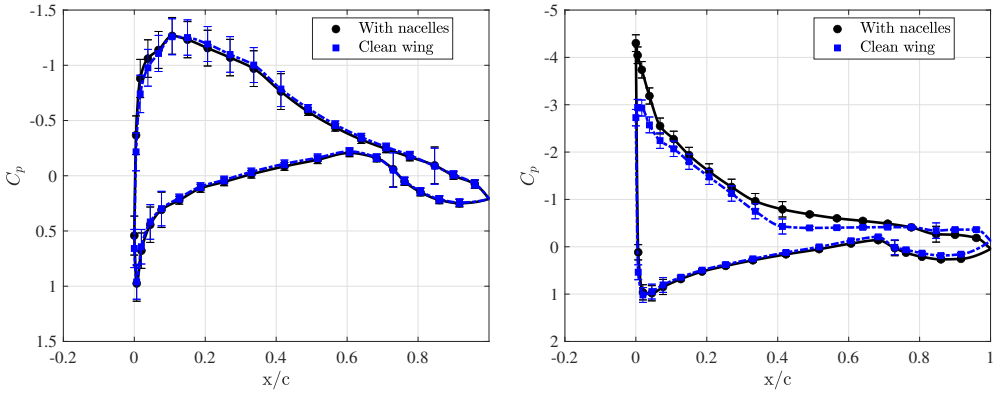

(a) AoA = 5 deg.

(b) AoA = 14 deg.

Figure 4.3: Pressure distribution. Flap retracted with nacelles vs. clean wing

4.2. LIFT ENHANCEMENT DUE TO ONE PROPELLER

As explained in chapter (2), the propeller slipstream enhances the lift on the wing mainly due to the increase in dynamic pressure. Apart from this net effect on the lift, the local lift is increased or decreased depending on whether is up-going or down-going blade, respectively, because of the propeller swirl. The enhancement in wing lift coefficient and in sectional lift coefficient in relation to the propeller-off case (with nacelles) can be appreciated in figures (4.4a) and (4.4b), respectively.

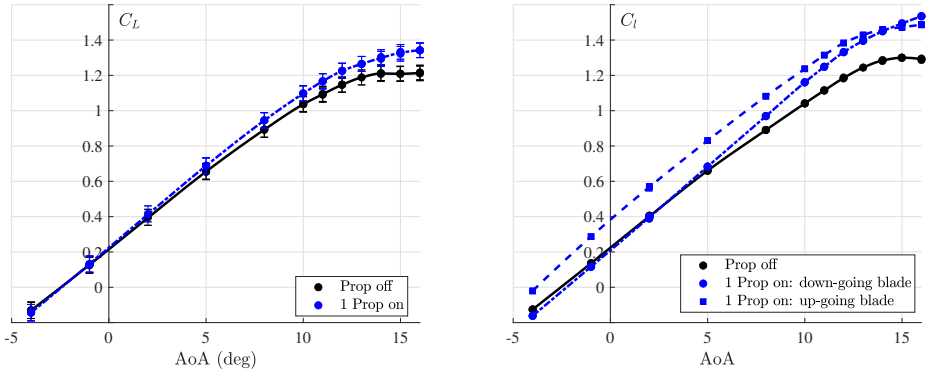

(a) C_L vs. AoA.

(b) C_l vs. AoA as obtained from pressure distribution.

Figure 4.4: Lift coefficient enhancement due to one propeller.

As can be seen in figure (4.4a), apart from the increase in lift curve slope, the maximum lift coefficient is increased. This delay in stall is due to the contribution of the following factors:

- The Reynolds number is higher due to the increased velocity in the slipstream.
- The propeller normal force that contributes to the lift as the wing increases the AoA.
- The decrease in effective AoA because the increase in axial velocity takes place parallel to the propeller axis and the latter is horizontally inclined negatively with respect to the wing position.

To get an impression of how much the increase in Reynolds number or the contribution of the propeller forces affects the lift coefficient, the increase in axial velocity produced by the propeller as well as the contribution of the propeller force to the lift enhancement are calculated. To obtain the increase in axial velocity, momentum theory as presented in Chapter (2) is used. The increase in velocity is assumed to be the velocity induced by the propeller. The induced velocity (v_i) is obtained solving equation (4.1). The velocity downstream of the propeller ($V_\infty + v_i$) for the three thrust settings is collected in table (4.1).

$$T = 2\rho_\infty A_p v_i (V_\infty + v_i) \tag{4.1}$$

Thrust	J	$V_\infty + v_i$	Increase in Reynolds number
Low thrust	1.15	33.37 m/s	11%
Medium thrust	1	36.21 m/s	21%
High thrust	0.8	40.97 m/s	37%

Table 4.1: Table collecting the increase in velocity downstream of the propeller according to momentum theory.

Next, the impact of the Reynolds number on the lift coefficient is analyzed. For this purpose, an aerodynamic analysis is performed using XFOIL of the airfoil for the two farthest cases, i.e., the propeller-off case and the high-thrust case (J = 0.8), and for two AoA, 5 and 16 deg. The results are collected in table (4.2). It can be seen that a difference of approximately 2.5% is obtained between the two configurations for both AoA. In conclusion, the change in Reynolds number due to the increase in axial velocity in the slipstream does not have a significant effect on the lift coefficient.

Thrust	Re	C_L at AoA = 5 deg from XFOIL	C_L at AoA = 16 deg from XFOIL
Prop-off	610000	0.79	1.33
High thrust	836000	0.81	1.35

Table 4.2: Table collecting the lift coefficient as obtained from XFOIL for two Reynolds number and AoA.

To obtained the contribution of the propeller forces to the lift, the thrust is normalized with the dynamic pressure and the wing area and it is multiplied by $\sin\alpha + i_p$, as shown in equation (4.2). Being i_p the propeller incidence angle (-5 deg). Figure (4.5) shows the evolution of $C_{L_{\text{Thrust}}}$ with AoA for the three thrust settings.

$$C_{L_{\text{Thrust}}} = \frac{T_c A_p}{S_{\text{ref}}} \sin(\alpha + i_p) \tag{4.2}$$

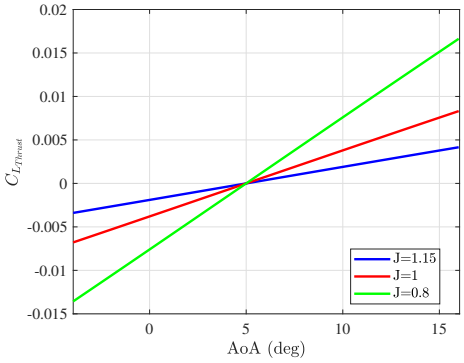

Figure 4.5: Contribution of the thrust to the lift coefficient as a function of AoA for three thrust settings.

The maximum lift coefficient obtained for the single-prop case as extracted from Fig. (4.4a) is 1.34. The contribution of the thrust to the lift coefficient for that condition (J = 1) at AoA = 16 deg is 0.008. This means that the force generated by the propeller contributes 0.6% to the lift coefficient of the wing, so it can be concluded that the vertical force generated by the propeller is not a major contribution to the lift. The case in which there are three propellers (distributed propulsion) is analyzed in section (4.3.2), where the contribution of the vertical force generated by the three propellers is shown for the high-thrust case.

Figure (4.4b) shows the difference between up-going and down-going blade side in terms of sectional lift coefficient when compared to the propeller-off case (with nacelles). One one hand, the up-going blade side provides higher sectional lift coefficient at low angles of attack due to the combined effect of the increased dynamic pressure and the increased effective angle of attack provided by the swirl. This effect can be appreciated in figure (4.6a), the pressure coefficient peak increases due to the added velocities in the leading edge. On the other hand, the down-going blade side does not increase the sectional lift coefficient because the increase in dynamic pressure is counteract by the decrease in effective angle of attack provided by the downwards flow direction of the slipstream swirl. The decrease in effective angle attack can be appreciated in the pressure distribution (Fig. (4.6b)), the pressure peak is similar but the location of the peak takes place at a more aft position.

Nevertheless, at high-angles of attack, the trend is inverted. In the up-going blade side the flow is prior to stall, the increase in sectional lift is therefore due to the increase in dynamic pressure (figure (4.7a)); in the down-going blade side, the flow is still attached due to the lower effective angle of attack (figure (4.7b)) that, combined with the increase in dynamic pressure, provides higher sectional lift than the up-going blade side. It is

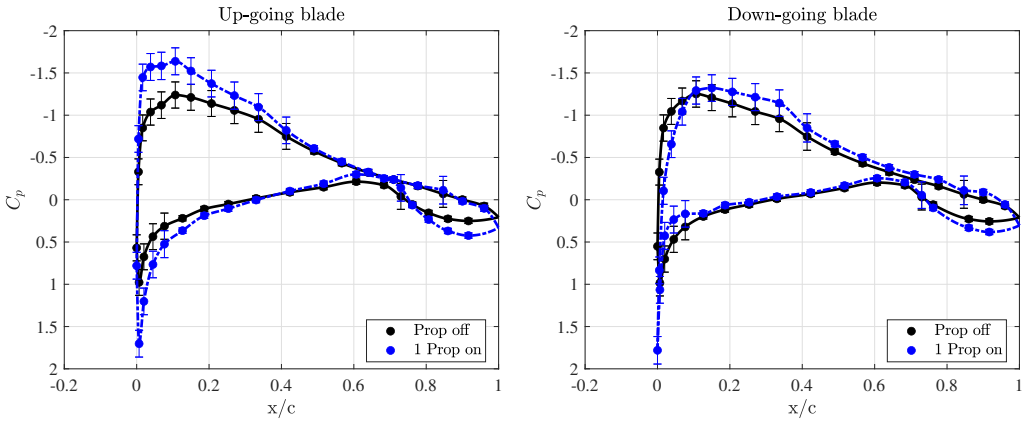

(a) Up-going blade side.

(b) Down-going blade side.

Figure 4.6: Pressure distribution at AoA = 5 deg. Flap retracted prop off vs. 1 Prop.

worth noting the difference in the prop-off configuration between up- and down-going blade side due to the appearance of 3D effects, showing the loss of the two-dimensionality at high angles of attack, as mentioned in chapter (3).

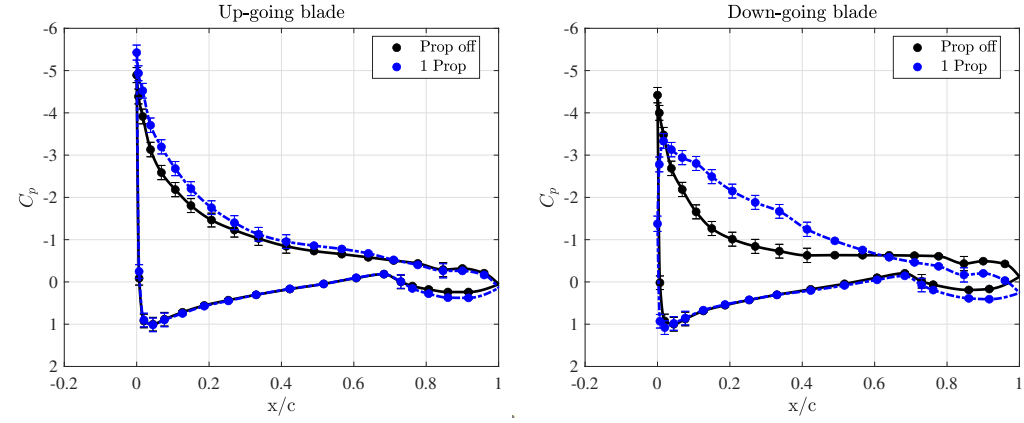

(a) Up-going blade side.

(b) Down-going blade side.

Figure 4.7: Pressure distribution at AoA = 16 deg. Flap retracted prop off vs. 1 Prop.

Another effect that must be taken into account when evaluating the difference between up-going and down-going blade sides is the asymmetry in the propeller loading that occurs due to the difference in pressure induced by the difference in effective angle of attack. This results in an increase in blade loading on the down-going blade side that may contribute to the change in the lift enhancement trend experienced. This difference in blade loading is more pronounced as the angle of attack increases because the pressure difference between the up- and down-going blade side is greater.

4.3. LIFT ENHANCEMENT DUE TO DISTRIBUTED PROPULSION

In this section, the lift enhancement produced by the three propellers in distributed-propulsion configuration is analyzed and compared to the case of three times a single propeller to assess the effect of having adjacent propellers on the aerodynamic coefficients, the pressure distribution and the slipstream shape. This section is divided in three subsections. First, the comparison between distributed propulsion and three times a single propeller is evaluated in terms of wing and sectional aerodynamic coefficients, supported by the pressure distribution. In the second subsection, the effect of the thrust setting on those aerodynamic coefficients is assessed. Finally, the deformation of the slipstream in distributed propulsion configuration is studied using wake array data.

4.3.1. EFFECT OF ADJACENT PROPELLERS ON THE AERODYNAMIC COEFFICIENTS

Despite having multiple adjacent propellers provides and interference between their slipstreams, this interaction seems to have a negligible effect on the wing aerodynamic coefficients. To elaborate this statement, the lift coefficient enhancement produced by a single propeller is obtained, multiplied by three and added to the lift coefficient produced by the prop-off configuration. The resulting lift coefficient (3 x 1 Prop) is compared to the lift coefficient of the distributed-propulsion configuration. Figure (4.8) shows how similar lift coefficient and drag coefficient are obtained when comparing distributed-propulsion and three times a single propeller, there is no significant advantage of the distributed-propulsion configuration. Only a different behavior is observed at high angles of attack. Sectional data is analyzed below to evaluate the local flow differences.

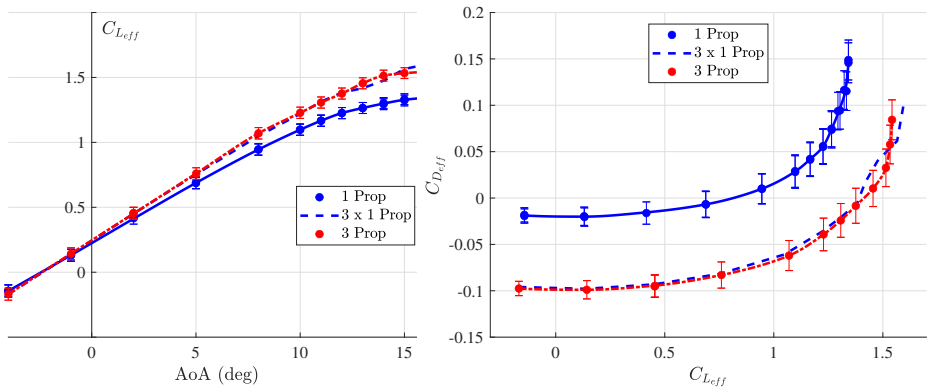

(a) $C_{L_{eff}}$ vs. AoA.

(b) $C_{L_{eff}}$ vs. $C_{D_{eff}}$

Figure 4.8: Sectional lift coefficient. Flap retracted 1 Prop vs. 3 prop.

Figure (4.9) shows the sectional lift coefficient enhancement in both sides for the two configurations, single-propeller (1 Prop) and distributed-propulsion (3 Prop). The effect

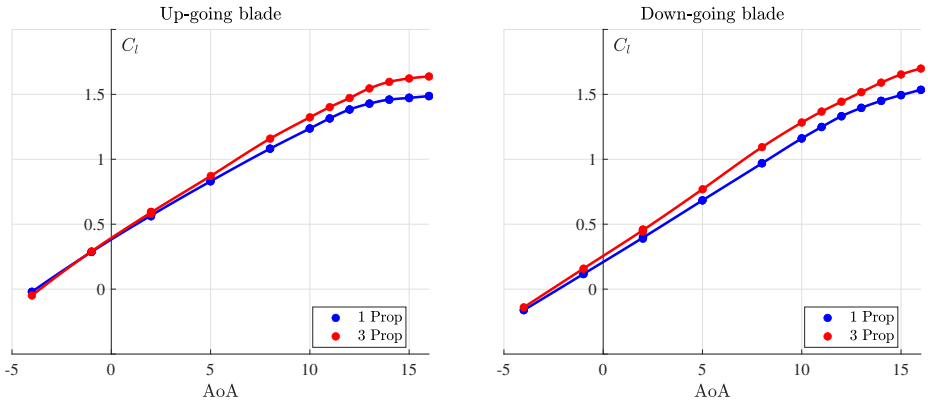

(a) Up-going blade side.

(b) Down-going blade side.

Figure 4.9: Sectional lift coefficient. Flap retracted 1 Prop vs. 3 prop.

of the adjacent propellers is to increase the lift curve slope for the up-going and the down-going blade side. The difference between single-propeller and distributed propulsion is more noticeable at high-angles of attack.

The increase in lift produced by the distributed-propulsion configuration versus the single-propeller configuration is due to the distribution of lift across the wingspan. As shown in chapter (2), in addition to the increase in lift in the area encompassed by the propeller, outside this area there is no pressure jump between the lift distribution of the wing and that produced by the propeller, but there is a region where the lift recovers to that of the wing in propeller-off conditions. This is a result of the vorticity sheet that leaves the wing.

In the distributed propulsion configuration, outside the spanwise area covered by the propeller, there are other spanwise intervals covered by the other propellers. Within this spanwise area covered by the propeller, in addition to the increase in lift produced by the slipstream itself, there is also the increase in lift produced by the adjacent slipstream outside its covered area. A simple sketch showing this effect is provided in figure (4.10). This explains the higher lift enhancement in the down-going blade side when comparing distributed-propulsion and single-propeller because the adjacent propeller is in its up-going blade side, hence, producing higher lift. It must be noticed that, if a propeller locally generates less lift compared to the propeller-off wing due to the swirl throughout the entire down-going blade side, the adjacent propeller would be adversely affected in terms of lift enhancement.

Analyzing the pressure distribution at AoA = 5 deg (Fig.(4.11)), an increase in rear loading of the pressure side is observed. This increase is higher in the down-going blade side and it may be caused by the slipstream shear that takes place on the adjacent propeller that impinges the middle propeller. This phenomenon is further explained in section (4.3.3),

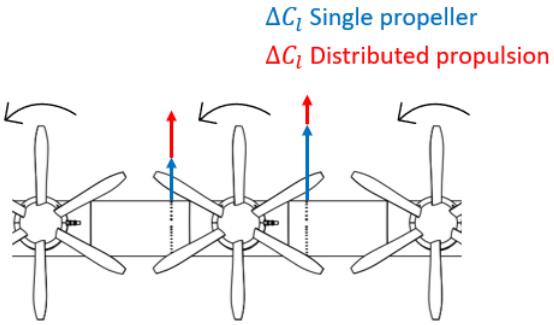

Figure 4.10: Sketch representing the lift enhancement of a distributed-propulsion system when compared to a single-propeller.

where the wake analysis of the slipstream is performed.

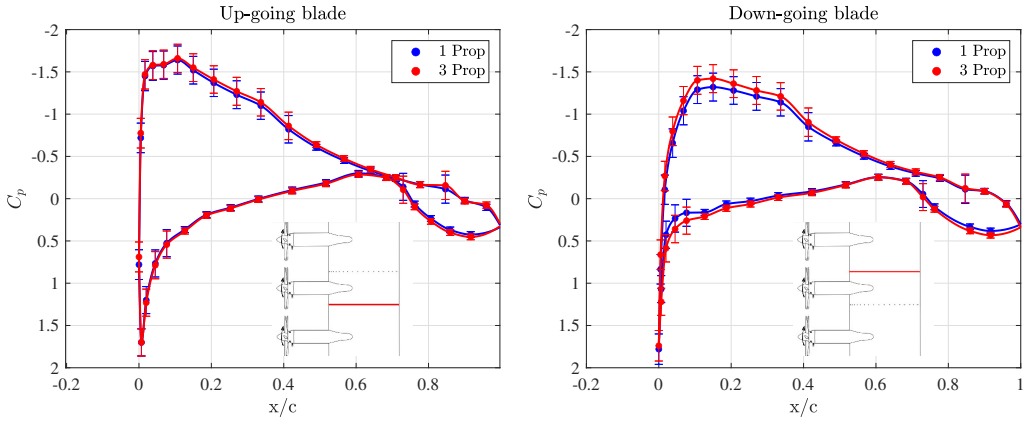

(a) Up-going blade side.

(b) Down-going blade side.

Figure 4.11: Pressure distribution at AoA = 5 deg. Flap retracted 1 Prop vs. 3 prop.

Figure (4.12) shows the sectional pressure drag enhancement on both sides for both configurations. High rise in pressure drag occurs for the single-propeller configuration compared to the distributed-propulsion one at high-angles of attack. On the up-going blade side, at low-angles of attack, there is a shift in the pressure distribution to a more aft position (Fig.(4.11a)) motivated by the pressure distribution of the adjacent propeller due to its lower effective angle of attack. On the down-going blade side, the increase in suction peak due to the influence of the adjacent propeller explained in the previous paragraph decreases the pressure drag.

At high-angles of attack, in the up-going blade side, the increase in effective angle of attack of the single-propeller configuration leads to separation in the upper surface while in the distributed-propulsion configuration a small bump can be appreciated at $x/c = 0.4$

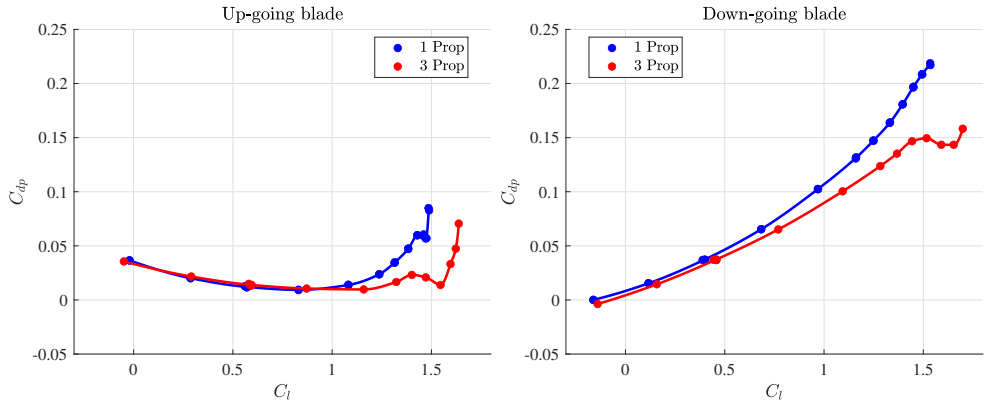

(a) Up-going blade side.

(b) Down-going blade side.

Figure 4.12: Sectional pressure drag coefficient. Flap retracted 1 Prop vs. 3 prop.

(Fig. (4.13a)) that could be a laminar bubble induced by the adjacent propeller as it is also present in the down-going blade side (Fig. (4.13b)). The pressure distribution at a specific section is generated by the propeller comprising that section and the influence of the pressure distribution generated by the adjacent propeller. This bubble postpones stall, leading to the higher differences in sectional lift coefficient at high-angles of attack between distributed-propulsion and single-propeller in the up-going blade side. On the contrary, on the down-going blade side, higher suction peak is obtained in the distributed-propulsion configuration influenced by the adjacent propeller enhanced suction peak.

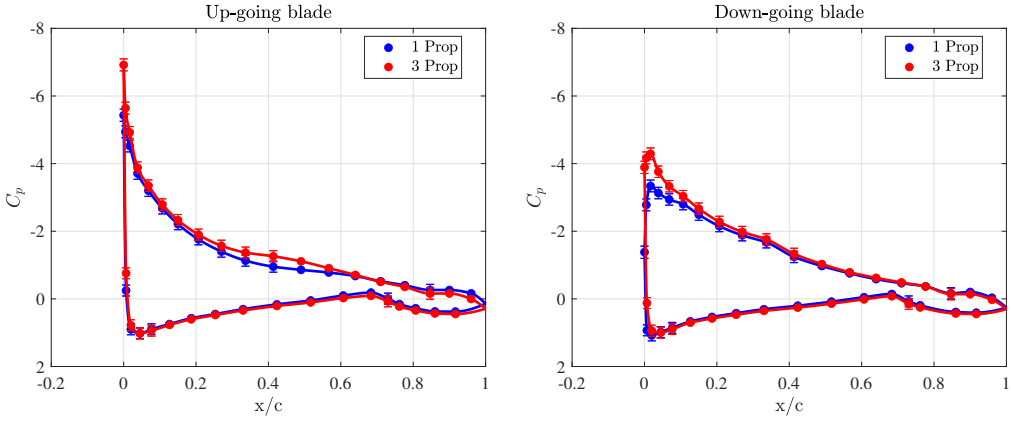

(a) Up-going blade side.

(b) Down-going blade side.

Figure 4.13: Pressure distribution at AoA = 16 deg. Flap retracted 1 Prop vs. 3 prop.

4.3.2. THRUST SETTING EFFECTS

Increasing thrust has two effects on lift enhancement. On the one hand, an increase in thrust implies an increase in axial velocity, which leads to an increase in dynamic pressure. On the other hand, increased or decreased thrust provides a change in propeller efficiency. A decrease in efficiency leads to an increase in swirl, which would magnify the local AoA effects. Figure (4.14) shows the wing lift coefficient enhancement as a function of the advance ratio for two different angles of attack, 5 deg and 16 deg. The lift coefficient enhancement is presented in a relative form respect to its propeller-off case.

$$\frac{\Delta C_{L_{\text{eff}}}}{C_L^{\text{prop-off}}} = \frac{C_{L_{\text{eff}}}^{\text{prop-on}} - C_L^{\text{prop-off}}}{C_L^{\text{prop-off}}} \tag{4.3}$$

It must be noted that the propeller-on lift coefficient is referred to as $C_{L_{\text{eff}}}$ because it includes the vertical components of the propeller forces due to its contribution to the lift. This contribution is collected in table for AoA = 16 deg, since in the 5 deg case the propeller is aligned with the freestream velocity. The magnitude presented in table (4.3) is the contribution of the thrust force to the lift enhancement. It can be seen how the contribution is 10% for the highest thrust setting, being an important part of the lift enhancement.

	AoA	Low thrust (J = 1.15)	Medium thrust (J = 1)	High thrust (J = 0.8)
$\frac{C_{L_{Thrust}}}{\Delta C_{L_{\text{eff}}}}$	16 deg	4%	8%	10%

Table 4.3: Contribution of the propeller thrust to the lift enhancement at AoA = 16 deg for three thrust settings.

In general trends, the increase in wing lift coefficient is higher for low advance ratios (high thrust). The evolution of wing lift coefficient enhancement when comparing distributed-propulsion (3 Prop) and three times the single-propeller (3 x 1 Prop) is similar for AoA = 5 deg. On the contrary, when analyzing the wing lift coefficient enhancement at AoA = 16 deg, the evolution with advance ratio is similar at low advance ratios (high thrust) but it less affected at high advance ratios (low thrust). Sectional data is presented below to obtain more information about these behaviors.

Figure (4.15) shows the sectional lift enhancement and the sectional pressure drag enhancement for two angles of attack (AoA = 5 and 16 deg) and both sides. In low-lift condition (AoA = 5 deg), the effect of the advance ratio is more appreciable in the up-going blade side due to increased swirl with decreased advance ratio. Analyzing the pressure distribution at AoA = 5 deg (Fig.(4.16)), the shift in the pressure distribution of the suction side to a more aft position as a consequence of the decreased effective angle of attack induced by the adjacent propeller is magnified as the thrust increases. This shift in the pressure distribution is responsible for the large differences in sectional pressure drag enhancement

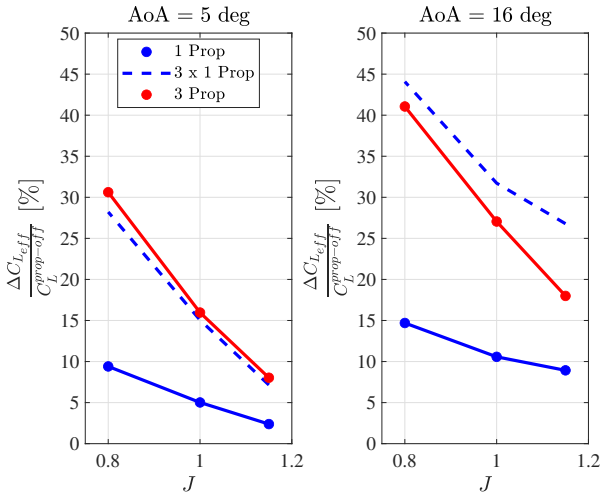

Figure 4.14: Wing lift coefficient enhancement vs. J

obtained with increased advance ratio (Fig. (4.15b)). The rotational direction of the adjacent propeller again plays an important role since there is a significant difference between single-propeller and distributed-propulsion in the down-going blade side, where the increase in suction peak with increased thrust is also magnified due to the increased swirl in the adjacent propeller.

The effect of the slipstream shear in the adjacent propeller mentioned in the previous subsection is also visible in the pressure distributions (Fig. (4.16)) when looking at the rear loading. Two conclusions are extracted:

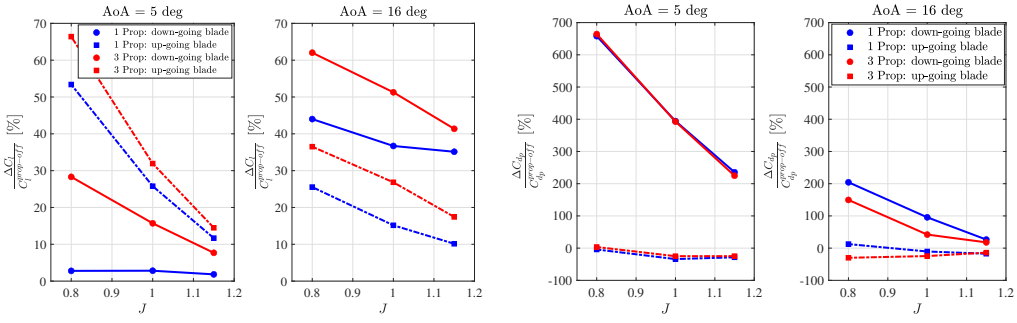

(a) Sectional lift coefficient enhancement.

(b) Sectional pressure drag coefficient enhancement.

Figure 4.15: Effect of the thrust setting on the sectional aerodynamic coefficients. Flap retracted 1 Prop vs. 3 Prop.

- The increase in rear loading in the pressure side is more significant when increasing the thrust. This increase in thrust intensifies the shear experienced by the slipstream due to the increased swirl that displaces each of the halves in the opposite direction with greater intensity, which causes it to influence the adjacent propeller more by increasing the dynamic pressure at the lower surface. This effect is further discussed in the following section, where the slipstream deformation is assessed in terms of wake survey data.

- The effect is more visible on the down-going blade because, while in the up-going blade side it is its own slipstream the one that increases the rear loading on the pressure side, in the down-going blade side is the bottom-half from the adjacent propeller the one that increases the pressure with its impingement.

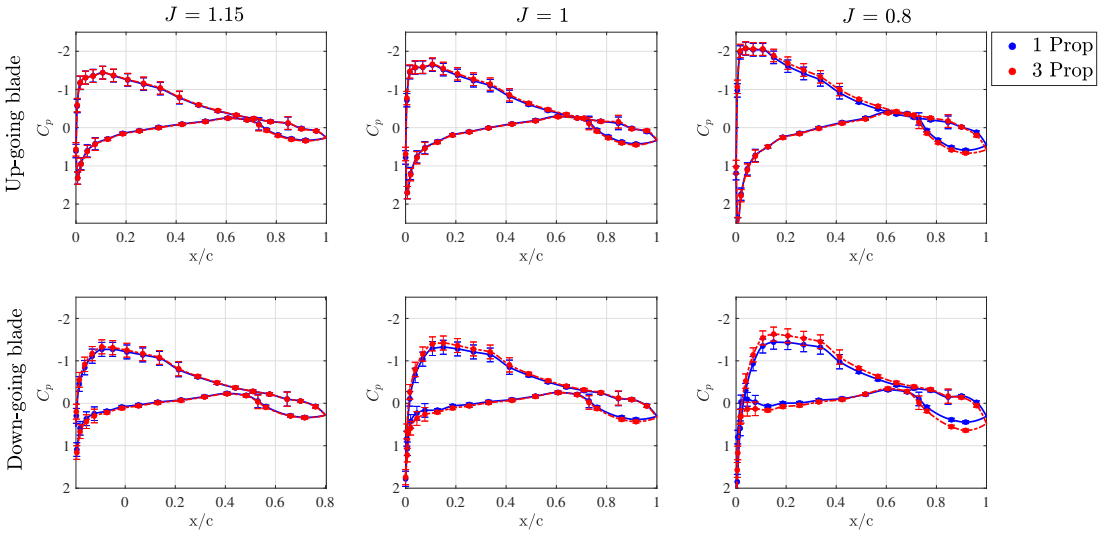

Figure 4.16: Pressure distribution at AoA = 5 deg for different thrust settings. 1 propeller on vs. 3 propeller on.

In high-lift conditions (AoA = 16 deg, Fig. (4.15a)), a similar evolution of the sectional lift enhancement with advance ratio at low advance ratios (high thrust setting) can be seen for the single-propeller and distributed-propulsion configurations, although an offset persists between them as a consequence of the induced lift enhancement from the adjacent propeller, which now provides higher values of sectional lift enhancement in the down-going blade side due to the change in trend between up- and down-going blade side at high-angles of attack explained in section (4.2). Nevertheless, at high advance ratios, the evolution of sectional lift enhancement with advance ratios of both single-propeller and distributed-propulsion configurations follows a different behavior, reducing the differences between them. The sectional pressure drag follows the same pattern explained previously for the sectional lift enhancement. The behavior seems to be, therefore, produced by flow separation. Analyzing the pressure distribution (Fig.(4.17)),

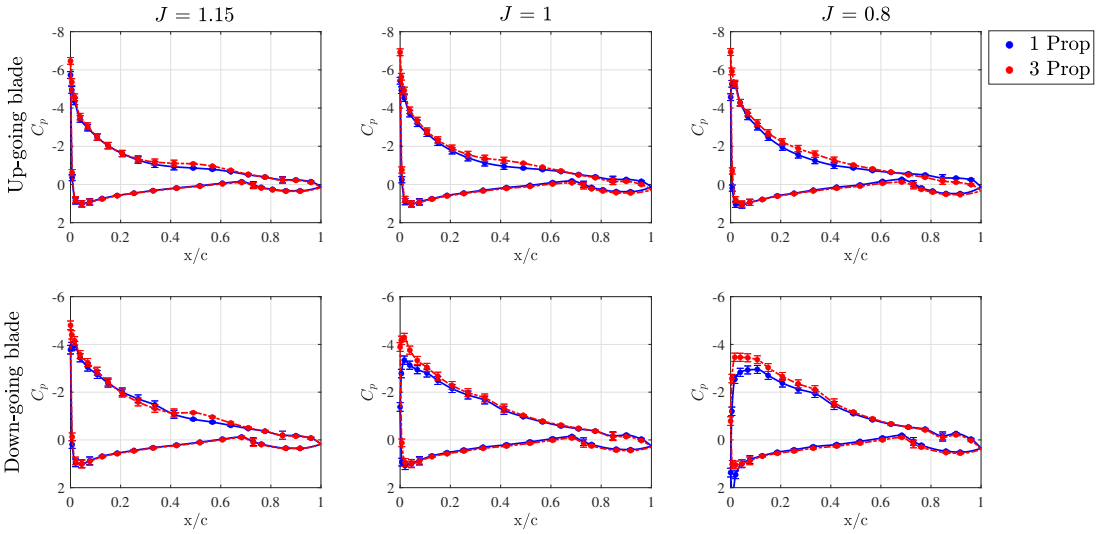

Figure 4.17: Pressure distribution at AoA = 16 deg for different thrust settings. 1 propeller on vs. 3 propeller on.

a similar trend as the AoA = 5 deg pressure distributions regarding the suction peak is observed. Nevertheless, the enhance in rear loading in the pressure side is not visible possibly due to the high inclination of the propeller with respect to the freestream flow compared to the previous AoA that was aligned with the propeller. The increase in AoA deforms the slipstream shape flattening the lower halve [21].

In all the pressure distributions at AoA = 16 deg, (Fig.(4.17)), a small bump can be recognized at different positions (between $x/c = 0.2$ and $x/c = 0.6$) in both up- and down-going blade sides. This bump could be a laminar bubble generated by the adjacent propeller. Nevertheless, another explanation lies in the complexity of the flow at high-angles of attack under slipstream interaction and the wing-nacelle interaction that may cause cross-flow that makes a 2D sectional analysis difficult to interpret. Focusing on the up-going blade side, when comparing $J = 1.15$ and $J = 1$, similar pressure distribution is obtained except for the slight increase in pressure peak. However, when comparing $J = 1$ and $J = 0.8$, it can be seen how the first one has trailing-edge stall while the latter has a pressure distribution prior to stall that may be generated by the increase in Reynolds number with increased axial velocity. On the down-going blade side, higher pressure peak is observed as a consequence of the adjacent up-going propeller that is magnified with increased thrust (decreased advance ratio).

4.3.3. WAKE ANALYSIS

To obtain more knowledge on the interaction between propeller slipstreams in a distributed -propulsion wing, results of the wake analysis of the propeller-off (Fig. (4.18)) configuration and the distributed-propulsion configuration (Fig. (4.19)) are presented. In both figures, the axial velocity ratio and total pressure coefficient distribution are shown together with the velocity distribution.

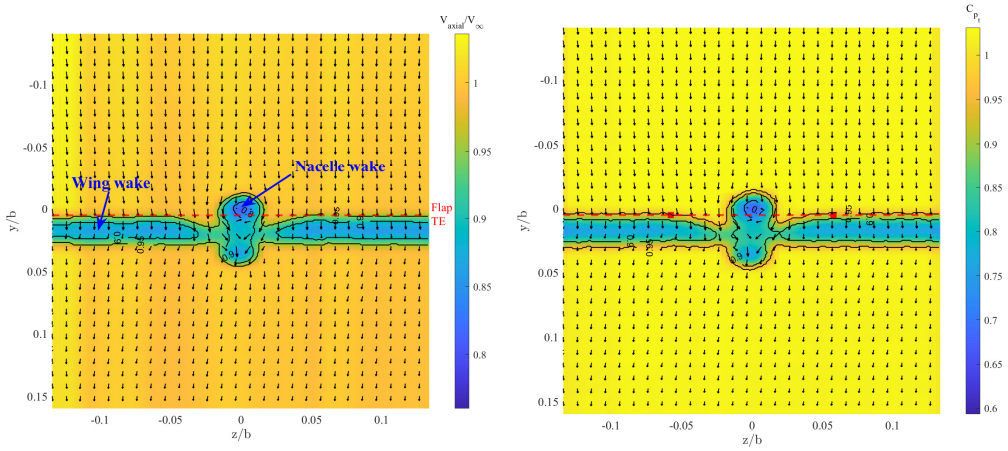

(a) Axial velocity ratio.

(b) Total pressure coefficient.

Figure 4.18: Wake measurement results of Flap Retracted configuration in prop-off case at AoA = 2 deg. View in upstream direction.

First, wake measurement results are shown in figure (4.18) for the flap retracted configuration at AoA = 2 in propeller-off condition seen from behind the wake plane (looking in upstream direction). Both representations (axial velocity ratio and total pressure coefficient) are almost identical. Two different areas of decreased total pressure (and decreased axial velocity) are identified that belong to the wing wake and the nacelle wake. The velocity distribution shows the perturbation of the nacelle on the flow. The curvature of the flow close to the nacelle can also be seen in Fig. (4.19a), which may be the cause of the increase in effective angle of attack mentioned in section (4.1).

Figure (4.19) shows the wake array results for the distributed-propulsion condition (J = 1). Again, the distribution of axial velocity ratio and total pressure coefficient are very similar. The slipstream deformation due to the presence of the wing is well known from previous research ([21], [54]), as shown in Fig. (2.6). However, those experiments were conducted using isolated propeller. The flow at both sides of the middle propeller is merged with the adjacent propellers creating an area of increased axial velocity in the region between propellers. It can be seen how each slipstream half is displaced producing impingement on the adjacent propeller area. This merged area in-between propellers generates a continuous lift enhancement distribution along the wing. Figure (4.20) shows

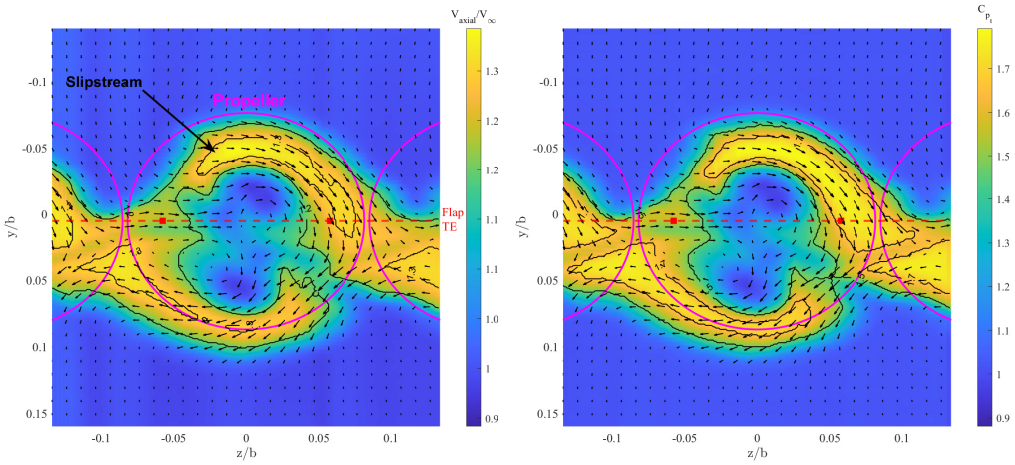

(a) Axial velocity ratio.

(b) Total pressure coefficient.

Figure 4.19: Wake measurement results of Flap Retracted configuration in Distributed-propulsion ($J = 1$) case at AoA = 2 deg. View in upstream direction.

a conceptual sketch of the slipstream deformation and how it increases with increased thrust, as explained in the previous section.

Although not easily distinguishable, one can see an area where the total pressure coefficient is not as large in the region between propellers. This is the wing wake which is deformed due to the rotation imposed by the swirl of the propeller.

The red squares plotted on Fig. (4.19b) represent the location of the pressure taps sections. Although the deformation of the slipstream is unknown, it can be seen how in the down-going blade side (right square), the impingement of the adjacent propeller's

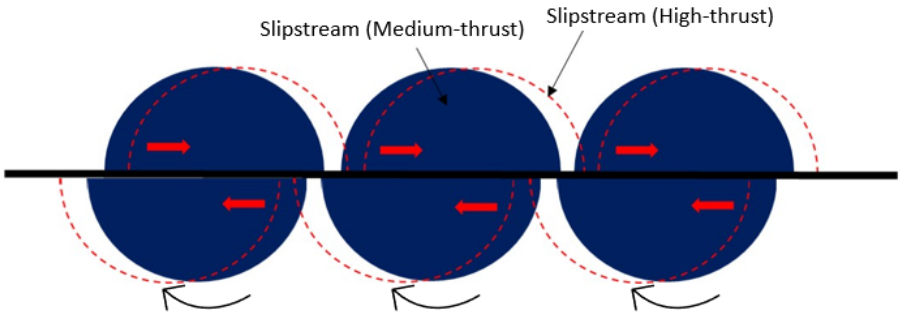

Figure 4.20: Drawing showing the increase in slipstream shear with thrust. Propellers rotate clockwise.

slipstream is present on the lower side and is responsible of the enhance in rear loading of the distributed-propulsion configuration when compared to the single-propeller one commented in previous sections.

5

EFFECT OF FLAP POSITION OEN THE PROPELLER-WING-FLAP INTERACTION IN DISTRIBUTED PROPULSION SYSTEMS

In this chapter, the results of the wind-tunnel experiment concerning the flap deployed configuration are presented with the objective of studying the effect of the flap position on the aerodynamic interaction with the propeller slipstream in distributed-propulsion configuration. First, the results of the aerodynamic coefficients for the wing without the effect of the propeller slipstream are provided to show how the flap position affects the aerodynamic coefficients in propeller-off conditions and which role the nacelle plays by comparing the results with the clean wing configuration. Second, the effect that the flap deflection under propeller slipstream has on the lift enhancement is assessed when the propellers are on. This section is divided into three subsections: the effect of flap deflection on the aerodynamic coefficients, the influence of the thrust setting and the slipstream deformation when the flap is deployed. The last section evaluates the influence of the flap gap under slipstream effects on the lift enhancement is assessed.

5.1. PROPELLER-OFF CONDITIONS

The aerodynamic coefficients for the different flap position configurations are presented in this section. Although the effect of the flap deflection angle and the flap gap on the

aerodynamic coefficients has been researched before for the selected airfoil [45], since the Reynolds number is different and plays an important role in the high-lift aerodynamics and the whole setup is different, the effect of the flap position is addressed in propeller-off conditions and serves as the baseline to subsequently analyze the lift enhancement in propeller slipstream conditions.

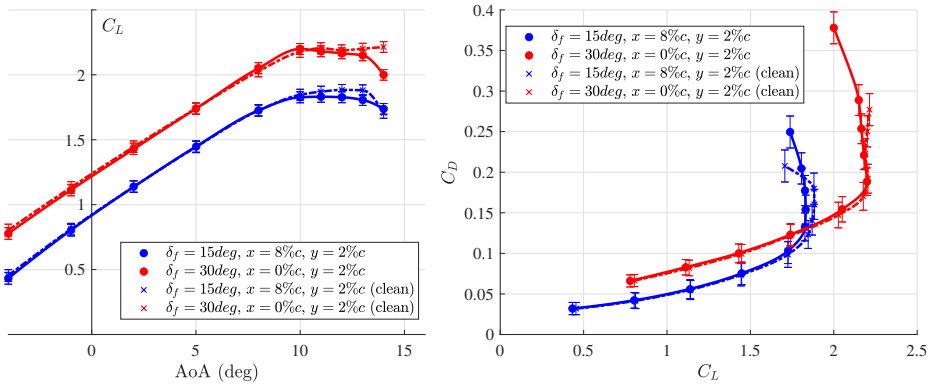

(a) C_L vs. AoA.

(b) C_L vs. C_D.

Figure 5.1: Wing aerodynamic coefficients. Flap $\delta_f = 15deg$, $x = 8\%c$, $y = 2\%c$ vs. Flap $\delta_f = 30deg$, $x = 0\%c$, $y = 2\%c$ and with nacelle vs. clean wing.

The effect of the flap deflection on the wing lift and drag coefficient is presented in figure (5.1). The increase in lift coefficient and the decrease in AoA for maximum lift coefficient with flap deflection is appreciated in figure (5.1a) and the increase in drag coefficient with flap deflection is shown in figure (5.1b). Apart from the effect of the flap deflection angle, the difference between the configuration with nacelles and the clean wing configuration is presented in figure (5.1). Contrary to the effect of the nacelle when the flap is retracted, when the flap is deflected the nacelle has a detrimental effect on the lift coefficient.

In chapter (4), the cross-flow generated as a consequence of the pressure gradient between the area downstream of the nacelle and the adjacent area where there is no nacelle is explained. The increase in suction in the area where the nacelle is not placed due to the flap deflection, increases the cross-flow that, in this case, seems to have a detrimental effect due to the reduction in suction, as it can be observed in the pressure distribution in Fig. (5.2).

Figure (5.3) shows a wind-on tunnel run in Flap 30 deg configuration using tufts for two AoA. It can be seen how at AoA = 5 deg (Fig. (5.3a)), the presence of the nacelle generates cross-flow from downstream of the nacelle, where the pressure is higher, to the area outside the nacelle influence, where there is more suction, as commented in section (4.1). Nevertheless, at AoA = 13 deg (Fig. (5.3b)) the nacelle generates re-circulation far from its downstream area covering the pressure taps section location. The reason could be the increase in suction in the area where the nacelle is not placed due to the flap deflection.

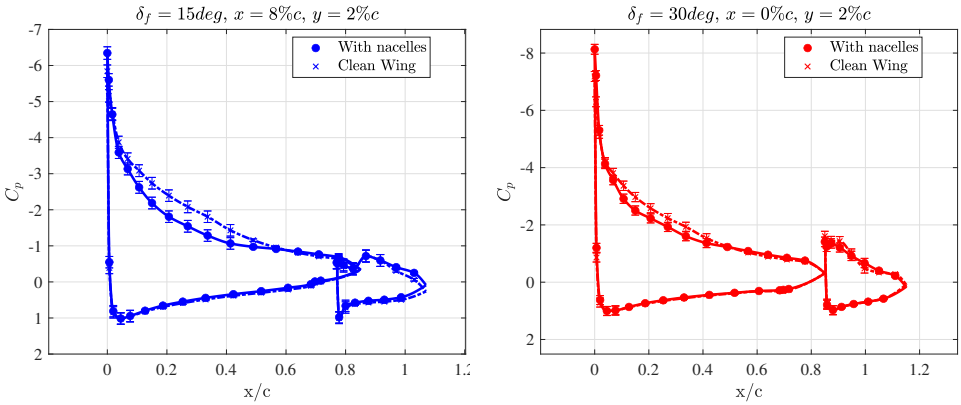

(a) Flap $\delta_f = 15deg,\ x = 8\%c,\ y = 2\%c$

(b) Flap $\delta_f = 30deg,\ x = 0\%c,\ y = 2\%c$

Figure 5.2: Pressure distribution at AoA = 13 deg. With nacelles vs. Clean Wing.

The increase in suction leads to an increase in the cross-flow that, in this case, seems to have a detrimental effect, as it can be observed in the pressure distribution in Fig. (5.2), where there is a reduction in suction of the configuration with nacelles. It must be noticed how the flow downstream of the middle nacelle is also detached that may be caused due to the combined cross-flow from the adjacent nacelles.

The effect of the flap slot on the wing lift and drag is presented in figure (5.4) for two flap deflections. For the 30 deg flap deflection, higher lift coefficient and lower drag coefficient is obtained for smaller flap slot. Figure (5.5) shows the flap pressure distribution of all the different flap slot configurations. The increase in lift and decrease in drag are explained because in the configuration with $y = 3\%c$ flap gap the stalled region is bigger. An erratic behaviour where the lift coeficient decreases and increases successively is appreciated for the $y = 3\%c$ flap slot case from an AoA of 10 degrees due to separation on the flap trailing edge, probably due to a thicker fresh boundary layer that is more prone to separation when compared to the $y = 2\%c$.

For the 40 deg flap deflection, again, higher values of the lift coefficient and lower of the drag coefficient are obtained when decreasing the flap slot (5.4). The $y = 5\%c$ flap slot provides lower lift than the rest of configurations due to separation of the whole flap section (5.5) because of the increased distance with the main element that eliminates the mutual interference. On the other side, the $y = 3\%c$ flap slot presents a high suction peak at low angles of attack. The flap is stalled for both slots at high angles of attack as a consequence of the strong pressure gradient created by the high inclination combined with the low Reynolds number at which the experiment is tested.

Due to its stalled behavior throughout most of the AoA range, the 40 deg configuration is not analyzed as it does not represent an interesting flight condition since the flow separation is so present.

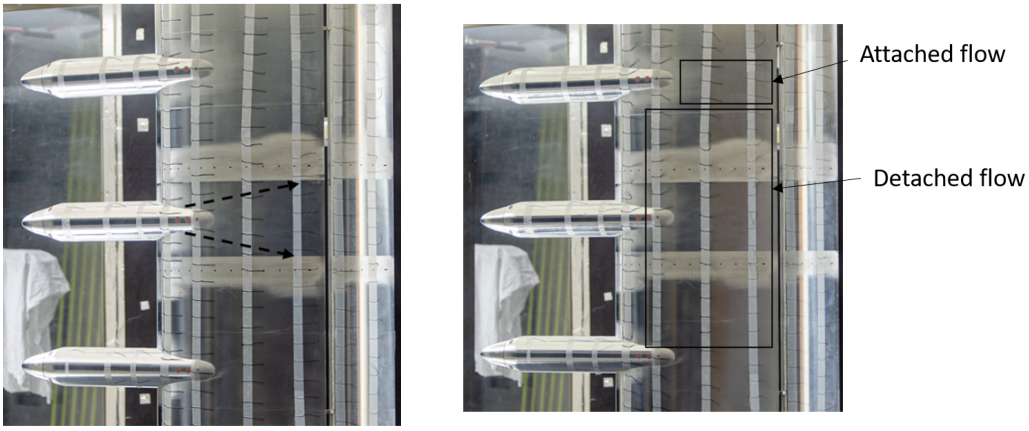

(a) AoA = 5 deg.

(b) AoA = 13 deg.

Figure 5.3: Wind-tunnel model picture using tufts. Flap $\delta_f = 30deg$, $x = 0\%c$, $y = 2\%c$.

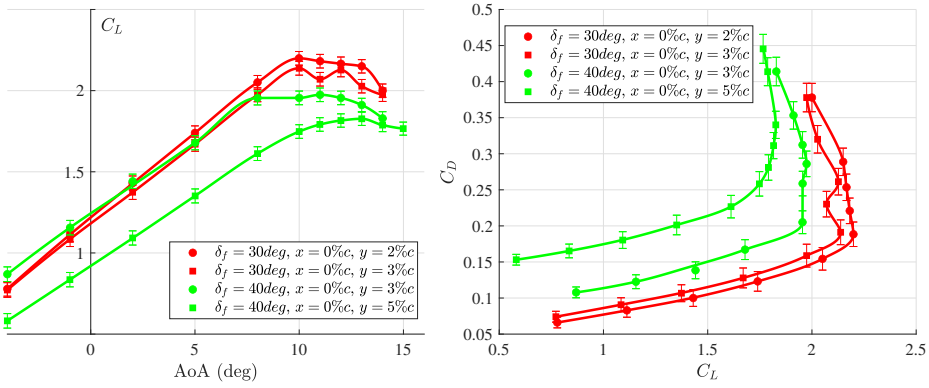

(a) Wing lift coefficient vs AoA.

(b) Wing drag coefficient vs AoA.

Figure 5.4: Wing aerodynamic coefficients. Flap $\delta_f = 30deg$, $x = 0\%c$, $y = 2\%c$ vs. $3\%c$ and Flap $\delta_f = 40deg$, $x = 0\%c$, $y = 3\%c$ vs. $5\%c$

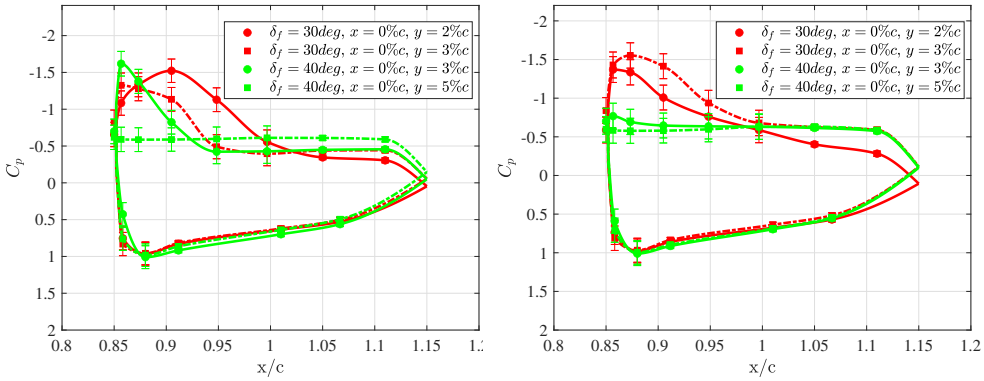

(a) AoA = 5 deg.

(b) AoA = 13 deg.

Figure 5.5: Flap pressure distribution Flap δ_f = 30deg, x = 0%c, y = 2%c vs. 3%c and Flap $\delta_f = 40deg$, $x = 0\%c$, $y = 3\%c$ vs. $5\%c$

5

5.2. INFLUENCE OF THE FLAP DEFLECTION ANGLE ON THE LIFT ENHANCEMENT IN PROPELLER-ON CONDITIONS

The effect of the flap deflection on the lift enhancement is assessed in this section for a wing with distributed propulsion. As stated at the beginning of the chapter, the section is divided in three subsections. The first section focuses on the lift enhancement under slipstream effects. The second section evaluates the influence of the thrust setting on the lift enhancement. Finally, wake measurement data is provided to analyze the influence of the flap position on the slipstream deformation. Three configurations are analyzed: flap retracted, flap δ_f = 15 deg, $x = 8\%c$, $y = 2\%c$ and flap δ_f = 30 deg, $x = 0\%c$, $y = 2\%c$.

5.2.1. EFFECT OF FLAP DEFLECTION ANGLE ON THE WING LOADS

In order to understand the effect of the flap deflection angle on the wing lift enhancement in the distributed-propulsion configuration, the wing lift coefficient enhancement for the three configurations is shown in figure (5.6). At first glance, a completely different behavior of the lift enhancement with AoA is observed between the three configurations. The flap retracted configuration follows an increasing trend with AoA although it presents a small bucket around AoA = 10 deg. The 15 deg flap deflection configuration follows an slightly increasing behavior with the same bucket at the same location, after that, it experiences a significant rise. Finally, in the 30 deg flap deflection configuration, the lift enhancement is the highest at low AoA but it decreases with it, the bucket is magnified and increases after. For further analysis, sectional data is presented below (Fig.(5.7)) to understand phenomena underlying the lift enhancement. The three magnitudes represented are sectional lift enhancement (Eq. (5.1)), sectional flap lift enhancement

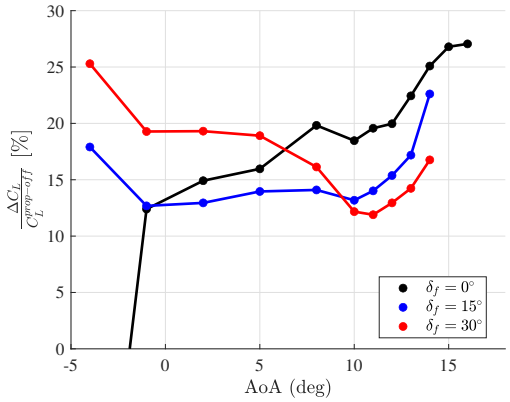

Figure 5.6: Effect of the flap deflection on the wing lift enhancement ($J = 1$) due to propeller slipstream vs. AoA.

5

(normalized with wing chord, Eq. (5.2)) and pressure drag enhancement (Eq. (5.3)). The enhancement in sectional aerodynamic coefficients is supported by representations of the pressure distribution of both flap deflections at three different AoA: 5 deg, 10 deg and 14 deg.

$$\frac{\Delta C_l}{C_l^{\text{prop-off}}} = \frac{C_l^{\text{prop-on}} - C_l^{\text{prop-off}}}{C_l^{\text{prop-off}}} \tag{5.1}$$

$$\frac{\Delta C_{l_\text{f}}}{C_{l_\text{f}}^{\text{prop-off}}} = \frac{C_{l_\text{f}}^{\text{prop-on}} - C_{l_\text{f}}^{\text{prop-off}}}{C_{l_\text{f}}^{\text{prop-off}}} \tag{5.2}$$

$$\frac{\Delta C_{d_p}}{C_{d_p}^{\text{prop-off}}} = \frac{C_{d_p}^{\text{prop-on}} - C_{d_p}^{\text{prop-off}}}{C_{d_p}^{\text{prop-off}}} \tag{5.3}$$

In figure (5.7) it can be seen how on the down-going blade side, at low-AoA the sectional lift enhancement is more prominent for the highest flap deflection. The sectional flap lift coefficient enhancement reveals an increase in the flap contribution to the lift that is clearly visible as an increase in flap suction peak when analyzing the pressure distribution at AoA = 5 deg (Fig (5.9)). An increase of flap suction peak is also appreciated in the up-going blade at the same AoA, although the increment is of lower magnitude. The reason for this difference between sides may come from the increase in axial velocity produced by the lower half of the slipstream of the adjacent propeller impingement as it is displaced due to shear. It must be noticed that the increase in suction peak of the main element, that takes place in the up-going blade side as a consequence of increased effective angle of attack, decreases the suction on the flap to a certain extent due to the circulation effect explained in chapter (2). Since both effects act in opposite direction,

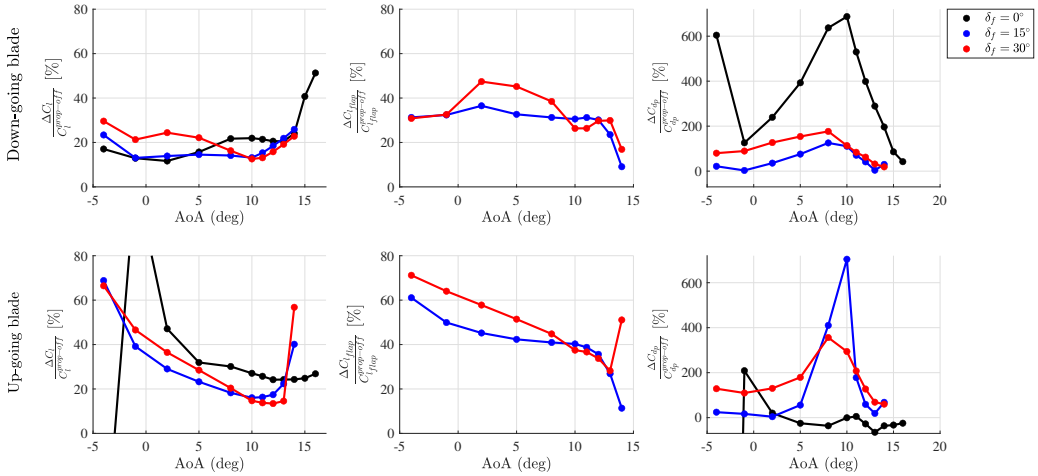

Figure 5.7: Effect of the flap deflection on the sectional aerodynamics enhancement ($J = 1$) due to propeller slipstream vs. AoA.

it is difficult to evaluate the real explanation for the difference in flap lift enhancement between both sides. This increase in flap participation is responsible for the higher sectional pressure drag of the 30 deg flap deflection when compared to the 15 deg one.

Another relevant aspect that can be observed in the pressure distributions at AoA = 5 deg (Figs. (5.8) and (5.9)), is the increase in suction with respect to the propeller-off configuration in the rear part of the main element. Although no conclusion can be drawn from the presented data regarding this effect, this increase may be due to the dumping effect present as a consequence of the pressure decrease in the flap, which would allow the main element to have less pressure without impairing the pressure gradient and causing flow separation.

The increase in flap suction is less apparent with increased AoA because the propeller is inclined with respect to the freestream velocity which translates into a different evolution of the slipstream compared to the AoA = 5 deg case where they are aligned. This means that the slipstream of the adjacent propeller may generate lower impingement, reducing the increase in axial velocity.

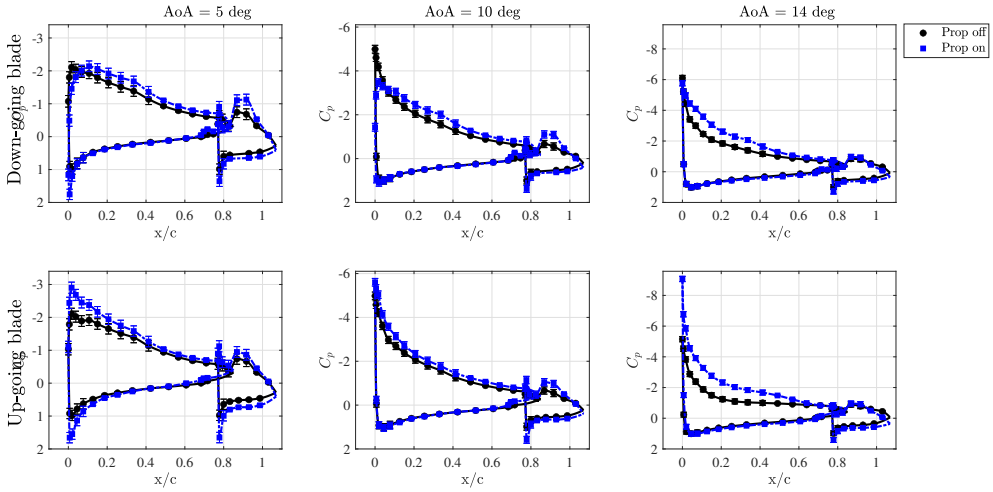

Figure 5.8: Pressure distribution of the Flap 15 deg configuration at three different AoA. Propeller-on vs. Propeller-off

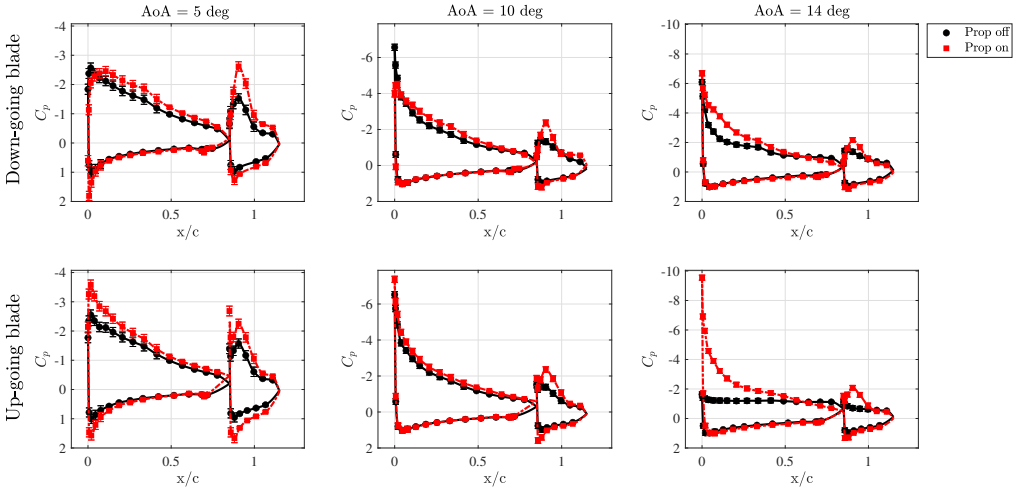

Figure 5.9: Pressure distribution of the Flap 30 deg configuration at three different AoA. Propeller-on vs. Propeller-off

At medium-to-high AoA (between 8 and 12 deg), the propeller seems to decrease its effect on the lift enhancement. This could be originated due to the combination of AoA and propeller inclination with respect to the wing, that hinders the slipstream to create a "doughnut" effect on the wing. Its effect is more accused in the up-going blade side due to the increased effective AoA. The effect of flap deflection on the lift enhancement is not visible in this area as both configuration present similar flap enhancement and lower compared to the flap retracted case. Nevertheless, a sudden increase in the sectional pressure drag is generated as a consequence of the the reduced influence on the main element, being the flap the only element with an increased suction that is responsible for the increase in pressure drag.

At high-AoA, stall is present in propeller-off conditions while the increased Reynolds number created by the increased axial velocity in the slipstream keeps the flow attached and, therefore, provides a high rise in lift enhancement.

5.2.2. EFFECT OF THRUST SETTING

As in chapter 4, the effect that the thrust change has on the lift enhancement is presented for two flap deflections. In a way, varying the thrust is a way to verify the phenomena explained in the previous section due to its dependence on the change in axial velocity and/or swirl. Figure (5.10) shows the lift enhancement for two advance ratios (J=0.8 and J=1.15) different to the one in Fig. (5.6). At first glance, similar behavior with AoA is obtained independent on the thrust setting, although the lift enhancement is almost scaled with increasing thrust. Figures (5.11) and (5.12) show the pressure distribution at three AoA for the three different advance ratio tested of the 15 deg and 30 deg flap deflection configuration, respectively.

The increase in flap suction with increasing thrust is visible, on both sides at AoA = 5 deg, specially in the Flap 30 deg configuration (Figs. (5.12a) and (5.12b)). Again, the higher increase in flap suction of the down-going blade side could be a consequence of the impingement from the adjacent propeller or the higher circulation present in the up-going blade side that would lower the suction on the flap due to the circulation effect. Higher dumping effect is also visible with increased flap pressure peak.

Small differences between the pressure distributions for different thrust settings are appreciated at AoA = 10 deg, especially the up-going blade side (Figs. (5.11c) and (5.11d) for the Flap 15 deg configuration and Figs. (5.12c) and (5.12d) for the Flap 30 deg configuration). This difference between up- and down-going blade side at AoA = 10 deg in both configurations could be originated because of propeller induced separation. As commented in the previous section, the combination of propeller inclination angle and AoA diminishes the effect of the slipstream on the lift enhancement making the wing lift enhancement mostly provided by the flap.

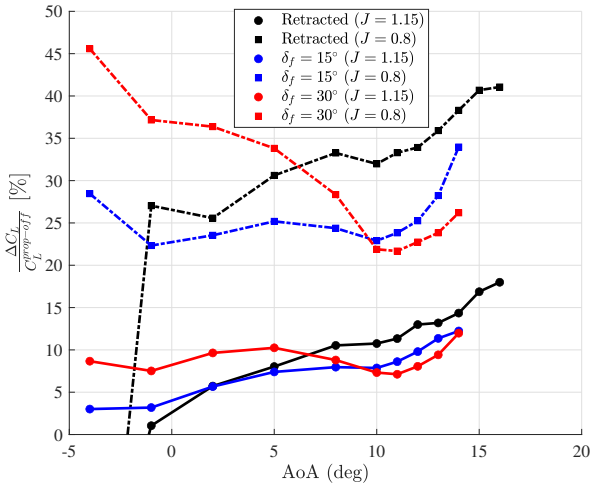

Figure 5.10: Effect of the flap deflection on the wing lift enhancement due to propeller slipstream for two thrust settings vs. AoA.

The differences are also small at high-angles of attack for the the up-going blade side (Figs. (5.11c) and (5.12c) for Flap 15 deg and 30 deg, respectively). Similar very high suction peak is obtained with increased thrust. On the down-going blade side (Figs. (5.11d) and (5.12d) for Flap 15 deg and 30 deg, respectively), the thrust has a higher impact on the flap suction enhancement due to the adjacent propeller impingement.

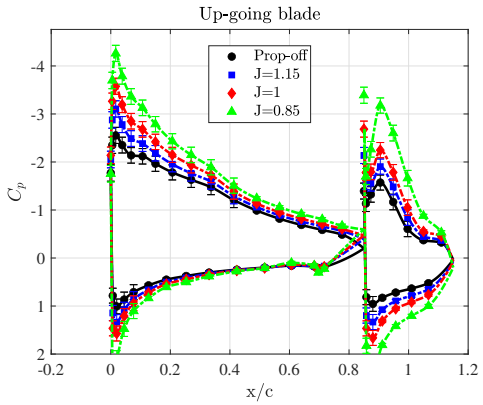

(a) AoA = 5 deg, Up-going blade side.

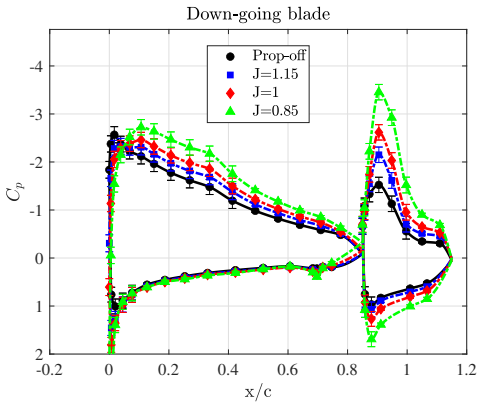

(b) AoA = 5 deg, Down-going blade side.

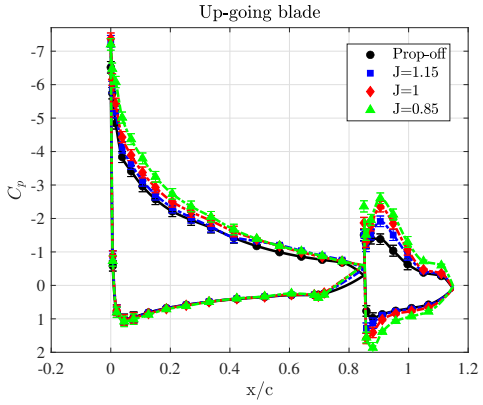

(c) AoA = 10 deg, Up-going blade side.

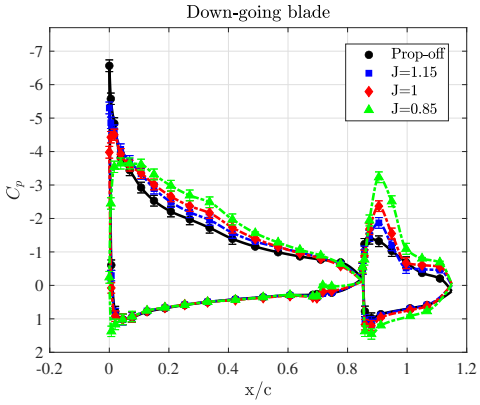

(d) AoA = 10 deg, Down-going blade side.

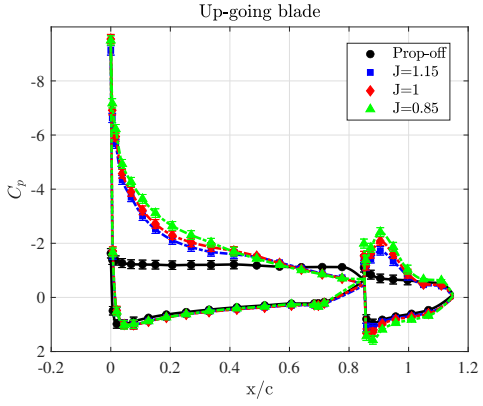

(e) AoA = 14 deg, Up-going blade side.

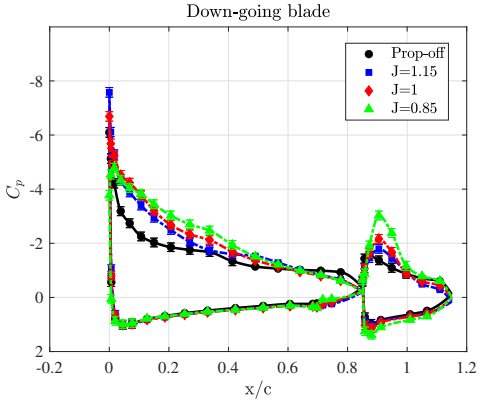

(f) AoA = 14 deg, Down-going blade side.

Figure 5.12: Pressure distribution at three AoA for different thrust settings. Flap 30 deg.

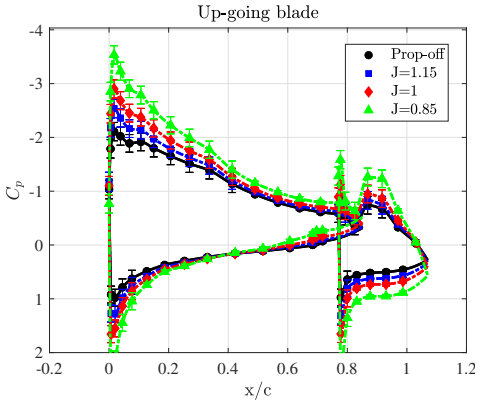

(a) AoA = 5 deg, Up-going blade side.

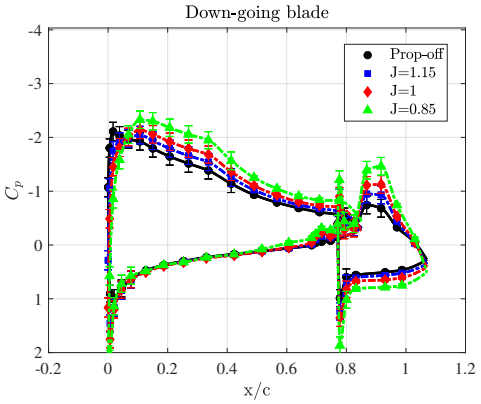

(b) AoA = 5 deg, Down-going blade side.

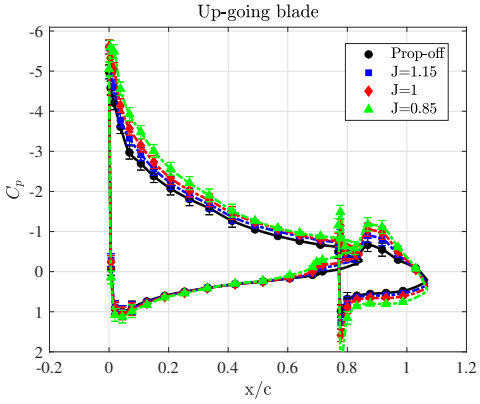

(c) AoA = 10 deg, Up-going blade side.

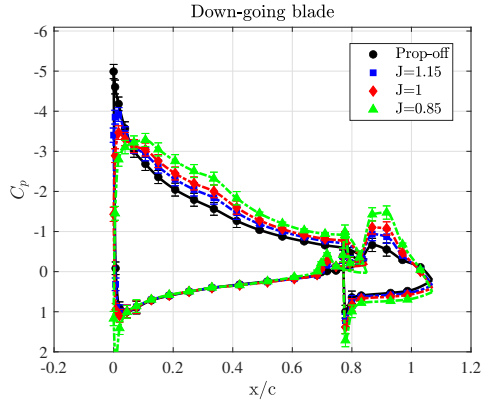

(d) AoA = 10 deg, Down-going blade side.

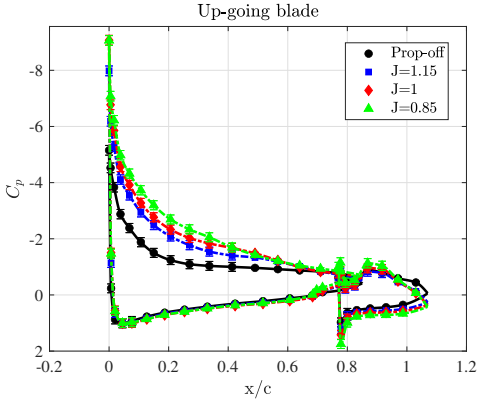

(e) AoA = 14 deg, Up-going blade side.

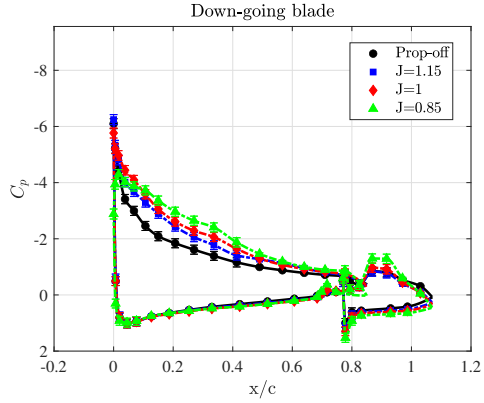

(f) AoA = 14 deg, Down-going blade side.

Figure 5.11: Pressure distribution at three AoA for different thrust settings. Flap 15 deg.

5.2.3. EFFECT OF FLAP DEFLECTION ON THE SLIPSTREAM DEFORMATION

In this section, the effect of flap deflection on the slipstream deformation is assessed. The results of the wake measured in prop-off and prop-on conditions (J = 1) are presented at AoA = 10 deg for the two flap deflections, 15 deg and 30 deg. It must be noticed that this AoA is the one where there is a significant drop in lift enhancement due to propeller induced separation.

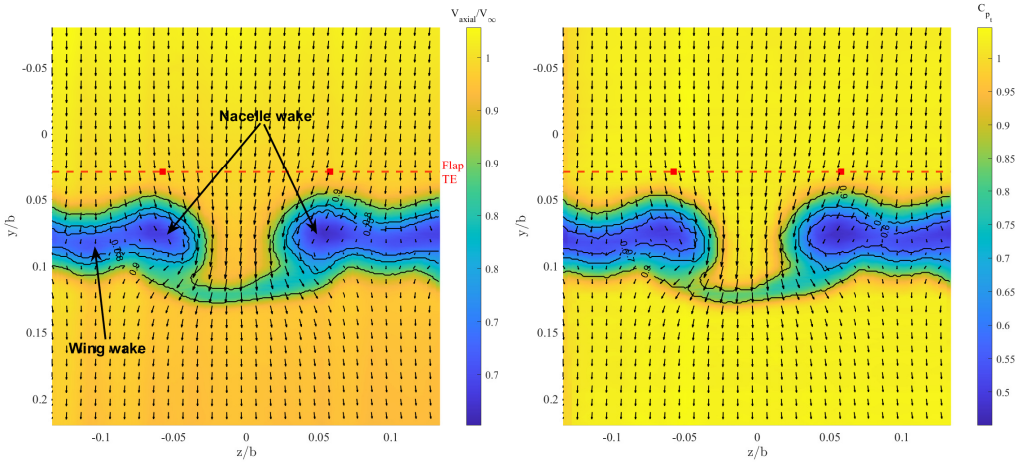

(a) Axial velocity ratio.

(b) Total pressure coefficient.

Figure 5.13: Wake measurement results of Flap 15 deg configuration in prop-off condition at AoA = 10 deg. View in upstream direction.

Figure (5.13) represents the wake results of the Flap 15 deg configuration in propeller-off conditions. The wake of the wing can be identified as the area of decreased total pressure and axial velocity. Nevertheless, contrary to the flap retracted configuration, the nacelle seems to split the flow in two vortices. Although any conclusions can be drawn from the data, the velocity distribution reveals how the flow curves around these areas (marked as nacelle vortex in Fig. (5.13a)). The two areas are joined by a strip of decreased axial velocity caused by the wake of the wing downstream of the nacelle. A similar velocity distribution is obtained for the Flap 30 deg configuration (Fig. (5.14)). While in the Flap 15 deg configuration the wake downstream of the nacelle is placed at a lower position that may be due to the induced downwards flow coming from the nacelle vortices, on the Flap 30 deg configuration there is trailing-edge separation in the flap that creates a wake. This flow separation makes the strip between vortices to be at the same location at the nacelle vortices.

Figures (5.15) and (**??**) shows the wake results for the Flap 15 deg and Flap 30 deg deflection, respectively, in a distributed propulsion configuration. The slipstream acquires a different shape when compared to the flap retracted case (figure (4.19)), which now has

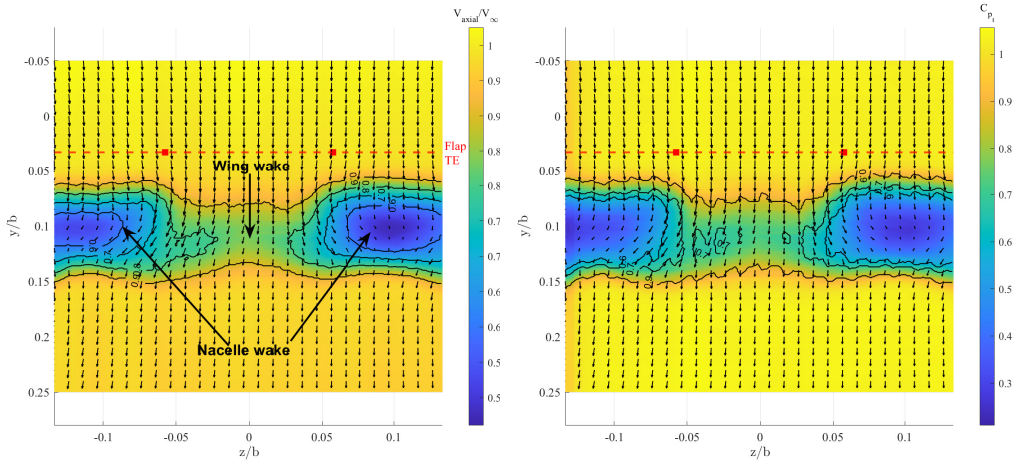

(a) Axial velocity ratio.

(b) Total pressure coefficient.

Figure 5.14: Wake measurement results of Flap 30 deg configuration in prop-off condition at AoA = 10 deg. View in upstream direction.

a shape similar to that of a hook. On both the 15 and 30 deg flap deflection configuration, on the top half, the circular shape of the slipstream can still be recognized and is preserved as an area of high axial velocity. The effect of the flap deflection angle is visible on the lower halve of the slipstream. When analyzing the velocity distribution, the swirl of the propeller is mitigated with increased flap deflection angle due to the increased downwash produced by the rise in circulation. The velocity distribution acquires a prominently downward direction. The boundary with the adjacent propellers is less discernible when the flap deflection angle is higher. On the bottom half, the axial velocity distribution gets planar and an area of accumulated high total pressure appears on the down-going blade side. In previous research [54], a total pressure distribution is presented for a flap deflection of 15 deg and, while the planar shape on the lower surface was appreciable, the area of increased total pressure was not. It is therefore concluded that the impingement coming from the adjacent propeller's slipstream generates this area of increased axial velocity present on the down-going blade side and is responsible of the increase in flap suction of that side compared to the up-going blade side. This area of increased axial velocity is placed below the flap trailing-edge location probably because it is deflected by the flap inclination. The deflection of flap makes the planar shape of the total pressure distribution to disappear on the bottom. The area of increased axial velocity produced by the adjacent slipstream impingement is also decreased with the flap deflection angle due to the separated flow on the flap trailing-edge, as it was shown in Fig. (5.9).

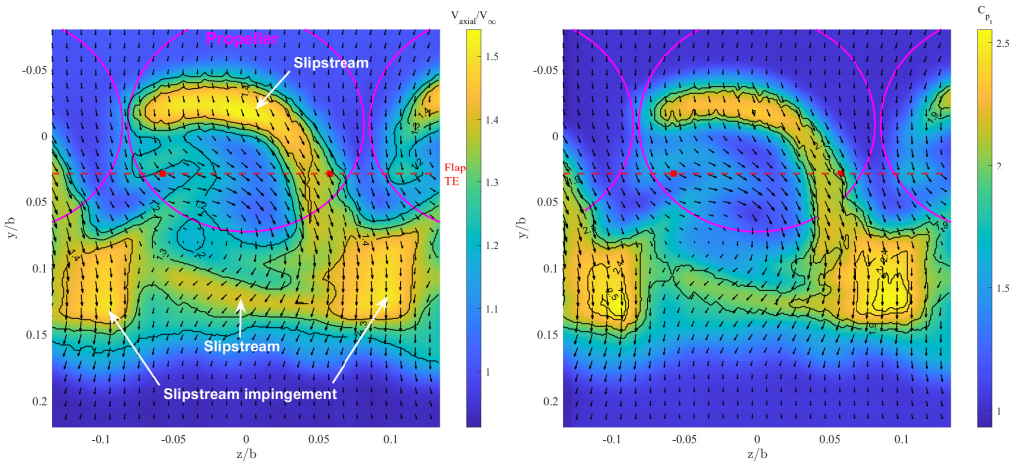

(a) Axial velocity ratio.

(b) Total pressure coefficient.

Figure 5.15: Wake measurement results of Flap 15 deg configuration in distributed-propulsion condition ($J = 1$) at AoA = 10 deg. View in upstream direction.

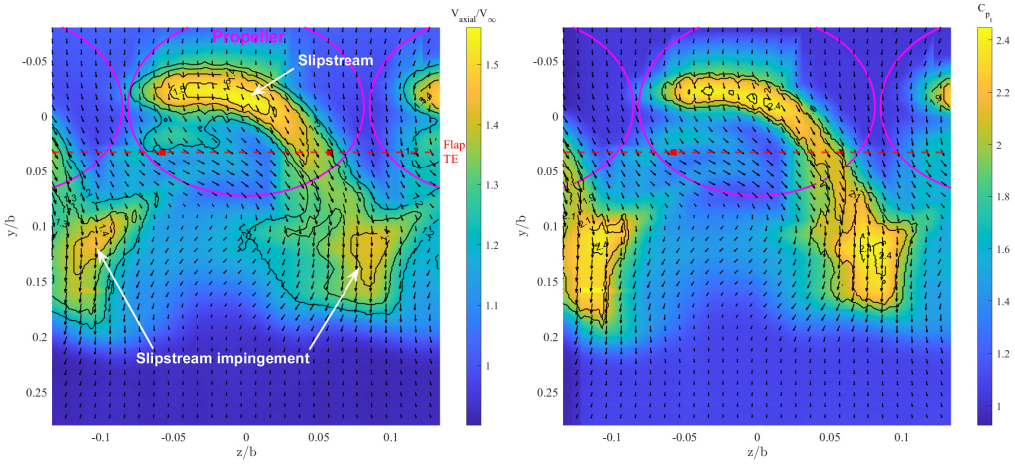

(a) Axial velocity ratio.

(b) Total pressure coefficient.

Figure 5.16: Wake measurement results of Flap 30 deg configuration in distributed-propulsion condition ($J = 1$) at AoA = 10 deg. View in upstream direction.

5.3. INFLUENCE OF FLAP SLOT ON THE LIFT ENHANCEMENT IN PROPELLER-ON CONDITION

In this section, the effect of the flap slot on the lift enhancement for the 30 deg flap deflection is assessed. In figure (5.17), the wing lift coefficient enhancement for the 30 deg flap deflection is presented. An increase in flap gap provides higher wing lift enhancement, except at AoA = 10 deg, where the propeller induced separation in the main element makes the lift enhancement drop for both flap slots. After that, the $y = 3\%c$ flap slot provides higher lift enhancement although it presents the erratic behaviour explained in section (5.1). To get more insight into the nature of this behavior, sectional aerodynamic data enhancement is provided (Fig. (5.18)). To support the behaviors observed in the aerodynamic coefficients, flap pressure distribution is shown (Fig. (5.19)).

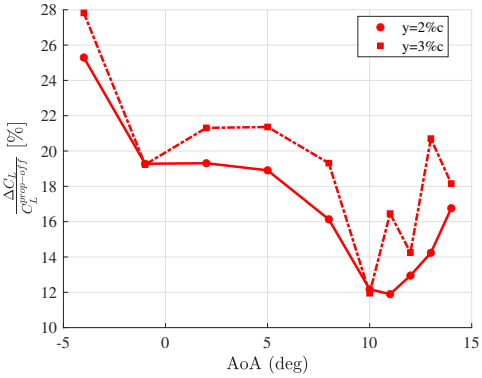

Figure 5.17: $\delta_f = 30$ deg

At low-AoA, on the down-going blade side there is a substantial increase in sectional lift enhancement with flap slot that goes with an increase in flap lift enhancement (5.18). Figure (5.19) reveals how the pressure distribution is similar for both flap slots at AoA = 5 deg, although a slight increase in suction is appreciated for the $y = 3\%c$ slot case close to the leading-edge as a consequence of the increased mass flow rate due to the larger gap. This trend is contrary to what is observed for the propeller-off case, where the flap stall hinders the pressure distribution to have higher suction. The difference in lift enhancement comes from this stalled flow of the propeller-off $y = 3\%c$ flap slot case that makes the enhancement higher, in spite of the similar pressure distribution.

The drop on the lift enhancement at AoA = 10 deg comes from the stalled flow provident from the main element that, despite merging with a fresh boundary layer from the flap, is not able to withstand the strong pressure gradient and creates stall towards the middle of the flap section. At high-AoA, again, the difference between attached flow in propeller-on conditions and stalled flap section provides a significant lift enhancement.

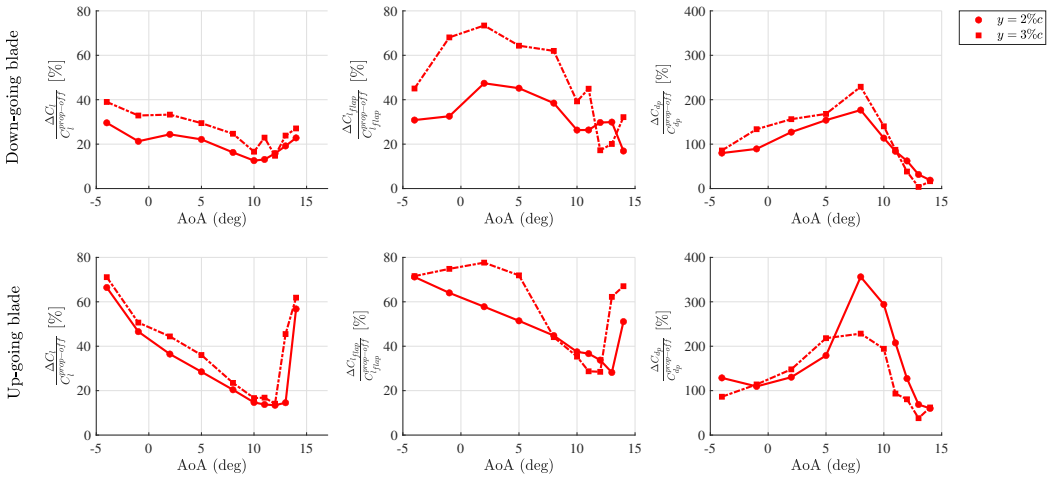

Figure 5.18: Sectional aerodynamic coefficients enhancement due to propeller slipstream ($J = 1$) vs. AoA for various flap slot values. Flap 30 deg.

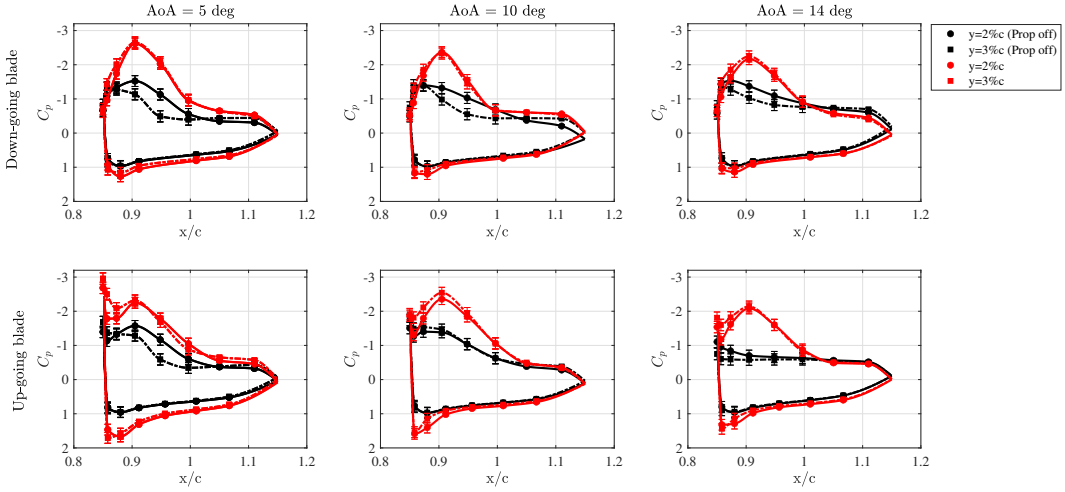

Figure 5.19: Flap pressure distribution, prop-off vs. prop-on. for two flap slot values. Flap 30 deg.

6

CONCLUSIONS

A wind tunnel experimental research is performed to gain insight into the aerodynamic interaction effects in propeller-wing-flap systems with leading-edge distributed propulsion, and to assess how this interaction changes with flap position. A 2.5D configuration has been used, consisting of a semi-span wing with distributed propulsion with the ability to have different flap deflections. Balance data and pressure distribution at two locations (up- and down-going blade side) are obtained and five-hole probe measurement is performed. The conclusions obtained from the results are presented in the form of answer to the research questions presented in Chapter (1).

What is the effect of using multiple propellers on the wing loading distribution, when compared to a single-propeller case?

When comparing the wing lift enhancement between the configuration with distributed-propulsion (3 propellers) and the lift enhancement produced by the single-propeller configuration but multiplied 3 times, similar values are obtained, so there is no benefit of the interaction between slipstreams on the wing lift. However, when analyzing the sectional data, there is an increase in sectional lift coefficient produced by the influence of the adjacent propeller. Therefore, the lift increase is greater on the down-going blade side since the adjacent propeller is up-going blade side, so its influence outside the propeller spanwise covered area is higher.

The pressure distribution is fully affected by the adjacent propeller. This results in an increase of the suction peak on the down-going blade side due to the influence of the adjacent up-going blade side; and the appearance of a bump, that could be a laminar bubble, at high angles of attack on the up-going blade side coming from the adjacent

down-going blade side.

When modifying the thrust generated by the propeller, an increase in the effective lift coefficient (including propeller forces) with respect to the propeller-off case of 30% is obtained for the high thrust condition ($J = 0.8$) and an increase of 8% for the low thrust condition ($J = 1.15$) at low angles of attack (AoA = 5 deg) while the increase is 41% and 18% for high and low thrust, respectively, at high angles of attack (AoA = 16 deg). When evaluating the contribution of the thrust force to the lift coefficient, it is found that has a small contribution (10%) at AoA = 16 deg for the highest thrust setting.

At low angles of attack, the increase in thrust causes the influence of the adjacent propeller to be magnified. In addition, due to the increased shear that deforms the slipstream when it interacts with the wing as the thrust increases, an increase in rear loading can be seen on the pressure side of the down-going blade side due to the impingement of the lower half of the adjacent slipstream. At high angles of attack, the increase in rear loading due to the increase in shear with thrust is probably not noticeable due to the higher position of the propeller.

What is the effect of the flap position on the change in aerodynamic coefficients due to slipstream effects?

When evaluating the effect of the flap position on the aerodynamic coefficients in distributed-propulsion systems, two parameters have been modified: the flap deflection angle and the flap slot (vertical distance between the flap and the main element trailing edge).

When comparing two flap deflection angles (15 and 30 deg) with the flap retracted configuration, it can be seen that a different lift enhancement behavior with AoA is obtained. While in flap retracted condition the increase in lift enhancement with AoA has a practically linear growth, the increase in flap deflection angle makes the evolution of lift enhancement with AoA become constant or even decreasing. Although there is a significant increase in lift enhancement at high angles of attack because the propeller-off configuration is stalled while the propeller-on case maintains the flow attached due to the increased Reynolds number.

At low angles of attack (between 5 and 8 degrees) the configuration with a flap deflection angle of 30 degrees provides the higher lift enhancement compared to the prop-off configuration, one reason is the increase in suction on the flap, specially on the down-going blade side. This is due to the impingement produced by the lower half of the adjacent slipstream being displaced due to shear, although it may also be a decrease in flap lift on the up-going blade side due to the increased circulation effect of having more lift on the main element.

As the angle of attack increases, the increase in suction on the flap decreases due to the decrease in impingement of the adjacent propeller by having the propeller disk in a higher

position. At medium-to-high AoA (between 8 and 12 degrees) there is a sudden decrease in lift enhancement because the slipstream effect on the main element disappears due to the combination of angle of attack and propeller inclination. This decrease is more pronounced the higher the flap deflection and on the up-going blade side.

Regarding the effect of the **flap gap** on the lift enhancement, a similar flap pressure distribution is obtained for both flap gap values except for a slight increase of suction in the flap leading-edge for the larger flap gap value, so the enhancement is higher for the latter case because it provides lower lift coefficient in propeller-off conditions.

How does the flap deflection affect the wake downstream of the system?

When the flap is retracted and the wing has an AoA of 2 degrees, the axial velocity distribution acquires the circular shape of both halves of the slipstream which have been displaced in opposite spanwise directions due to trailing vorticity. This displacement makes that the slipstream merges with the adjacent slipstream. However, deflecting the flap together with the increased angle of attack (AoA = 10 deg), modifies the shape of the axial velocity distribution, which acquires a shape that reminds to a hook, where only the circular shape can be seen in the upper half. The slipstream acquires a flat shape in the lower half and an area of increased axial velocity appears on the down-going blade side apparently without swirl which seems to be generated due to the impingement of the adjacent propeller's slipstream. This area of increased axial velocity is placed well below the wing location. This could be due to the flap inclination that deflects the flow and it is less apparent in the 30 deg flap configuration due to flow separation in the flap.

Apart from the general conclusions explained above, other conclusions that apply to this experimental model are presented.

- A wind tunnel run has been performed to evaluate potential **3D effects** on the model using small tufts on the upper surface. The result is that with the flap deflected 30 degrees and at high angles of attack, there is flow separation in a large portion of the span between the root and the first nacelle.
- In flap retracted conditions, the configuration was tested **covering the gap between flap and main element and without covering it**. There was no significant difference between the configurations other than a slight increase in lift at high angles of attack due to the small amount of air blown through the gap.
- Blockage and Streamline curvature **2D wind tunnel corrections** were calculated following a conservative approach to verify that they do not have a relevant impact on the aerodynamic coefficients and that, therefore, the data could be presented uncorrected.
- When evaluating the **effect that the presence of the nacelle had on the aerodynamic coefficients**, it could be seen that when the flap was retracted, the presence of the

nacelle provided additional lift at high angles of attack due to postponed separation and a slight increase in pressure drag probably due to an increase in the local angle of attack. However, with flap deflection, the effect was the opposite and lift was lower at high angles of attack due to a reduction of suction on the upper surface attributed to the cross-flow between high-pressure area (downwash of the nacelle) and low-pressure area.

Once the conclusions are presented, possible implications drawn from the findings, as well as limitations for future research, are suggested. All these comments are divided into different topics and shown below:

- **The influence of the diameter-to-chord ratio and the Reynolds number**

  The model used in this experiment has a diameter-to-wing-chord ratio of 0.66. Higher values of this parameter would result in a greater increase of the lift coefficient and would imply other changes such as a greater incidence of slipstream on the wing. It is suggested to test additional values of this parameter to assess its impact on the maximum lift enhancement and on the wing-flap aerodynamic interaction. In addition, the experiment takes place at a Reynolds number of approximately 610000, which is low and results in lower values of maximum lift when compared to STOL aircraft as well as different multi-element flow interaction. That is why the model used in this experiment is a limiting case for a real application of an aircraft with LEDP, so it is more applicable to Urban Air Mobility concepts. It is suggested to perform the same experiment at a higher Reynolds number to assess its effect on the flow separation and, again, on the wing-flap aerodynamic interaction.

- **Further research on single-propeller vs. distributed-propulsion**

  When analyzing the differences between single-propeller and distributed-propulsion configuration, we could see how the wing lift coefficient is similar if we compare the enhancement between distributed-propulsion and three times the enhancement of single-propeller. However, significant differences were observed when analyzing the local flow and wake. An analysis of the flow at more spanwise positions is suggested to understand how sectional lift enhancement is not reflected in the wing lift enhancement. In addition, to confirm this impingement due to slipstream deformation, that is enhanced with increased thrust, an analysis of the wake at different thrust settings and measurements also in the single-propeller case are necessary for comparison.

- **Test additional flap positions**:

  The initial idea was to test three flap gap values for two flap deflection angles and additionally one overlap value for each deflection angle. However, due to time constraints there was only time to test two flap gaps for each of the deflection angles. Furthermore, due to the low Reynolds number, in the flap deflection at 40 deg, the flow separation is predominant. That is why it is suggested to test the configurations

corresponding to the rest of the flap positions, including the configuration in which the flap was located in the position of maximum slipstream velocity for a higher Reynolds number so that the separation is not so present in the flap. In this way a more detailed map of the effect of flap position on lift enhancement could be obtained.

BIBLIOGRAPHY

[1] EASA, EEA, and EUROCONTROL, "European Aviation Environmental Report 2019," 2019. DOI: 10.2822/309946. [Online]. Available: https://ec.europa.eu/transport/sites/transport/files/2019-aviation-environmental-report.pdf.

[2] ICAO, "Environmental Report 2019," 2019.

[3] IATA, "Aircraft technology roadmap to 2050," 2013.

[4] European Union Commission, "Flightpath 2050 Europe's Vision for Aviation." DOI: 10.2777/50266.

[5] D. F. Finger, C. Braun, and C. Bil, "On Aircraft Design under the Consideration of Hybrid-Electric Propulsion On Aircraft Design under the Consideration of Hybrid-Electric Propulsion Systems," *Proceedings of the Asia-Pacific International Symposium on Aerospace Technology (APISAT2018)*, Chengdu, China, 2018.

[6] A. Y. Arabul, E. Kurt, F. Keskin Arabul, İ. Senol, M. Schrötter, R. Bréda, and D. Megyesi, "Perspectives and development of electrical systems in more electric aircraft," *International Journal of Aerospace Engineering*, vol. 2021, 2021.

[7] A. Misra, "Energy storage for electrified aircraft: The need for better batteries, fuel cells, and supercapacitors," *IEEE Electrification Magazine*, vol. 6, no. 3, pp. 54–61, 2018.

[8] T. P. Dever, K. P. Duffy, A. J. Provenza, P. L. Loyselle, B. B. Choi, C. R. Morrison, and A. M. Lowe, "Assessment of technologies for noncryogenic hybrid electric propulsion," 2015.

[9] C. E. Riboldi, L. Trainelli, and F. Biondani, "Structural batteries in aviation: A preliminary sizing methodology," *Journal of Aerospace Engineering*, vol. 33, no. 4, p. 04 020 031, 2020.

[10] M. Henke, G. Narjes, J. Hoffmann, *et al.*, "Challenges and Opportunities of Very Light High-Performance Electric Drives for Aviation," *Energies*, vol. 11, no. 2, p. 344, Feb. 2018, ISSN: 1996-1073. DOI: 10.3390/en11020344. [Online]. Available: http://www.mdpi.com/1996-1073/11/2/344.

[11] C. L. Bowman, J. L. Felder, and T. V. Marien, "Turbo-and hybrid-electrified aircraft propulsion concepts for commercial transport," *2018 AIAA/IEEE Electric Aircraft Technologies Symposium (EATS)*, IEEE, 2018, pp. 1–8.

[12] A. G. Rao, "Aero engine technology flight performance and propulsion," Faculty of Aerospace Engineering, T.U. Delft, 2016.

[13] T. Sinnige, N. van Arnhem, T. C. Stokkermans, G. Eitelberg, and L. Veldhuis, "Wingtip-mounted propellers: Aerodynamic analysis of interaction effects and comparison with conventional layout," *Journal of Aircraft*, vol. 56, no. 1, pp. 295–312, 2019.

[14] J. Patterson Jr. and G. Bartlett, "Effect of a wing-tip mounted pusher turboprop on the aerodynamic characteristics of a semi-span wing," *Proceedings of the 21st Joint Propulsion Conference*, Reston, Virigina: American Institute of Aeronautics and Astronautics, Jul. 1985. DOI: 10.2514/6.1985-1286. [Online]. Available: http://arc.aiaa.org/doi/10.2514/6.1985-1286.

[15] M. H. Snyder Jr. and G. W. Zumwalt, "Effects of wingtip-mounted propellers on wing lift and induced drag.," *Journal of Aircraft*, vol. 6, no. 5, pp. 392–397, Sep. 1969, ISSN: 0021-8669. DOI: 10.2514/3.44076. [Online]. Available: http://arc.aiaa.org/doi/10.2514/3.44076.

[16] J. R. Whurr and A. M. Rolt, "Optimizing propulsive efficiency in aircraft with boundary layer ingesting distributed propulsion," *ISABE 2015 (Awatef Hamed, Faculty Work and Research, College of Engineering and Applied Science)*, 2015.

[17] S. Sahoo, X. Zhao, and K. Kyprianidis, "A review of concepts, benefits, and challenges for future electrical propulsion-based aircraft," *Aerospace*, vol. 7, no. 4, p. 44, 2020.

[18] M. D. Patterson, J. M. Derlaga, and N. K. Borer, "High-lift propeller system configuration selection for nasa's sceptor distributed electric propulsion flight demonstrator," *16th AIAA Aviation Technology, Integration, and Operations Conference*, 2016, p. 3922.

[19] M. D. Patterson and N. K. Borer, "Approach considerations in aircraft with high-lift propeller systems," *17th AIAA Aviation Technology, Integration, and Operations Conference*, 2017, p. 3782.

[20] H. D. Kim, A. T. Perry, and P. J. Ansell, "A review of distributed electric propulsion concepts for air vehicle technology," *2018 AIAA/IEEE Electric Aircraft Technologies Symposium (EATS)*, IEEE, 2018, pp. 1–21.

[21] L. L. M. Veldhuis, "Propeller wing aerodynamic interference," PhD Dissertation, Delft University of Technology, 2005.

[22] G. L. Gentry Jr, M. Takallu, and Z. T. Applin, "Aerodynamic characteristics of a propeller-powered high-lift semispan wing," 1994.

[23] X. Fei, B. German, and M. D. Patterson, "Exploring the effects of installation geometry in high-lift propeller systems," *2018 AIAA Aerospace Sciences Meeting*, 2018, p. 0277.

[24] S. Mikhalyov, A. Dunaevsky, L. Teperin, R. Vasilyev, and A. Redkin, "Effects of propeller slipstream of distributed electric propulsion on the wing-flap system," *MATEC Web of Conferences*, EDP Sciences, vol. 304, 2019, p. 02 018.

[25] K. A. Deere, S. Viken, M. Carter, J. K. Viken, J. M. Derlaga, and A. M. Stoll, "Comparison of high-fidelity computational tools for wing design of a distributed electric propulsion aircraft," *35th AIAA Applied Aerodynamics Conference*, 2017, p. 3925.

[26] B. Bohari, Q. Borlon, P. B. Mendoza-Santos, A. Sgueglia, E. Benard, M. Bronz, and S. Defoort, "Conceptual design of distributed propellers aircraft: Non-linear aerodynamic model verification of propeller-wing interaction in high-lifting configuration," *2018 AIAA Aerospace Sciences Meeting*, 2018, p. 1742.

[27] X. Fei, "Evaluation of a commercial surface vorticity flow solver for the modeling of propeller-wing interaction," *AIAA Scitech 2019 Forum*, 2019, p. 1046.

[28] A. Aljabri and A. Hughes, "Wind tunnel investigation of the interaction of propeller slipstream with nacelle/wing/flap combinations," *AGARD Aerodyn. and Acoustics of Propellers*, 1985.

[29] A. M. Stoll, "Comparison of cfd and experimental results of the leaptech distributed electric propulsion blown wing," *15th AIAA aviation technology, integration, and operations conference*, 2015, p. 3188.

[30] B. Bohari, Q. Borlon, M. Bronz, and E. Benard, "Aerodynamic model of propeller–wing interaction for distributed propeller aircraft concept," *Proceedings of the Institution of Mechanical Engineers, Part G: Journal of Aerospace Engineering*, p. 0 954 410 019 857 300, 2019.

[31] B. W. McCormick, *Aerodynamics of V/STOL flight*. Courier Corporation, 1999.

[32] T. Theodorsen, *The Theory of Propellers: The Slipstream Contraction with Numerical Values for Two Blade and Four Blade Propellers*. US Government Printing Office, 1947.

[33] M. K. Rwigema, "Propeller blade element momentum theory with vortex wake deflection," *27th International congress of the aeronautical sciences*, vol. 2010, 2010, pp. 2–3.

[34] J. K. Viken, S. Viken, K. A. Deere, and M. Carter, "Design of the cruise and flap airfoil for the X-57 Maxwell distributed electric propulsion aircraft," 2017.

[35] B. Stratford, "The prediction of separation of the turbulent boundary layer," *Journal of fluid mechanics*, vol. 5, no. 1, pp. 1–16, 1959.

[36] R. H. Liebeck, "Design of subsonic airfoils for high lift," *Journal of aircraft*, vol. 15, no. 9, pp. 547–561, 1978.

[37] A. M. Smith, "High-lift aerodynamics," *Journal of Aircraft*, vol. 12, no. 6, pp. 501–530, 1975.

[38] L. L. M. Veldhuis, "Review of propeller-wing aerodynamic interference," *24th International Congress of the Aeronautical Sciences*, vol. 6, 2004.

[39] S. J. Miley, R. M. Howard, and B. J. Holmes, "Wing laminar boundary layer in the presence of a propeller slipstream," *Journal of Aircraft*, vol. 25, no. 7, pp. 606–611, 1988.

[40] R. E. Kuhn, "Semiempirical procedure for estimating lift and drag characteristics of propeller-wing-flap configurations for vertical-and short-take-off-and-landing airplanes," 1959.

[41] Z. Ning, "Experimental investigations on the aerodynamic and aeroacoustic characteristics of small uas propellers," 2018.

[42] J. F. Cahill, "Summary of section data on trailing-edge high-lift devices," 1949.

[43] TU Delft, "Propeller models," Flight Performance - Propeller Aerodynamics - Facilities, (accessed: 01.09.2021).

[44] Jane's All the World's Aircraft: Development & Production, "ATR42," Aircraft - Fixed-Wing - Civil, 2020.

[45] L. Boermans and P. Rutten, "Two-dimensional aerodynamic characteristics of airfoil NLF-MOD22 with flap," Delft University of Technology, 1995.

[46] C. J. Wenzinger and T. A. Harris, "Wind-tunnel investigation of an N.A.C.A. 23012 airfoil with various arrangements of slotted flaps," National Advisory Committee for Aeronautics, 1939.

[47] T. A. Harris and P. E. Purser, "Wind-tunnel investigation of an NACA 23012 airfoil with two sizes of balanced split flap," Langley Memorial Aeronautical Laboratory, Langley Field, VA, 1940.

[48] D. Foster, H. Irwin, Williams, and B. Williams, "The two-dimensional flow around a slotted flap," Aerodynamics Dept. RAE Farnborough, 1971.

[49] DNW Aero, *Low-speed tunnel*. [Online]. Available: https://www.dnw.aero/wind-tunnels/lst/, (accessed: 20.09.2021).

[50] L. Veldhuis, "Aircraft aerodynamics," Faculty of Aerospace Engineering, T.U. Delft, 2019.

[51] N. van Arnhem, R. de Vries, T. Sinnige, R. Vos, G. Eitelberg, and L. Veldhuis, "Engineering method to estimate the blade loading of propellers in nonuniform flow," *AIAA Journal*, vol. 58, no. 12, pp. 5332–5346, 2020.

[52] S. Yoo and J. Duensing, "Computational analysis of the external aerodynamics of the unpowered x-57 mod-iii aircraft," *AIAA Aviation 2019 Forum*, 2019, p. 3698.

[53] Y. Qiu, J. Bai, and L. Qiao, "Aerodynamic effects of wing-mounted engine nacelle on high-lift configuration of turboprop airliner," *Journal of Aircraft*, vol. 55, no. 3, pp. 1082–1089, 2018.

[54] Y. Leng, M. Bronz, T. Jardin, and J.-M. Moschetta, "Slipstream deformation of a propeller-wing combination applied for convertible uavs in hover condition," *Unmanned Systems*, vol. 8, no. 4, pp. 295–308, 2020.

[55] *Hyperworks 13.0: Optistruct reference guide*, Altair Hyperworks, 2014.

[56] M. Avalos, I. Alvarez-Armas, and A. Armas, "Dynamic strain aging effects on low-cycle fatigue of aisi 430f," *Materials Science and Engineering: A*, vol. 513, pp. 1–7, 2009.

[57] R. de Vries, N. van Arnhem, T. Sinnige, R. Vos, and L. Veldhuis, "Aerodynamic interaction between propellers of a distributed-propulsion system in forward flight," *Aerospace Science and Technology*, vol. 118, 2021.

[58] J. B. Barlow, W. H. Rae, and A. Pope, *Low-speed wind tunnel testing*. John wiley & sons, 1999.

A

MODEL DETAILED DESIGN

In this appendix, the detailed design considerations for each of the components of the propeller-wing-flap system are addressed. To provide a better explanation of these details, the components are divided into groups. The model consists of a beam attach to the ceiling of the wind tunnel and the wing is divided into segments. There are different types of segments depending on if they have the propeller attached, if they have pressure taps or if they are simply clean wing. Similarly to the wing, there are flap segments that are attached to the wing through brackets. A drawing representing an overview of the model exploded is shown in figure (A.1). In this drawing, each of the components is represented using a numerical code so they can be identified.

The beam consists of two pieces made of steel: the main beam and the beam balance block. The first piece consists of a cylinder where the wing is placed. This piece goes into the beam balance block, that is the part that is attached to the balance. The main beam possesses a screwed hole in the end opposite to the wing attached to the balance. The relative movement between main beam and beam balance block is constrained using a key.

The wing is divided into nine segments that are made of aluminium. The wing segments consists of a main element, the part that corresponds to the flap is separated. All the segments have a circular hole because they are strung by the beam. In order to avoid a rotation between the segments, they have two pin holes. Apart from the beam hole, they have two more holes for the pressure tubes and the engine wires. In the cove, there is a slot for the brackets that attaches the flap segments to the wing segments, the bracket is fixed to the wing segment using a bolt.

Two segments have pressure taps (1.4 and 1.5), to record pressure data during the experiment. Three of the segments possess a hole in the leading-edge to attach the nacelle (1.3). When the nacelle is removed, a leading-edge cap is placed instead that has the same shape of the leading edge to make a clean wing configuration. The rest of the segments are the wing root segment (1.6), the wing main segment (1.2) and the tip wing segment (1.1), that has a hole concentric to the beam hole where a nut is screwed to the beam that tightens the wing segments to the beam balance block.

Similar to the wing segments, the flap segments (from 1.15 to 1.20) are skewed by the flap beam (1.21). Two pin holes are placed to avoid rotation between segments and an additional hole is made for the flap pressure taps tubes. The attachment between wing and flap is made using a bracket (1.22). Since different flap positions are tested, there is a different bracket per flap position (and one extra for the flap retracted configuration) and six bracket per bracket type. The bracket is attached to both wing and flap using bolts to ease the change between flap configurations.

The nacelles consists of two halves, one attached to the upper surface and the other attached to the lower surface, using bolts. A fairing is placed between the top half of the nacelle and the upper surface of the wing and another fairing is placed between the bottom half of the nacelle and the lower surface of the wing with the aim of smoothing the flow transition from nacelle to wing and therefore try to avoid flow separation.

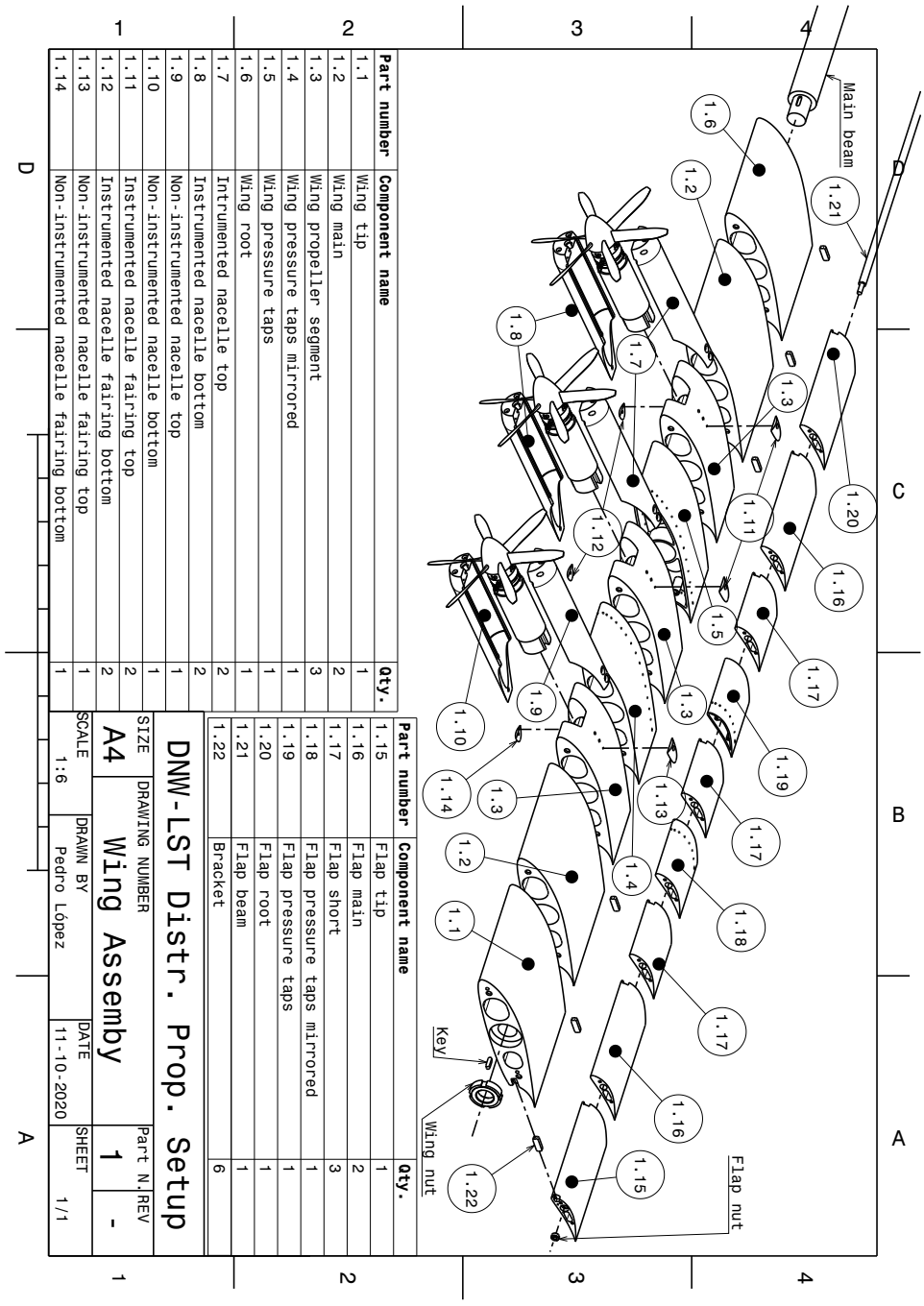

Part number	Component name	Qty.
1.1	Wing tip	1
1.2	Wing main	2
1.3	Wing propeller segment	3
1.4	Wing pressure taps mirrored	1
1.5	Wing pressure taps	1
1.6	Wing root	1
1.7	Intrumented nacelle top	2
1.8	Instrumented nacelle bottom	2
1.9	Non-instrumented nacelle top	1
1.10	Non-instrumented nacelle bottom	1
1.11	Instrumented nacelle fairing top	2
1.12	Instrumented nacelle fairing bottom	2
1.13	Non-instrumented nacelle fairing top	1
1.14	Non-instrumented nacelle fairing bottom	1

Part number	Component name	Qty.
1.15	Flap tip	1
1.16	Flap main	2
1.17	Flap short	3
1.18	Flap pressure taps mirrored	1
1.19	Flap pressure taps	1
1.20	Flap root	1
1.21	Flap beam	1
1.22	Bracket	6

DNW-LST Distr. Prop. Setup

SIZE	DRAWING NUMBER		Part N.	REV
A4	Wing Assemby		1	-
SCALE	DRAWN BY	DATE	SHEET	
1:6	Pedro López	11-10-2020	1/1	

Figure A.1: Drawing representing the overview of all the components of the model exploded.

B

STRUCTURAL ANALYSIS

In order to ensure the safety of the wind tunnel and its personnel, structural requirements must be fulfilled in agreement to the DNW policy. In this section, a FEM analysis is performed using the most restricted loads expected during the experiment on the most critical parts to ensure that the safety factor is met. The analysis is performed using Altair Optistruct 2019 for the calculations and Altair Hyperworks 2019 for the pre/post-processing of the results. The first subsection encompasses the computational setup, where the most critical parts are identified and an explanation of how these parts are modelled is provided. In the second subsection, the critical loads are estimated for the static, dynamics and modal analysis. Finally, the results of the analysis are provided together with the safety margins.

B.1. COMPUTATIONAL SETUP

Performing an analysis of the whole model may be very complex and will not allow to identify the most critical part of each component. Three different analyses are therefore proposed for which the model is divided in three parts. First, the wing segments mounted on the beam may be critical because of the slenderness of the beam and the contact between wing segments. Since the wing operates under high-lift conditions, an appreciable displacement of the tip may be detrimental for the correct interpretation of the experimental results. Second, the wing-bracket assembly may be a potential source of failure due to the bending moment where the bracket is attached to the wing, generated by the flap normal force on the wing. Finally, the propeller is envisioned as a potential critical part due to its rotational nature and the loads expected during its operation. For the three analysis, the selection of the mesh, the modelling of the contacts and the constraints are explained.

B

MESH

All the components on the wing and the beam are modelled separately. The flap segments, the bracket and the nacelles are not included in the analysis for simplicity. In the case of the wing-bracket assembly the flap is not included because the critical stresses are expected in the wing-bracket union due to the moment arm created by the flap normal force. In the case of the propeller, the model consists of the propeller hub and the blades, the shaft is not included. A picture of three meshed models can be found in figure (B.1). The elements used for creating the mesh in all cases are CTETRA elements (four-sided solid element with four grid points) [55] due to its easiness to adapt to complex shapes such as the wing profile or the blade twist. The mesh density is increased in those elements that have more detail, like the pressure taps segments because they have one half hollow. The property selected for all the elements is PSOLID since they are solid elements [55].

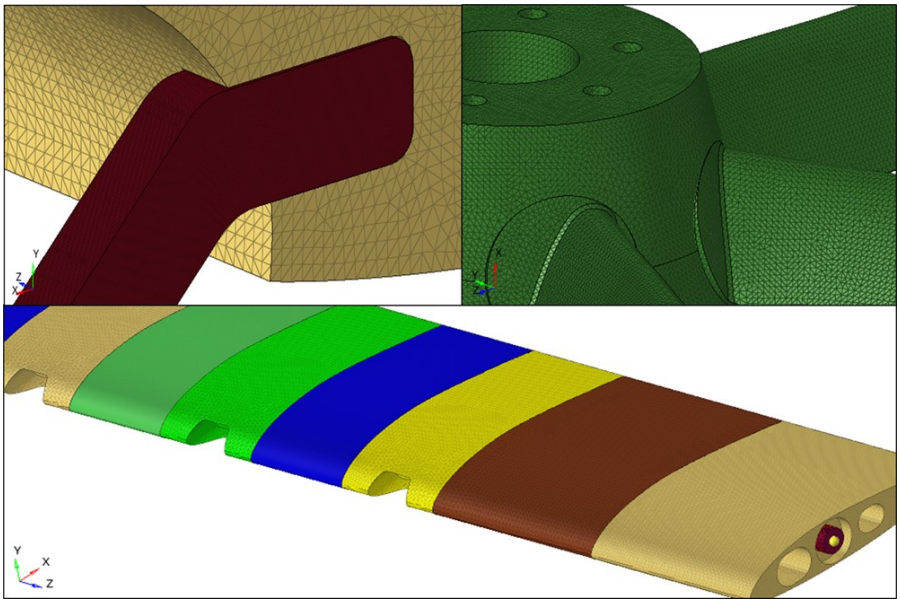

Figure B.1: Representation of the meshed models for the three analysis. Top left, bracket-wing assembly; top right, propeller; bottom, wing assembly.

MATERIALS

Only two materials are present in the model: aluminium and stainless steel. All the components are made of aluminium except for the components of the beam, the brackets and the propeller, that are made of stainless steel. The material properties can be found in table (B.1)

Since the propeller may be subject to fatigue damage, the fatigue properties of the

	Stainless steel 430F	Aluminium Alplan ® 6082
Density (kg/m^3)	7700	2700
Young's modulus (GPa)	200	69
Poisson's ratio	0.27	0.33
Yield strength (MPa)	310	240
Ultimate strength tensile (MPa)	552	276

Table B.1: Material properties from references

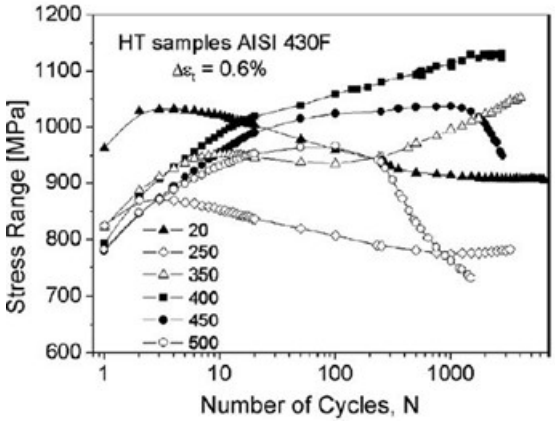

Figure B.2: SN curve of the stainless steel 430F [56].

stainless steel 430F are shown in figure (B.2). This SN curve of the material for different temperatures is obtained from Ref. [56]. If room temperature is assumed for the experiment, a infinite cycle life is obtained for stress ranges below 900 MPa (± 450 MPa).

B.1.1. CONTACTS, CONNECTORS AND CONSTRAINTS

When there is a contact between the different components, properties are assigned to the interface between them. In the wing-beam and wing-bracket assembly, a CONTACT with static friction coefficient is selected [55]. For aluminium-aluminium contact, like the contact between wing segments, a coefficient of 0.75 is established. When the contact is a steel-aluminium contact, like the beam-wing contact or the bracket-wing contact a coefficient of 0.4 is selected. In the case of the propeller model, the contact between the different components (propeller hub and blades) is defined as a TIE contact [55], which means that the the nodes that are in contact from both components have the same motion. After evaluating different types of contact it is concluded that the TIE contact is the more realistic and conservative.

The bracket is attached to the wing using a bolt, in order to model this attachment, the bolt is modelled as a CBEAM element [55]. The properties assigned to the element are the ones corresponding to PBEAM [55], so the bolt is assumed to be a circular beam with the same dimensions as the real bolt.

Constraints are defined for the three models. First, in the wing assembly, the six degrees-of-freedom are set to zero in the beam block that attaches the model to the wind-tunnel wall. Second, in the bracket-wing assembly, the dofs of the side of the wing segment opposite to the bracket are set to zero. Finally, in the propeller analysis, the degrees-of-freedom of the inner nodes that would be in contact with the shaft are set to zero.

B.2. LOADS

In this subsection, the different loads that are applied in the three analysis are defined. For each of the analysis, the loads are calculated together with their point of application.

WING ASSEMBLY

The main load in the wing assembly is the lift force. The drag and the thrust are not considered in this analysis because they are assumed to be one order of magnitude lower. The lift is considered to be more critical due to its higher magnitude and because it is applied in the direction of lower moment of inertia. Since the gravity applied in the direction of the beam because the model is attached to the ceiling, it does not contribute to the torsional or bending moment. A conservative approach is made for calculating the magnitude of the lift force because a constant lift distribution is defined in spanwise direction.

The maximum lift that may be expected is calculated using the maximum lift coefficient obtained for the same airfoil when the flap is deflected 40 deg [45]. The value of the $C_{L_{max}}$ is 3.3. In order to add the lift enhancement due to the effect of the slipstream, a thrust coefficient of 1 is assumed, which is approximately the maximum one that can be tested [57]. In the following conditions, V_∞=40 m/s and ρ=1.225 kg/m^3 and the velocity induced by the propeller is 20% higher than the freestream velocity. If we assume that the lift enhancement is proportional to the increase in dynamic pressure and we take into account that only half of the wing area is wetted by the propeller slipstream, we obtain the following lift coefficient:

$$C'_{L_{max}} = C_{L_{max}} \cdot 1.2^2 \cdot 0.5 + C_{L_{max}} \cdot 0.5 = 4$$

The lift force that results from this maximum lift coefficient is applied as a constant

pressure in the lower surface of the wing.

A compression force is applied at the tip wing segment against the other segments as a result of the installation nut. The magnitude has a value of 1000 N and it is selected arbitrarily. Nevertheless, a ten-fold increase in this magnitude resulted in just a 10% increase in maximum stress which is still in the safety margin. A counteracting force is applied to the beam in the opposite direction.

A potential source of dynamic loading in the wing is the unsteady flow separation at high angles of attack. Other potential sources of dynamic loading, such as the unsteady loads generated by the propeller have been demonstrated to be negligible in previous research [57]. The required safety factor is 30% higher than the static one. Since all the analysis is on the elastic range, this increase in safety factor is compared as a 30% increase in the magnitude of the loads.

WING-BRACKET ASSEMBLY

The lift generated by the flap is assumed to be proportional to its chord, therefore 30% of the maximum lift force obtained using $C_{L_{max}} = 4$ is generated by the flap, although this approach is conservative because the lift generated by the flap is less than the 30% in all cases [45]. Since only one bracket is analyzed, the force is divided into six and applied as a point load normal to the bracket surface which coincides with the flap normal direction.

PROPELLER

Two types of loads are applied in the propeller. First, a rotational force is applied to all the elements of the model. This force is applied as a RFORCE [55]. In order to define this force, a rotational velocity of 184.5 Hz is selected as the maximum velocity tested in the experiment. Second, a pressure distribution is applied on one of the blades to simulate the maximum expected thrust during the experiment. The load distribution is obtained using the method described in Ref. [51], although this load distribution is obtained under extreme inflow conditions (AoA = 15 deg) which is unlikely to be reached during the experiment. The load distribution selected is the one at the blade position of maximum integral blade thrust. Figure (B.3) shows the load distribution in maximum and minimum thrust coefficient conditions. The torque on the blade is neglected.

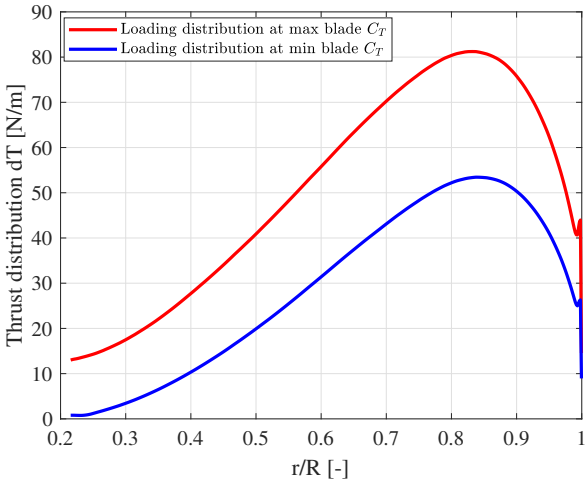

Figure B.3: Loading distribution of the propeller for maximum and minimum thrust coefficient conditions throughout a revolution at AoA = 15 deg and ω = 184.5 Hz.

B.3. RESULTS

In this subsection, the results from the static analysis in terms of Von Mises stress and shear stress are presented. When representing the stress map in the different components, the results are presented as the simple average of the stresses of the nodes of each element because the mesh is fine enough to avoid big differences between adjacent nodes. All the results are collected in table (B.2) and the Safety Factors (SF) are calculated and compared with the DNW requirements. First, in the wing-beam assembly, the most relevant stresses are found in the beam block, on the traction side. Both Von Misess stress map and shear stress map are shown in figure (B.4).

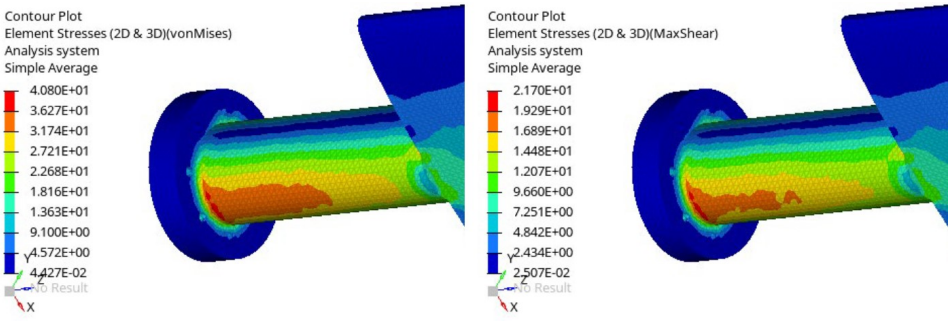

Figure B.4: Results of the static analysis for the wing-beam assembly. On the left side, Von Mises stress (MPa). On the right side, Shear stress (MPa).

Second, in the bracket-wing assembly, the most relevant stresses are found in the corner

radius close to the wing. Among all the brackets, the most critcal results are found for the bracket that corresponds to the flap position that correspond to maximum slipstream velocity (40 deg, x=0%, y=17.85%). This result was expected due to the large moment arm of the lift force generated by the flap. The stress map for this bracket is shown in figure (B.5), where only the stress map of the bracket is shown.

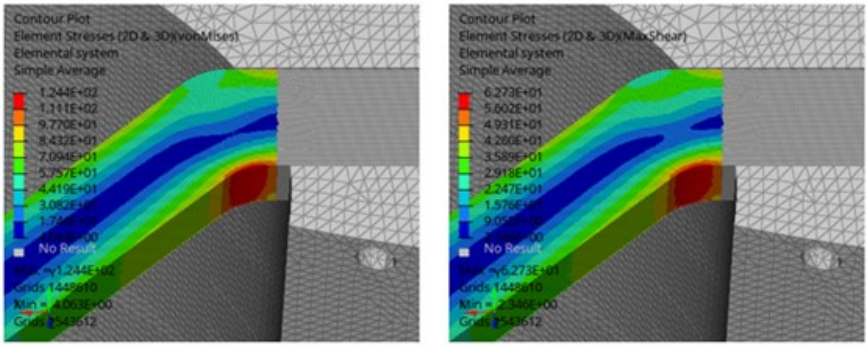

Figure B.5: Results of the static analysis on the bracket for the bracket-wing assembly. On the left side, Von Mises stress (MPa). On the right side, Shear stress (MPa).

Finally, in the propeller, the most critical stresses are found at the root of the blade, in the area where the blade has less area. Since the centrifugal force acts as a normal force to the blade sectional area, the stresses are higher there due to the reduced area. These results are shown in figure (B.6).

In table (B.2), the results of the three analysis are collected. According to the DNW requirements, the Safety factor required is 2.5 and 3 depending on if the Ultimate Tensile Strength or the Yield Strength is used, respectively. The required Safety Factor is increased in 30% in order to evaluate dynamic loading as explained in the Loads subsection (B.2). To sum up, all the Safety factors are above the requires by DNW, the model meets the requirements for being testes at the DNW Wind Tunnel.

Model	**Maximum von Mises stress**	**Maximum shear stress**	**UTS**	**YS**	**SF (UTS)**	**SF (YS)**
Wing-beam assembly	40.8 MPa	21.7 MPa	552 MPa	310 MPa	13.5	6.7
Bracket-wing assembly	124.4 MPa	62.7 MPa	552 MPa	310 MPa	4.4	4.9
Propeller	55.1 MPa	28.5 MPa	552 MPa	310 MPa	10	10.9

Table B.2: Stresses and safety factor (SF) of the three models under static loading.

Regarding the fatigue analysis, since the maximum stresses obtained in the propeller are well below the range of 900 MPa stated in the Materials section, it is considered that the propeller will not suffer from fatigue damage during the wind-tunnel campaign.

B

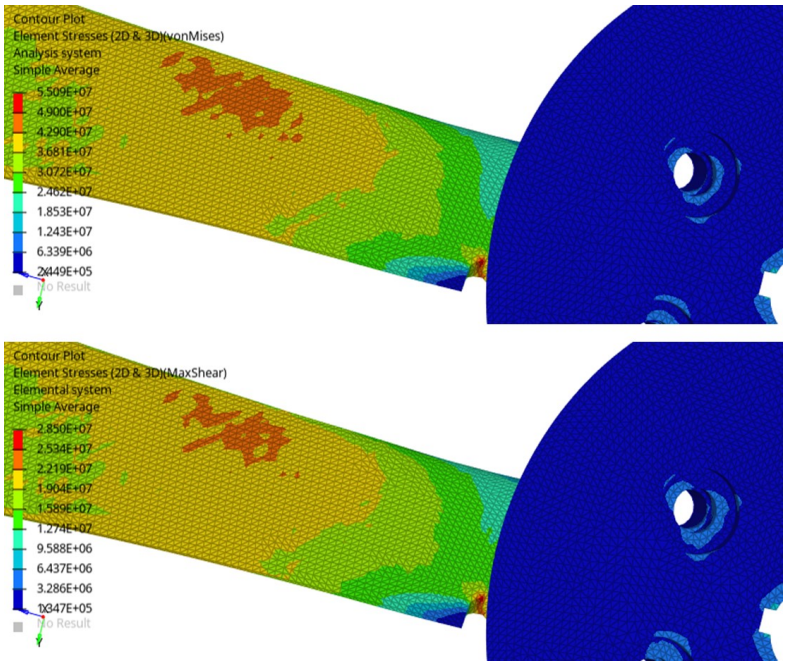

Figure B.6: Results of the static analysis for the propeller. On the top, Von Mises stress (MPa). On the bottom, Shear stress (MPa).

C

PRESSURE TAPS LOCATION

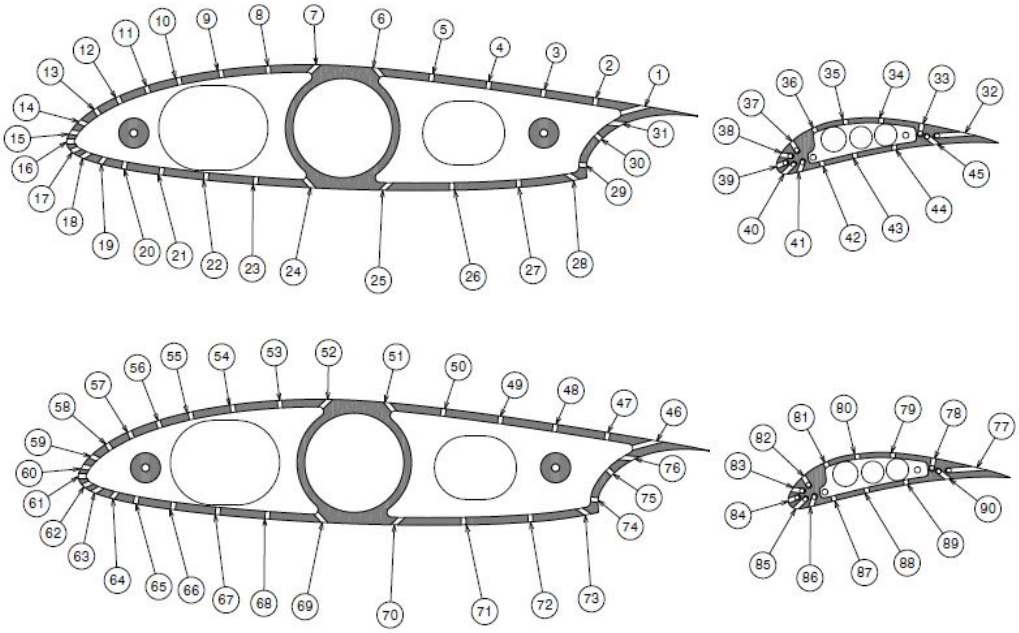

Figure C.1: Pressure taps numbering. On top, right side (down-going blade). On bottom, left side (up-going blade).

C

CODE	X [m]	Y [m]	Z [m]	Chord [mm]	X/C [-]	Surface	Seq
MR1	0.23300	0.01477	-0.07110	255.0	0.91	main, top	001
MR2	0.21300	0.01815	-0.07110	255.0	0.84	main, top	002
MR3	0.19200	0.02149	-0.07110	255.0	0.75	main, top	003
MR4	0.17000	0.02473	-0.07110	255.0	0.67	main, top	004
MR5	0.14700	0.02776	-0.07110	255.0	0.58	main, top	005
MR6	0.12400	0.03021	-0.07110	255.0	0.49	main, top	006
MR7	0.10100	0.03149	-0.07110	255.0	0.40	main, top	007
MR8	0.08100	0.03104	-0.07110	255.0	0.32	main, top	008
MR9	0.06200	0.02930	-0.07110	255.0	0.24	main, top	009
MR10	0.04500	0.02636	-0.07110	255.0	0.18	main, top	010
MR11	0.03200	0.02292	-0.07110	255.0	0.13	main, top	011
MR12	0.02050	0.01859	-0.07110	255.0	0.08	main, top	012
MR13	0.01150	0.01374	-0.07110	255.0	0.05	main, top	013
MR14	0.00500	0.00872	-0.07110	255.0	0.02	main, top	014
MR15	0.00150	0.00444	-0.07110	255.0	0.01	main, top	015
MR16	0.00000	0.00000	-0.07110	255.0	0.00	main, LE	016
MR17	0.00200	-0.00338	-0.07110	255.0	0.01	main, bottom	017
MR18	0.00600	-0.00588	-0.07110	255.0	0.02	main, bottom	018
MR19	0.01350	-0.00837	-0.07110	255.0	0.05	main, bottom	019
MR20	0.02300	-0.01047	-0.07110	255.0	0.09	main, bottom	020
MR21	0.03800	-0.01281	-0.07110	255.0	0.15	main, bottom	021
MR22	0.05600	-0.01490	-0.07110	255.0	0.22	main, bottom	022
MR23	0.07600	-0.01660	-0.07110	255.0	0.30	main, bottom	023
MR24	0.09900	-0.01802	-0.07110	255.0	0.39	main, bottom	024
MR25	0.12700	-0.01895	-0.07110	255.0	0.50	main, bottom	025
MR26	0.15500	-0.01897	-0.07110	255.0	0.61	main, bottom	026
MR27	0.18200	-0.01781	-0.07110	255.0	0.71	main, bottom	027
MR28	0.20500	-0.01483	-0.07110	255.0	0.80	main, bottom	028
MR29	0.20910	-0.00900	-0.07110	255.0	0.82	main, bottom	029
MR30	0.21500	0.00132	-0.07110	255.0	0.84	main, bottom	030
MR31	0.22400	0.00760	-0.07110	255.0	0.88	main, bottom	031
FR32	0.07900	0.00376	-0.07110	90.00	0.88	flap, top	032
FR33	0.06000	0.00781	-0.07110	90.00	0.67	flap, top	033
FR34	0.04400	0.01001	-0.07110	90.00	0.49	flap, top	034
FR35	0.02950	0.00949	-0.07110	90.00	0.33	flap, top	035
FR36	0.01650	0.00615	-0.07110	90.00	0.18	flap, top	036
FR37	0.00700	0.00050	-0.07110	90.00	0.08	flap, top	037
FR38	0.00200	-0.00481	-0.07110	90.00	0.02	flap, top	038
FR39	0.00000	-0.00934	-0.07110	90.00	0.00	flap, LE	039
FR40	0.00250	-0.01248	-0.07110	90.00	0.03	flap, bottom	040
FR41	0.00900	-0.01159	-0.07110	90.00	0.10	flap, bottom	041
FR42	0.01850	-0.00926	-0.07110	90.00	0.21	flap, bottom	042
FR43	0.03200	-0.00605	-0.07110	90.00	0.36	flap, bottom	043
FR44	0.04800	-0.00281	-0.07110	90.00	0.53	flap, bottom	044
FR45	0.06500	-0.00057	-0.07110	90.00	0.72	flap, bottom	045

Table C.1: Position of the pressure taps in right side (down-going blade).

CODE	X [m]	Y [m]	Z [m]	Chord [mm]	X/C [-]	Surface	Seq
ML46	0.23300	0.01477	0.07110	255.0	0.91	main, top	046
ML47	0.21300	0.01815	0.07110	255.0	0.84	main, top	047
ML48	0.19200	0.02149	0.07110	255.0	0.75	main, top	048
ML49	0.17000	0.02473	0.07110	255.0	0.67	main, top	049
ML50	0.14700	0.02776	0.07110	255.0	0.58	main, top	050
ML51	0.12400	0.03021	0.07110	255.0	0.49	main, top	051
ML52	0.10100	0.03149	0.07110	255.0	0.40	main, top	052
ML53	0.08100	0.03104	0.07110	255.0	0.32	main, top	053
ML54	0.06200	0.02930	0.07110	255.0	0.24	main, top	054
ML55	0.04500	0.02636	0.07110	255.0	0.18	main, top	055
ML56	0.03200	0.02292	0.07110	255.0	0.13	main, top	056
ML57	0.02050	0.01859	0.07110	255.0	0.08	main, top	057
ML58	0.01150	0.01374	0.07110	255.0	0.05	main, top	058
ML59	0.00500	0.00872	0.07110	255.0	0.02	main, top	059
ML60	0.00150	0.00444	0.07110	255.0	0.01	main, top	060
ML61	0.00000	0.00000	0.07110	255.0	0.00	main, LE	061
ML62	0.00200	-0.00338	0.07110	255.0	0.01	main, bottom	062
ML63	0.00600	-0.00588	0.07110	255.0	0.02	main, bottom	063
ML64	0.01350	-0.00837	0.07110	255.0	0.05	main, bottom	064
ML65	0.02300	-0.01047	0.07110	255.0	0.09	main, bottom	065
ML66	0.03800	-0.01281	0.07110	255.0	0.15	main, bottom	066
ML67	0.05600	-0.01490	0.07110	255.0	0.22	main, bottom	067
ML68	0.07600	-0.01660	0.07110	255.0	0.30	main, bottom	068
ML69	0.09900	-0.01802	0.07110	255.0	0.39	main, bottom	069
ML70	0.12700	-0.01895	0.07110	255.0	0.50	main, bottom	070
ML71	0.15500	-0.01897	0.07110	255.0	0.61	main, bottom	071
ML72	0.18200	-0.01781	0.07110	255.0	0.71	main, bottom	072
ML73	0.20500	-0.01483	0.07110	255.0	0.80	main, bottom	073
ML74	0.20910	-0.00900	0.07110	255.0	0.82	main, bottom	074
ML75	0.21500	0.00132	0.07110	255.0	0.84	main, bottom	075
ML76	0.22400	0.00760	0.07110	255.0	0.88	main, bottom	076
FL77	0.07900	0.00376	0.07110	90.00	0.88	flap, top	077
FL78	0.06000	0.00781	0.07110	90.00	0.67	flap, top	078
FL79	0.04400	0.01001	0.07110	90.00	0.49	flap, top	079
FL80	0.02950	0.00949	0.07110	90.00	0.33	flap, top	080
FL81	0.01650	0.00615	0.07110	90.00	0.18	flap, top	081
FL82	0.00700	0.00050	0.07110	90.00	0.08	flap, top	082
FL83	0.00200	-0.00481	0.07110	90.00	0.02	flap, top	083
FL84	0.00000	-0.00934	0.07110	90.00	0.00	flap, LE	084
FL85	0.00250	-0.01248	0.07110	90.00	0.03	flap, bottom	085
FL86	0.00900	-0.01159	0.07110	90.00	0.10	flap, bottom	086
FL87	0.01850	-0.00926	0.07110	90.00	0.21	flap, bottom	087
FL88	0.03200	-0.00605	0.07110	90.00	0.36	flap, bottom	088
FL89	0.04800	-0.00281	0.07110	90.00	0.53	flap, bottom	089
FL90	0.06500	-0.00057	0.07110	90.00	0.72	flap, bottom	090

Table C.2: Position of the pressure taps in right side (down-going blade).

D

WIND TUNNEL CORRECTIONS

This appendix presents the methodology used to calculate the wind tunnel corrections. The following methodology is extracted from Ref. [58]. Two types of corrections are performed for 2D models in closed-section: blockage and streamline curvature. The model is assumed to be spanning the whole wind-tunnel section (2.25 m x 3 m), what leads to a section area of 6.75 m^2.

D.1. BLOCKAGE CORRECTIONS

Three sources of blockage are identified in this model: solid blockage, wake blockage and slipstream blockage.

SOLID BLOCKAGE (ϵ_s)

Due to the presence of the walls, the flow between the model and the wall experiments a contraction which leads to an increase in velocity that is assumed to be constant over the model. It is calculated using the following expression:

$$\epsilon_s = \frac{K \cdot \text{Volume}}{C^{3/2}} = 8.533E-4 \tag{D.1}$$

Where K is a factor that depends on the orientation of the model, in this case 0.54 for

being positioned spanning the tunnel height [58]. The volume of the model is estimated using the following expression [58]:

$$\text{Volume} = 0.7 \cdot t/c \cdot c \cdot c \cdot b = 0.0277\text{m}^3 \tag{D.2}$$

WAKE BLOCKAGE (ϵ_w)

In the wake generated by the model the air slows down, consequently, the air outside the wake must speed up, following the continuity equation similarly as the solid blockage. For 2D models, the following equation is used:

$$\epsilon_w = \frac{c/h}{2} C_{d_u} \tag{D.3}$$

Where c/h is the chord divided by the wind tunnel width (3 m). C_{d_u} is the uncorrected drag coefficient, two values corresponding to low (AoA = 5 deg) and high (AoA = 13 deg) angle of attack of the 30 deg flap deflection configuration (Fig. (5.4b)) are used to assess its impact on the wind-tunnel corrections:

AoA	C_{d_u}	ϵ_w
5 deg	0.12	0.0069
13 deg	0.28	0.0161

SLIPSTREAM BLOCKAGE (ϵ_{ss})

The slipstream generated by the propellers increase the velocity of the flow. Outside the influence of the slipstream, the flow slows down following the continuity equation. Figure (D.1) shows this change in velocity. To account for this effect, the following equation is used:

$$\epsilon_{ss} = -\frac{\tau A_p/C}{2\sqrt{1+2\tau}} = -0.01295236 \tag{D.4}$$

Where A_p is the propeller disk area (in this case, of three propellers). The term τ is the thrust normalized with the air density, the propeller area and the velocity squared. The maximum achievable value is estimated to be 2.4 for an advance ratio of 0.8.

Adding the three blockage contributions, the following total blockage is obtained:

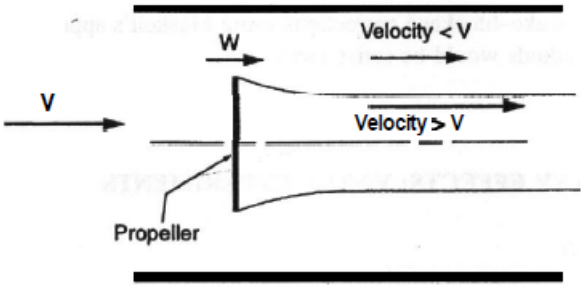

Figure D.1: Representation of the slipstream blockage [58].

$$\epsilon_{\text{AoA=5deg}} = 5.5755E-4$$

$$\epsilon_{\text{AoA=13deg}} = 9.7576E-4$$

D.2. STREAMLINE CURVATURE

The presence of the wall alters the normal curvature of the air around the airfoil, increasing the lift coefficient. This corrections is used taking into account the following parameter [58]:

$$\sigma = \frac{\pi^2}{48}\left(\frac{c}{h}\right)^2 = 0.0027 \tag{D.5}$$

The influence of the blockage and the streamline curvature on the lift and drag coefficient is computed in the following way [58]:

$$\frac{c_l}{c_{l_u}} = 1 - \sigma - 2\epsilon \tag{D.6}$$

$$\frac{c_{d_0}}{c_{d_{0u}}} = 1 - 3\epsilon_s - 2\epsilon_w + 2\epsilon_{ss} \tag{D.7}$$

The last term of the slipstream blockage is not present on the equation extracted from Ref.[58], but it is included as the opposite effect of the model wake. The following ratios between corrected and uncorrected lift and zero-lift drag coefficient are obtained:

AoA	$\frac{c_l}{c_{l_u}}$	$\frac{c_{d_0}}{c_{d_{0u}}}$
5 deg	0.996	0.969
13 deg	0.981	0.954

From this analysis, a difference between corrected and uncorrected lift coefficient of 0.4% and 1.9% are obtained for AoA of 5 and 13 deg, respectively. It is concluded that the wind tunnel effects may be negligible throughout the entire AoA range, except at high-AoA where these effect may have a slight impact in the lift coefficient achieved.

When analyzing the difference between corrected and uncorrected zero-lift drag coefficient, values of 3.1% and 4.6% are obtained for AoA of 5 and 13 deg, respectively. It must be noticed that the zero-lift drag coefficient is part of the drag coefficient. To summarize, since the differences between corrected and uncorrected zero-lift drag coefficient would not have a big impact on the results and the research is focused on lift enhancement, it is concluded that the wind-tunnel corrections are not applied to the raw data.